

Mapping Tactile Imaging Information: Parameter Estimation and Deformable Registration

A thesis presented by
Anna M Galea

to

The Division of Engineering and Applied Sciences
in partial fulfillment of the requirements for the degree of
Doctor of Philosophy in the subject of Engineering Sciences

Harvard University
Cambridge, Massachusetts
January 2004



© 2004 Anna M Galea
All rights reserved.

This thesis printed on 100% post-consumer recycled paper.

Mapping Tactile Imaging Information:

Parameter Estimation and Deformable Registration

Advisor
Robert D. Howe

Author
Anna M Galea

Abstract

Medical Tactile Imaging uses an array of pressure sensors mounted on a rigid scanhead to record the surface pressures that result when the scanhead is pressed into biological tissue. The resulting tactile data quantifies palpation, and contains information on the stiffness of the underlying tissue as well as the geometric distribution of the stiffness. Tactile imaging shows promise for clinical use in breast palpation and in assessing tissue properties in organs such as the liver. To date, tactile information has been used to estimate tissue geometry but not stiffness. We develop a linear algorithm to estimate the salient tissue parameters from a simple model of a solid lesion attached to the substrate of soft tissue. The parameters of interest are the background stiffness and thickness, and the stiffness and diameter of a round lesion. The algorithm is developed using finite element models, and results obtained on physical models show errors of 5.4% in estimating lesion modulus. This work was extended to the case of a solid lesion floating in soft tissue,

which encompasses cases of pathology in a large breast or pathology in the liver or prostate. Parameter estimation from finite element data showed errors of 12% for the modulus of large lesions. Extending this model to hollow areas in soft tissue, such as the large veins in livers, resulted in errors of 25 and 13% for estimating the size and depth of veins in perfused porcine livers. Given the success of applying a linear algorithm to the relationship between tissue parameters and tactile information, we study the impulse response of the system to explore the limits of tactile imaging using the currently available scanheads. Employing tactile imaging clinically in breast cancer screening requires registration of tactile images to other modalities such as mammograms. A deformable registration algorithm is developed on finite element models and applied to a physical model with less than 2.4 mm registration error. A preliminary clinical study shows good registration between the tactile and mammographic images, and holds promise for increasing the positive predictive value of breast cancer screening.

Mapping Tactile Imaging Information:

Parameter Estimation and Deformable Registration

Anna M Galea

Contents

Abstract	iii
Dedication	viii
Acknowledgements	ix
Epigraph	x
1. Introduction	1
1.1. Tactile Imaging	1
1.2. Motivation	5
1.3. Thesis Scope and Outline	6
1.4. Background	8
1.4.1. Tactile Imagers	8
1.4.2. Breast Anatomy and Pathology	10
Anatomy	10
Mechanical Properties	12
Roots of Pathology	13
Breast Cancer Statistics	14
1.4.3. Imaging Modalities for Breast Cancer Screening	16
Breast Self Exam	17
Clinical Breast Exam	17
Mammography	18
Tactile Imaging and Breast Cancer Screening	20
1.4.4. Other Organs	21
Anatomy and Pathology of the Liver	21
2. Fixed Lesion Parameter Estimation	25
2.1. Introduction	25
2.1.1. Problem Statement	26
2.1.1.1. Simplifying Assumptions	29
2.1.2. Previous Work	32
2.1.3. Analytical Solution	34
2.1.4. Tactile Scanning	40
2.1.5. Parameter Ranges	42

2.2. Mechanical Modeling	43
2.2.1. Finite Element Model Construction	43
2.2.2. Tactile Information from Finite Element Models	45
2.3. Inversion Algorithm	48
2.3.1. Algorithm Development	48
2.3.2. Calculating the Transformation Matrix	55
2.4. The Transformation Matrix	56
2.4.1. Rank Deficiency	56
2.4.2. Visualizing the Transformation Matrix	59
2.4.3. Numerical Transformation Matrix	59
2.4.4. Reconstituted Transformation Matrix	61
2.4.5. Physical Basis of the Transformation Matrix	63
2.4.6. Synthetic Transformation Matrix	67
2.5. Parameter Estimation Results	71
2.5.1. Results from the Numerical Transformation Matrix	71
2.5.2. Results from the Reconstituted Transformation Matrix	78
2.5.3. Results from the Synthetic Transformation Matrix	80
2.6. Towards Physical Data	82
2.6.1. Noise Analysis	82
2.6.2. Tactile System Calibration	83
2.7. Experimental Validation	84
2.7.1. Physical Model Construction	84
2.7.2. Data Collection	86
2.7.3. Experimental Parameter Estimation Results	87
2.8. Discussion and Future Work	89
2.8.1. Summary	89
2.8.2. Discussion of Estimation Results	91
2.8.3. Towards Clinical Data	94
2.8.4. Future Work	97
3. Round Lesion in Soft Tissue	99
3.1. Introduction	99
3.2. Mechanical Modeling	101
3.2.1. Linearized Parameters	103
3.3. Solid Lesion Results	105
3.4. Vessel Parameter Estimation	110
3.5. Experimental Results	113
3.6. Discussion and Future Work	116
4. Continuous Estimation	121
4.1. Introduction	121
4.2. Estimation Approach	122
4.2.1. Pressure Output	124
4.3. Mechanical Modeling	125

4.4. Linearity	127
4.5. Algorithm Development	131
4.5.1. Estimating the Glandular Tissue Thickness	136
4.6. Effect of the Background Modulus	138
4.7. System Resolution	140
4.8. Results and Discussion	142
4.9. Future Work	144
5. Mammography Registered Tactile Imaging	146
5.1. Introduction	146
5.1.1. Motivation	147
5.1.2. Chapter Layout	148
5.1.3. Further Clinical Application	151
5.1.4. Previous Work	152
5.2. Mechanical Modeling	153
5.2.1. Model-based Approach	153
5.2.2. Finite Element Model Development	154
5.2.3. Finite Element Model Data	158
5.2.4. Algorithm Development	160
5.2.5. Finite Element Model Registration	166
5.3. Physical Modeling	168
5.3.1. Physical Model Construction	168
5.3.2. Obtaining Model Mammogram and Tactile Image	171
5.3.3. Experimental Results	172
5.3.4. Discussion	173
5.4. Preliminary Clinical Testing	174
5.4.1. Clinical Data Acquisition	174
5.4.2. Calibration	177
5.4.3. Clinical Registration	188
5.4.4. Clinical Data Results	192
5.5. Discussion	197
5.6. Future Work	200
6. Summary and Future Work	202
References	208
Appendix A - Parameters for Finite Element Models	213
Appendix B - Protocol for Future Work	220

to

Brock

Acknowledgements

The work presented here would not have been possible without the contributions of the following people:

My advisor, Robert Howe, who believed in the idea of this research and found a way to keep it going through lean times.

Other professors in the Division, especially Joost Vlassak, Garrett Stanley, and John Hutchinson, who have taken time to answer my questions and guide my thinking.

Fellow students in the BioRobotics Lab. From brainstorming ideas to keeping my computer connected to the world, and giving me a reason to smile when I came to work, their contribution extends in ways I may not even be aware of.

My family and friends, who have been unfailingly supportive at every turn. Turns out your close friends are the ones who will listen to you go on and on about a topic they don't understand, just because you seem to need to talk about it.

My husband, Fred, who has stood by me, listening and supporting, from the day I decided to stay poor for four more years and pursue a PhD. I didn't understand how works could be dedicated to other people until I married him.

This work is intended to advance the field of tactile imaging, particularly in breast cancer screening. This work is not finished. It will not be finished until there is no more need for it. Let us never forget the terrible toll on lives young and old that cancer exacts.

“..breast cancer detection is one of the most important and most challenging engineering problems. It’s exciting to be working on something that has so much potential for saving women’s lives ... This area of research provides the most natural source of inspiration”

Susan Hagness
‘Not your mother’s Mammography’
IEEE Spectrum, October 2002

Chapter 1

Introduction

Tactile Imaging uses an array of passive pressure sensors to map the surface pressures that result from indenting the tactile imager into the surface of a soft material. The field of medical tactile imaging evolved out of a recognition that pathologies in the human breast can manifest as stiffness in the otherwise relatively soft organ [Frei 78, Cundari 96, West 99]. The breast in particular has been a driving force behind tactile imaging advancement, since it is an easily accessible organ with pathologies that can be palpated or imaged using tactile imaging.

1.1. Tactile Imaging

The human sense of touch is an established method for detecting pathologies that manifest as a stiff area under the surface of a soft organ. Clinical palpation, however, has been shown to result in qualitative information highly dependent on the practitioner [Evans 99, Jatoi 97, Pennypacker 99]. A method to noninvasively and reliably measure the mechanical properties of soft tissue and map embedded structures has been the

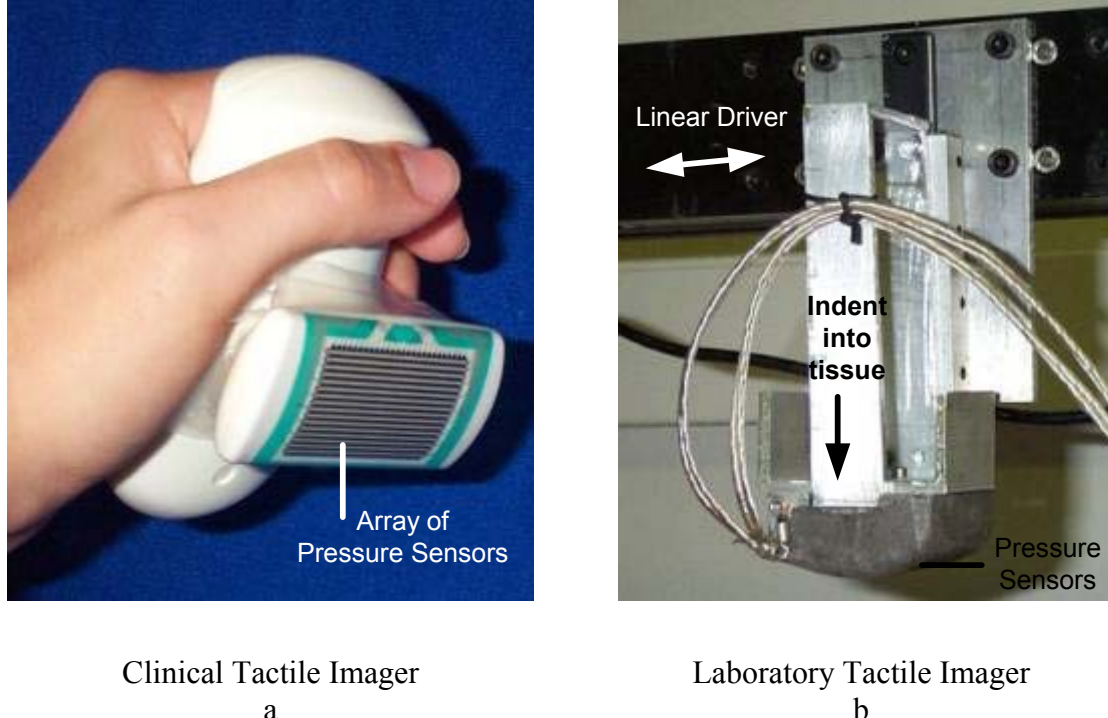
driving goal for several researchers [Hendrickson 03, Kita 01, Maier 98, Sanada 00, Sarvazyan 97, West 99]. Tactile imaging is the most direct way of mechanically implementing the palpation performed clinically.

In the last 25 years several advances in the field of tactile imaging have been made, particularly in devising better sensors in different shapes and sizes for various organs besides the breast. Tactile imaging has been shown to provide a method to quantify palpation [Wellman 99b], however the field is still in its infancy and is not yet in widespread clinical use.

Examples of tactile imagers are shown in figure 1.1. The exact size and shape of the tactile imager varies with the specific application it was intended for, however due to manufacturing limitations the pressure arrays on tactile imagers used in modern studies are mounted on a cylindrical surface with a radius of curvature in at most only one direction.

The most common use of the tactile information contained in the individual frames of pressure data collected is the generation of a two-dimensional Tactile Map [figure 1.2]. In tactile mapping, the frames are projected onto a flat representative plane using their spatial position information. Overlapping pressure information is averaged to create the Tactile Map [figure 1.3]. The resulting Tactile Map contains information about both the underlying material modulus and the geometry of the stiffness distribution. Aliasing can occur wherein two distinct geometry and stiffness profiles generate the same tactile map. Wellman [Wellman 99a] showed that even for the simple case of a hard round lump in a

soft tissue, cases arise where a small hard lump generates the same tactile map as a larger softer lump to within 0.5% mean square difference.



Clinical Tactile Imager
a

Laboratory Tactile Imager
b

Figure 1.1. Tactile Imager Scanheads. (a) Tactile Imager built for clinical use and used in the data collection of Chapter 5. Pressure is recorded by an array of 16x26 resistive pressure sensors, and the position of each pressure frame is recorded magnetically. (b) Tactile Imager used in the model data collection of Chapters 2 and 3. This imager has a 16x16 array of capacitive pressure sensors. The position of the pressure frames can be recorded in one dimension by a linear driver as shown here. Alternately, the scanhead can be removed and the position recorded in three dimensions (6 coordinates) by a magnetic tracker.

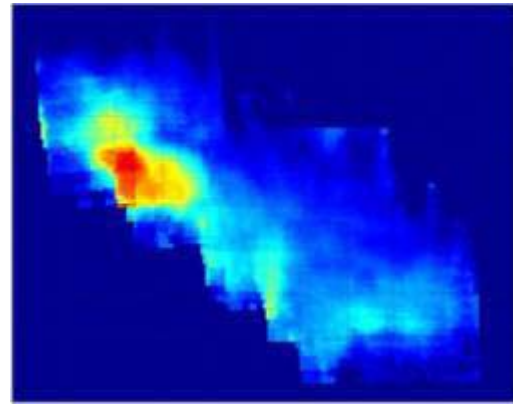


Figure 1.2. Sample Tactile Map. This map was obtained in short vertical swipes using the tactile imager in figure 1.1b. Note the hard lesion in red and yellow in the top left of the image.

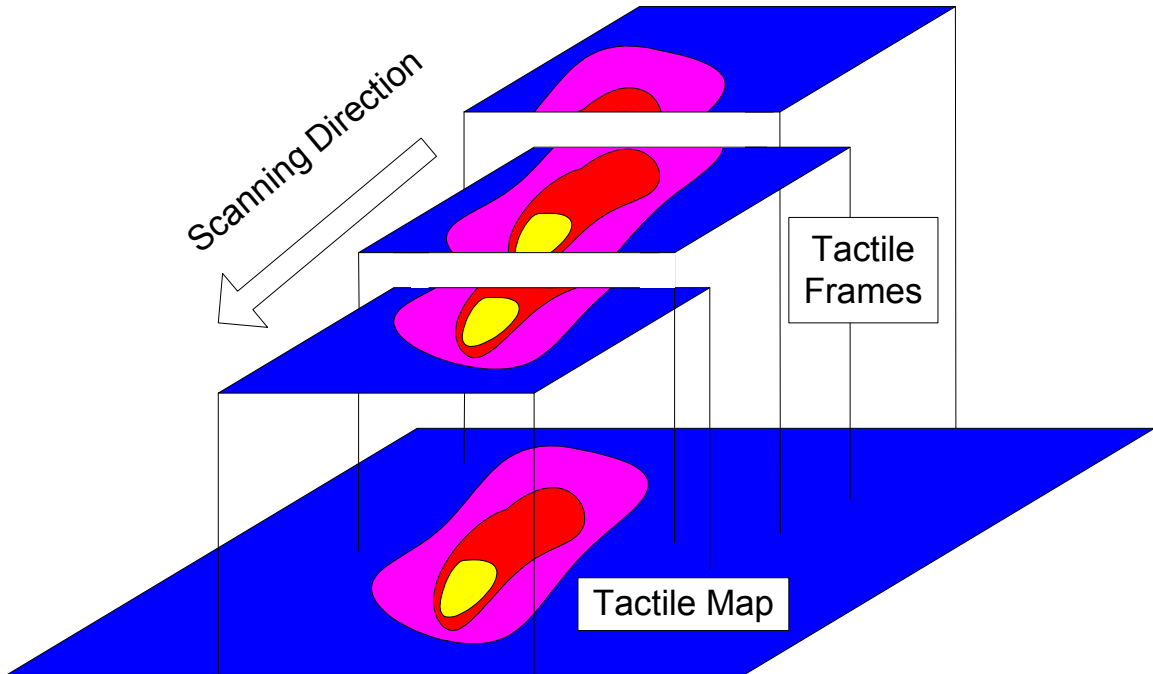


Figure 1.3. Generating a Tactile Map from Tactile Frames. Each frame is localized in space, projected onto a 2-D plane that best fits the spatial data, and the overlapping data is averaged to create the map.

Despite aliasing issues, tactile imaging is a valuable tool for quantifying palpation [Wellman 99b]. Tactile imaging can indicate the presence of stiff areas in soft tissues and yield quantitative information about these areas of increased stiffness [Wang 99]. Tactile imaging has been shown to be more sensitive to changes in lesion size than clinical palpation [Wellman 01]. Also, the tactile map has been shown to be repeatable for a range of users, and thus corrects a main fault cited for clinical palpation. The use of tactile imaging has been explored in various medical fields, including breast, liver, and prostate studies [Sarvazyan 97].

1.2. Motivation

Tactile imaging has been shown to reduce the subjectivity of clinical palpation, in that the tactile image generated is relatively clinician-invariant [Wellman 01]. The tactile map generated, however, has not yet been linked quantitatively to the underlying tissue properties such as stiffness. This information promises to be of clinical relevance to the detection and management of disease [Kopans 00, Ronnov-Jessen 96]. In this work we seek to come up with a method for estimating these underlying tissue parameters from the information collected during tactile imaging.

A direct application of this parameter estimation is breast cancer screening. The current gold standard for breast cancer detection is based on the difference in radioopacity of normal and pathological tissues, however breast stiffness and the presence of lesions are

correlated to breast health [Jatoi 97]. Tactile imaging holds promise for improving breast cancer screening by quantifying palpation and adding a repeatable, reliable imaging modality based on tissue mechanical properties. Therefore, in this study, we also seek a method to integrate tactile imaging with mammography, so that combined with the tissue parameter extraction discussed above a foundation will be laid for improving breast cancer screening.

1.3. Thesis Scope and Outline

The purpose of this work is to further the utility of tactile imaging by expanding the scientific understanding of tactile information. The research presented here concerns two aspects of tactile imaging, which can be applied together in a clinical setting to aid in breast cancer screening by providing quantitative information not currently available clinically. The first part concerns extracting absolute tissue information from the tactile data, specifically information such as size and stiffness of embedded inclusions. The second part uses tactile maps collected in a screening setting and concerns the utility of these maps to a screening radiologist.

The rest of this chapter provides background information detailing specifics on the tactile imagers used in this study. An overview of breast cancer and the imaging modalities currently used in screening are presented to provide context for the scope of most of the work presented in this thesis. Other organs, which may benefit from the application of

tactile imaging, are also discussed since the work presented here will be applied to organs besides the human breast.

Various aspects of parameter estimation from tactile information are presented in the following three chapters. Chapter 2 deals with the basic problem of a round lesion attached to the substrate of a soft layer of tissue. We attempt to find a closed form analytical solution to the problem and discuss the work of other researchers in this topic. A new algorithm, which can estimate the underlying stiffness and geometry parameters of such a structure, is developed on models with parameters in the range of physiological breast parameters. Tactile Scanning, a new way of examining each frame of tactile information, is presented, and forms a basis for the work in this chapter. The algorithm is tested both on finite element data and physical models. The results show an improvement upon the work of previous estimation attempts.

Chapter 3 extends the utility of the parameter estimation algorithm developed in chapter 2 to a more complex problem. Specifically, this chapter considers the case of a lesion embedded in tissue but not attached to a rigid substrate. With only a slight modification, the algorithm is shown effective on finite element data of this case. This estimation work is extended to include lesions softer than the background, such as the nonpathological case of large hollow vessels in liver tissue. Porcine livers are imaged with the laboratory tactile imager, and used as a physical test bed for the algorithm developed.

Chapter 4 concerns the general case of estimating parameters of an underlying tissue stiffer than the surface layer. We characterize the tactile scanning system as a linear system and find its impulse response over a range of tissue parameters. This allows for continuous estimation of the underlying parameters, while providing a better understanding of the limitations of tactile scanning.

The work presented in chapter 5 concerns registering tactile maps of the breast to mammograms. This requires an understanding of the different types of deformation inherent in obtaining the two images. We develop models to quantify the deformations resulting from the different compressions, and use this information to generate an algorithm to register tactile maps to their corresponding mammograms. The algorithm was applied clinically in a small study, and can be applied more widely to study a possible increase the positive predictive value of screening mammography.

1.4. Background

1.4.1. Tactile Imagers

The two tactile imagers used in this study are shown in figure 1.1. The radius of curvature for both sensors is 3.8 cm, which is optimized for recording maps on the human breast [Wellman 99]. The clinical tactile imager (figure 1.1a) uses a 26x16 array of resistive pressure sensors, each 1.5mm apart on center, to record tactile frames at 16Hz.

The location and orientation of each tactile frame are determined by a magnetic tracker incorporated into the plastic handle. The tracker must work in the vicinity of the magnetic transmitter, and in the absence of electromagnetic interference, the position of each frame can be determined to an accuracy better than 2mm for a 30cm work area. The resistive pressure array of this imager is prone to a random noise caused by the mechanics of the resistive ink in each sensor, and as such even with calibration we can expect gaussian noise with a standard deviation of 10% of the signal in each tactile frame collected.

The laboratory tactile imager used in this study is shown in figure 1.1b. This imager employs a 16x16 array of capacitive pressure sensors spaced 2mm apart on center to record tactile frames at 10Hz. This imager has two modes of operation, depending on whether the tactile information sought is to be collected on a straight line or in a 2-D map. For maps collected in a straight line, the imager can be mounted on a linear driver, whose positional accuracy is less than a millimeter. For tactile information collected anywhere in space, the same magnetic tracker as in the first tactile sensor is utilized. The capacitive pressure sensors are less prone to random noise than the resistive sensors, however noise upwards of 5% is commonly found in practice.

1.4.2. Breast Anatomy and Pathology

The breast, by virtue of being an external organ, is an ideal candidate for full tactile imaging, and the great social impact and high prevalence of breast disease are good cause to examine the role that tactile imaging may play in breast cancer screening and detection. In this section we present an overview of the anatomy and pathology of the human breast to provide context for the work of this thesis.

Anatomy

The human female breast, after puberty and before menopause, is made up of glandular tissue (the mammary glands), adipose tissue (fat cells), and supporting tissue (stroma, mainly collagen and elastin fibers). The general anatomy of the breast is shown in figure 1.4. The glandular tissue, located in a cone with its apex at the nipple, is the site of milk production. The adipose tissue, in layers under the skin and above the chest wall, is the greatest contributor to the general shape and size of the breast. The supporting tissue is thin and sparse and affects mainly the gross appearance and motion of the breast.

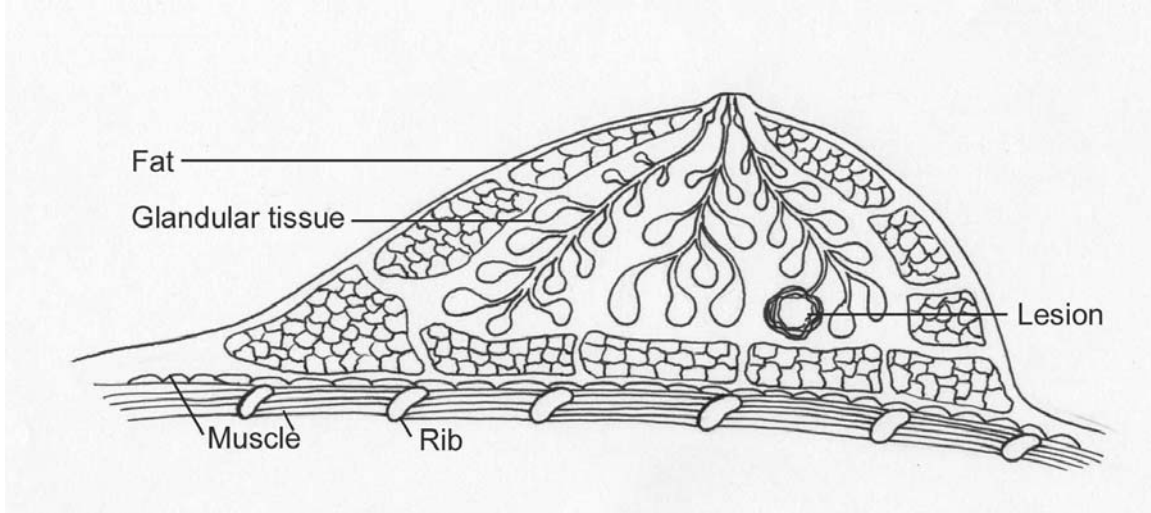


Figure 1.4. General anatomy of the human female breast, after puberty and before menopause. The glandular tissue is essentially a cone-shaped area under the nipple, with an extension superolaterally into the axilla (towards the armpit) to form the axillary tail. The adipose tissue (fat) naturally occurs in layers under the skin and above the chest wall. This figure also shows a small lesion growing from the cells that line a terminal gland.

Menopause marks the conclusion of replacement of the glandular tissue by fat in a process called involution. Although there is a great variety in timing between individuals, involution of the breast begins at about 30 years of age and continues until menopause during a period called perimenopause. Involution manifests as the glandular component atrophies and is replaced in discrete sections by adipose tissue until the entire glandular component is replaced. The other components of the breast also undergo menopausal changes. Specifically, the volume of adipose tissue increases, while the elastic and collagen fibers weaken.

Examination of the breast by palpation yields very different results depending on the relative age of the subject. A premenopausal breast has a high glandular tissue component under the superficial adipose tissue, leading to an inhomogeneous texture.

Postmenopausal breasts, on the other hand, are far more uniform, and the adipose tissue is softer and easier to palpate in searching for stiff pathologies.

Mechanical Properties

Biological tissues are generally viscoelastic and strain-hardening [Fung 93], and the tissues found in the human breast are no exception [figure 1.5]. Under slow manipulation, however, ($\sim 1\text{Hz}$) viscoelasticity effects are minimal [Wellman 99] and can be ignored for all of the breast tissues in question. The supporting tissues plays a role when the breast is under tension, however under compression they offer negligible structural support, and naturally occupy such a small volume of the breast that their presence under compression can be ignored. Local mechanical properties, especially with the breast supported against gravity and examined in compression, are thus determined almost entirely by the glandular and adipose tissues. Adipose tissue exhibits linear elastic behaviour through strains of 15% and in this linear regime has a Young's modulus of $15\pm 4\text{kPa}$. Glandular tissue exhibits linear elastic behaviour through strains of 6% at a Young's modulus of $45\pm 6\text{kPa}$ [Krouskop 02, Wellman 99].

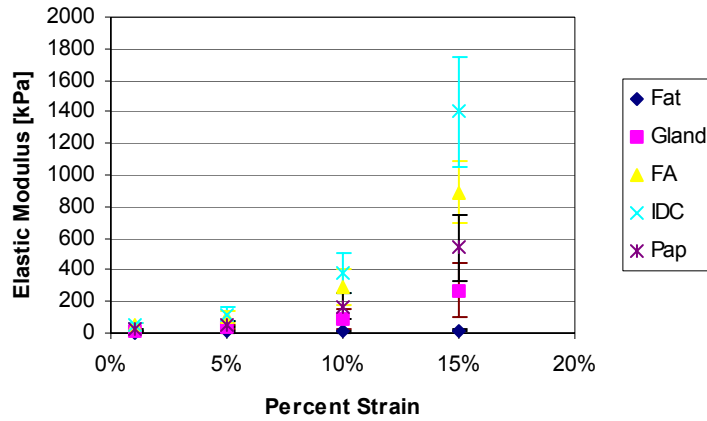


Figure 1.5. Breast Tissue Modulus Variation (data from Wellman 99). Legend: Fat (normal adipose tissue), Gland (normal glandular tissue), FA (benign Fibroadenoma), IDC (malignant Intraductal Carcinoma), Pap (precancerous Papilloma).

Pathological tissues are even stiffer than glandular tissues, and so can be felt as distinct under palpation, and viewed as stiffer in tactile imaging. The clearest distinction is made in postmenopausal breasts in which the background is almost entirely soft adipose tissue, however due to the distinct modulus, pathologies are often felt under palpation even in premenopausal breasts.

Roots of Pathology

Glandular tissue is the most metabolically dynamic tissue in the breast, increasing and decreasing its volume and cellularity with menstruation and pregnancy. This property of glandular tissue results in this tissue being the source of almost all pathologies indigenous to the breast [Lester 99]. Problematic pathologies are detected as they grow to differentiate themselves from their glandular tissue source. It is suspected that most pathologies, especially malignant tumors, have an initial dormant phase of little growth,

where they remain less than 2mm in size [Grundfest 88]. After a variable amount of time (which can be as long as decades) they begin to grow rapidly. As the glandular tissue involutes, the pathology does not, and remains behind as an island of stiff tissue among soft fat. The latency in the active growth phase is the reason that most breast cancers are found in post-menopausal women who have little to no glandular tissue left to generate new growths.

Breast Cancer Statistics

In America, the chances that a woman will develop breast cancer in her lifetime (assumed to be 85 years) is now one in eight [Imaginis 03]. Breast cancer accounts for one-third of new cancer cases, making it second only to skin cancers as the most common cancer in women. Of these 175,000 new cases of invasive cancer each year, more than 43,000 women will die from the disease, making breast cancer the leading cause of cancer death of women next to lung cancer. Men, too, are not spared from this disease, with 1,300 new cases diagnosed each year in the United States, and 400 deaths. The occurrence of breast cancer is not uniform across each region of the breast, with a disproportionate number of cases found in the upper outer quadrant of the breast [figure 1.6]. The age breakdown of breast cancer cases is shown in figure 1.7.

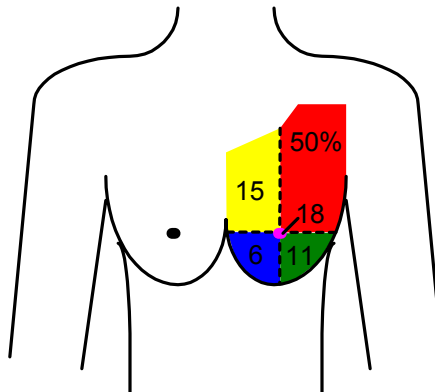


Figure 1.6. Incidence of breast cancer in the nipple and four quadrants of the breast. The upper outer quadrant has a disproportionate number of cases.

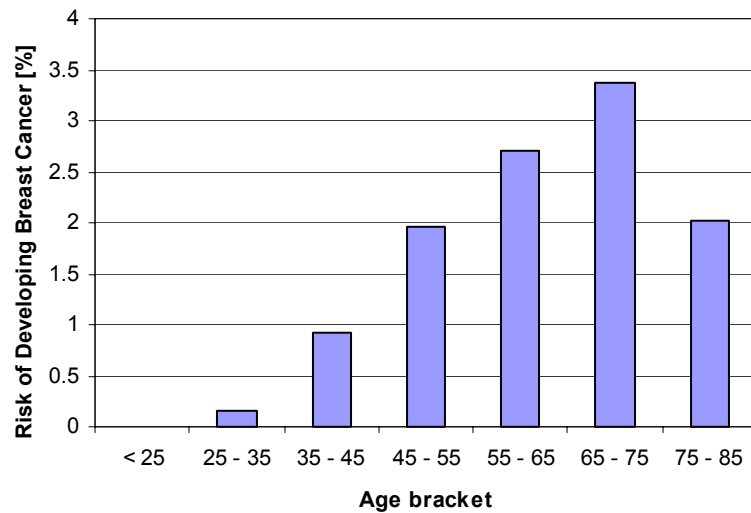


Figure 1.7. A woman's risk of developing breast cancer in age brackets indicated. Data from Komen [03].

A woman's aggregate risk of a breast cancer diagnosis increases as she ages, with a large increase around age 50. From table 1.1 we see that this coincides with the modal age of menopause.

Table 1.1. Onset of menopause. Data from [Taber 97]

By age...	% of women
47	25
50	50
52	75
55	95

From this we see that the vast majority of breast cancer cases occur in postmenopausal women, whose breasts are composed almost entirely of fat. The high modulus contrast between the pathology and the background tissue in postmenopausal women make this an ideal situation for tactile imaging. The high prevalence of breast cancer in modern society provides us not only with a disease for which we can easily find clinical subjects, but also with a disease in which even a small percentage increase in the effectiveness of clinical care can make a large impact on many lives.

1.4.3. Imaging Modalities for Breast Cancer Screening

Until more than halfway through the 20th century, the only screening tool for breast cancer was feeling for lumps in the breast with the fingerpads. In 1963, a large screening mammography study was funded in New York [Friedlander 99] and a 30% decrease in long-term mortality from breast cancer was observed in the participants. Although no one imaging technique is perfect (or else one might argue that the mortality rate would be zero) mammography offered both a new tool which can detect lesions by a different criteria than was previously available, and also, by mandating screening, it brought about a greater awareness of breast cancer, which at the very least leads to better self examinations, if not more thorough clinical assessments.

Today, the triad of self breast exam, clinical breast exam, and mammography are the mainstay of breast cancer screening. It is recommended that every postpubertal woman

performs a self exam monthly, and has a clinical breast exam at least yearly [ACS 03]. Biannual mammograms are suggested for women 40-50 years of age (with some organizations recommending yearly), and yearly thereafter. Despite this screening regimen, however, breast cancer rates are still very high, and missed or delayed diagnosis of breast cancer is the leading cause of medical malpractice suits [Pennypacker 99].

Breast Self Exam

It is recommended that all women perform breast self examination (BSE) monthly, to develop a routine and a knowledge of their breasts, so that they can better feel any changes. A breast self exam entails visual inspection for any changes in the breast contour (since pathology can sometimes affect the skin or ligaments of the breast, causing distortion) and manual palpation of the bulk of the breast. A recent study concluded that an average woman would have sensitivity and specificity scores of 46% and 61%, respectively, but that with training on proper technique and what to look for, these numbers change to 59% and 57 % (specificity decreases due to the increase in total number of lumps found) [Barton 99]. Although the percentage of women who perform them regularly is not known, and is expected to be quite low.

Clinical Breast Exam

A clinical breast exam (CBE) is similar to the self breast exam that women should perform on themselves monthly. As with BSE, a CBE begins with the clinician

observing the movement of the breasts with arm motion while the woman sits or stands. The woman then lays supine and the clinician manually palpates the breast by pressing gently with the pads of the fingers until all the breast tissue is covered. The clinician feels for nodules which exhibit the three D's: Discrete, Different, and Dominant, although most diagnoses from CBE are based on qualitative experience. Sensitivity and specificity of CBE are estimated at 54% and 94%, respectively [Barton 99].

The causes of palpable breast lumps can be broken down as follows [Tavassolis 96]

- fibrocystic changes 40%
- no major pathology (i.e. normal) 30%
- benign diseases 13%
- cancer 10%
- fibroadenoma 7%

It has been shown that a trained clinician can feel a lump as small as 3mm in diameter [Pennypacker 99], however the diagnostic ability of the CBE is highly dependent on the clinician administering the test. A proper CBE takes time and can make some patients and clinicians feel uncomfortable, and is not often performed in full.

Mammography

Mammography works on the same principle as any X-ray, though since the breast is solely made up of soft tissue, it is a very low dose exposure. The breast is compressed between two flat parallel plates to obtain the maximum tissue spread and thinnest profile possible. Photons in the X-ray frequency range pass through the top plate, through the breast tissue, and expose photographic film in the bottom plate. The X-rays pass through

some tissue preferentially over others. Regions of calcification, for example, are considered “radio-opaque”, and the x-ray image (which is effectively a photo negative) will remain white under these regions. Since mammography uses very low doses, a small calcification (on the order of a mm) can easily be picked up. Other areas of radiologically dense tissue, however, prove to be more difficult, and are subject to the experience and expertise of the radiologist reading the film. A clinically occult carcinoma can appear as microcalcifications or a stellate mass on mammography, and so in general, any areas of calcification and most irregular densities are tagged as suspicious and are recommended for biopsy. If a region of calcification that is clinically occult is excised, the excised specimen is reimaged after pathological examination to confirm that the lesion of concern was indeed excised.

Although the reading of mammography films remains highly subjective, there are many that believe that mammography “is the most accurate imaging technique available for the diagnosis of breast cancer” [Hermann 92]. In fact, there are many lesions which it cannot pick up, and many false positives, as benign densities often appear as opaque as cancers on film. This is reflected in the sensitivity and specificity numbers of about 80% and 40%, respectively. Friedlander [99] summarized the strengths and weaknesses of mammography by stating:

“Mammography continues to be the best screening tool for the detection of breast abnormalities, especially for older women. It appears to have

limitation for those with dense breast tissue or women using hormone replacement.”

Despite its limitations, and the fact that it is very uncomfortable (and even painful) for many women, mammography continues to be the most common screening tool used for breast cancer.

Tactile Imaging and Breast Cancer Screening

Although breast cancer screening ideally involves information from both palpation and mammography, the information from the various imaging modalities is rarely assimilated. The manner in which each modality is performed plays a large role in this. Clinical breast exams are performed by a clinician with the woman laying supine. Mammography, on the other hand, is performed by a radiologist with the woman standing. Combining the qualitative information from the ventral-dorsal plane with the more quantitative radiographic information obtained in an entirely different plane is difficult at best, and due to the different practitioners is not often done in a screening setting. Tactile imaging stands to bridge the gap between the two pieces of information, by providing a quantitative image of palpation that can be obtained in the same plane as a mammogram.

1.4.4. Other Organs

Tactile information is useful in organs other than the breast, particularly in solid organs such as the liver, spleen, and prostate. Because of the liver's size and the prostate's location, palpation is regularly used in assessing the health of these organs. A prostate screening exam consists of a blood analysis and manual palpation of the prostate, while in cases of liver surgery, distinct pathology under the surface is located by the surgeon using manual palpation to outline the area of stiffness. Here we present a basic overview of liver anatomy and pathology as background for the work in this thesis. The breast and liver provide ideal first test-beds for establishing the utility of tactile imaging since a direct relationship between modulus and pathology for both the parenchyma and embedded inclusions is currently being explored in these organs [Kopans 00, Sanada 00].

Anatomy and Pathology of the Liver

The average human adult liver is wedge-shaped and weighs 1200-1600g [figure 1.8]. Its thickness varies from 6-12 cm at the midclavicular line to 4-8 cm at the midsternal line. Its parenchyma is composed of isotropically distributed lobules, and is contained in a thin fibrous capsule that surrounds the entire organ. The liver parenchyma, like most biological tissues, exhibits viscoelastic behaviour and a nonlinear stress-strain curve. In the linear regime under slow compression, its modulus can be approximated as 10kPa [Ottensmeyer 01].

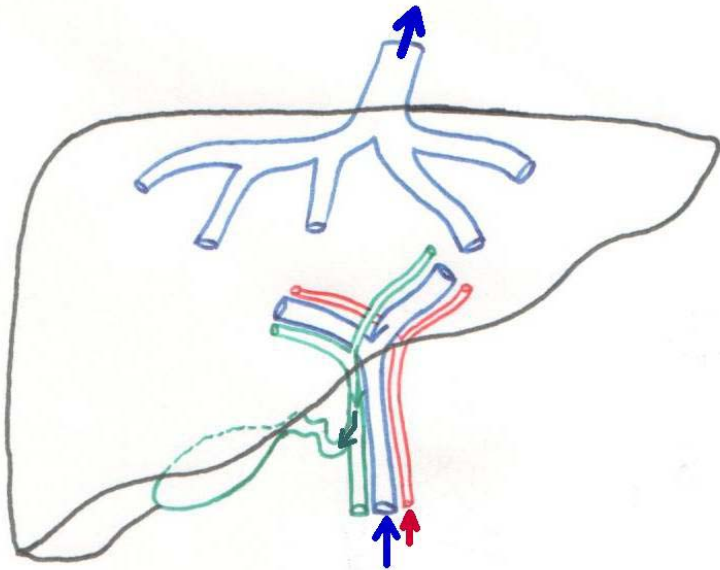


Figure 1.8. Human Liver Anatomy. The liver parenchyma is macroscopically homogenous and isotropic, save for the few large vessels that run through the center of the liver. The arteries, bile ducts, and portal vein (“portal triad”, entering from the bottom) are well-enmeshed with the liver parenchyma, however the hepatic vein (large vessel leaving through the top) presents a cylindrical gap in the tissue, due to its low blood pressure and large volume. The arrows indicate the direction of fluid flow. The green sac at the bottom of the liver is the gall bladder.

The liver receives 25% of the total body blood flow in its task of eliminating toxins from the blood. As such, it has an extensive system of vessels, both at high pressure (hepatic artery) and at low pressure (portal vein, hepatic vein, bile duct). These vessels enter the liver as relatively large tubes, and in the case especially of the hepatic vein, continue to be a significant part of the liver cross-section at distal locations [figure 1.9]. The shape of the hepatic vein is actually determined by the cylindrical void created for it by the hepatocytes, and this void plays a role in determining the mechanical properties of the liver.



Figure 1.9. Porcine Liver Lobe. This is one of the five distinct lobes of a porcine liver. Thin slices (right) of the lobe show the large hepatic veins that run along the main axis of the liver and remain open even without perfusion.

Liver cirrhosis is a sadly common condition which leads to liver failure and is one of the top ten causes of death in the Western World [Crawford 99]. Cirrhosis leads to an increase in diffuse liver stiffness due to the formation of scars between the lobules. Each scar is very small and thin, however their abundance leads to changes in the gross properties of the liver. Studies have shown that the extent of disease correlates well to the modulus of the liver [Sanada 00]. Most other liver pathologies manifest locally, generally resulting in round lesions stiffer than the background parenchyma. These are differentially diagnosed from blood tests, symptomatic assessment, and x-rays, and are excised by surgeons who feel for their round, stiff, presence under the liver surface with their fingers.



Figure 1.10. Advanced Liver cirrhosis with hepatocellular carcinoma. The overall stiffness modulus of the liver is greater than normal. The abnormal nodules are stiffer yet, and started out much smaller.

Porcine organs, including the liver, have been used extensively as a testbed for the study of their human counterparts [Carter 01, Ottensmeyer 01]. Porcine organs in general are structurally and functionally similar to their human counterparts, however porcine livers are more collagenous than human livers, and as such are characteristically stiffer, with a modulus in the elastic regime of 15 kPa. Porcine livers also display a distinctly lobulated structure, which each lobe containing its own venous structure. The large portal veins in the porcine liver traverse the middle of the lobes' parenchyma [figure 1.9]. Smaller venules branch off the main vein at sharp angles to supply the peripheries of the individual lobes.

Chapter 2

Fixed Lesion Parameter Estimation

2.1. Introduction

Breast stiffness is a recognized indicator of breast health [Ronnov-Jessen 96]. Absolute stiffness changes over the course of a woman's reproductive life, and deviations from expected stiffness ranges can signal an underlying pathology. Diffuse granularity and increased background stiffness are hallmarks of fibrocystic changes [Lester 99], and may indicate an increased risk for breast cancer [Thomas 97]. A discrete lump can indicate the presence of local pathology, be it a fibroadenoma, cyst, or malignancy. These different pathologies present with varying physical characteristics such as stiffness and mobility [Kopans 00].

Using palpation to feel breast stiffness locally (as in a lump) and diffusely is an established screening mechanism for assessing breast health [Evans 99]. Women are advised to obtain Clinical Breast Exams (CBE) at regular intervals [Jatoi 97] and to perform Breast Self Exams (BSE) at home [ACS 03]. Reproducibility and efficacy of

CBEs is limited by the experience of the clinician and by human variability [Pennypacker 99, Lavin 80].

A method for noninvasively estimating breast stiffness and lesion size and stiffness holds promise of clinical utility. As discussed in chapter 1, different breast pathologies occupy different regions on the stiffness scale, and so knowing the stiffness of a lesion can help in lesion identification and disease management. Lesion size, as well, is an important factor in assessing the extent of disease. Even in the absence of a lesion, the general stiffness of the breast may correlate well with breast cancer risk [Kopans 00].

Tactile images contain modulus and geometry information. In this chapter we develop an algorithm for using tactile information to quantify parameters of soft tissue with stiff inclusions in a simple geometry that models many cases of breast pathology. In subsequent chapters, we will expand the algorithm to more complicated cases that encompass other cases of breast pathology as well as structures in other organs. Along the way, we introduce a new way of handling tactile data, called Tactile Scanning, that will enable us to estimate the parameters of interest from tactile information.

2.1.1. Problem Statement

With few exceptions, breast pathologies originate in the glandular tissue of the premenopausal breast. Most remain in a benign dormant state for many years, while the

breast undergoes involution and the surrounding glandular tissue is replaced by fat. Therefore most lesions, although arising from glandular tissue, are found amid the soft fat of the postmenopausal breast. Specifically, since most lesions arise from the milk-producing cells at the terminal end of the glandular tissue, most of these lesions are not near the surface of the breast, but rather near the chest wall, with a layer of fat between them and the skin.

Mechanical forces at play in the growth of the lesions help to keep the lesions round in shape. The thin basement membrane that anchored the cells of the originating duct remains and grows, resulting in lesions that have smooth, distinct borders. A few sample lesions are shown in figure 2.1. These benign and malignant lesions are representative of the lesions commonly encountered in breast pathology.

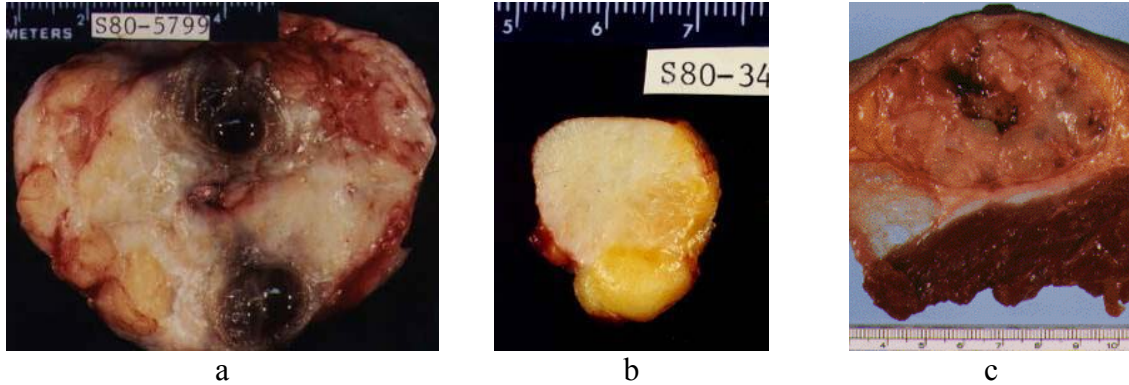


Figure 2.1. Gross anatomy of various breast pathologies. (a) Cysts in fibrocystic tissue. (b) Glandular cell tumor. (c) Ductal carcinoma that has invaded beyond this focal site. Note that each pathology manifests as a round lesion. Images from Transmed [97], used with permission.

In light of the general shape and position of many breast pathologies, we propose the model shown in figure 2.2 for the basis of our study. The tissue is modeled as a soft slab

of constant thickness in the vicinity of the lesion. The indentor is a rigid cylinder of finite length that is pushed into the tissue over the lesion. The lesion is spherical and is attached to the rigid tissue substrate. The interaction between the indentor and the tissue is assumed to be frictionless. We shall devise a method for estimating the four salient parameters of background thickness, t , and modulus, B , and lesion size, d , and modulus, L , from the pressure information collected at the interface between the tactile imager and the tissue surface.

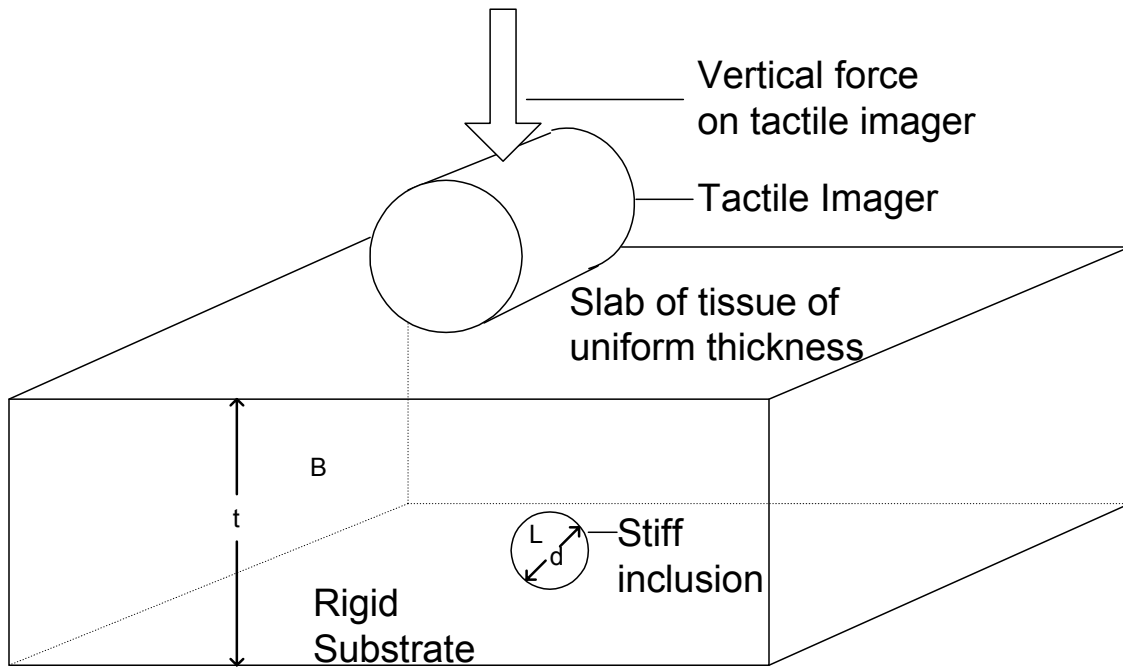


Figure 2.2. Idealized model for the study of parameter estimation from tactile information. The lesion is approximated as a round mass, stiffer than the background, attached at one point to a rigid substrate. The background tissue near the lesion is assumed to have a constant thickness t . The lesion diameter is d . The modulus of the background and lesion are B and L , respectively.

2.1.1.1. Simplifying Assumptions

The full problem as depicted in figure 1.4 is to estimate the modulus in every point in a three-dimensional breast. This is a complex three-dimensional problem that has no closed-form expression. Figure 2.2 shows the idealized problem of interest. If we focus on the centerline of the problem, the problem simplifies to that shown in figure 2.3. As a first approximation, we will consider the two dimensional model of figure 2.3 as a plane strain model, thus representing a long cylindrical lesion embedded in tissue and indented by an infinite cylindrical scanhead. We approximate the healthy breast tissue as a slab of material with finite thickness which is fixed to a flat, incompressible chest wall. The lesion, stiffer than the background tissue, is also attached to the chest wall at one point. We will assume that both materials in the slab are linear elastic and isotropic, and are perfectly bound to each other. These assumptions are all based on physical data, and will now be discussed in more detail.

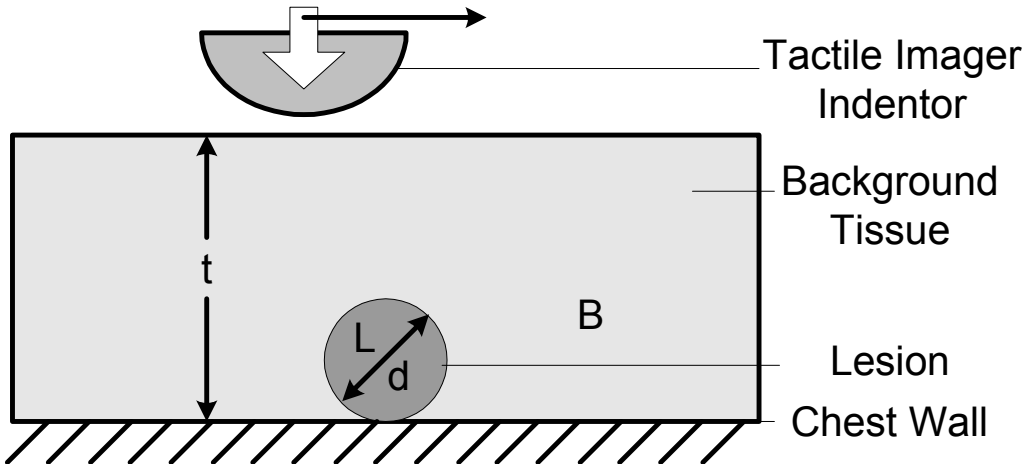


Figure 2.3. Centerline of the problem of interest. The arrows at the indentor indicate the direction of force (clear arrow) and motion (line arrow). Our goal is to develop a method of estimating the four parameters indicated from surface contact pressure information collected via tactile imaging.

Tissue of Constant Thickness

Our assumptions require a swath of tissue of approximately constant thickness for a few centimeters near a breast lesion. This is not physically unreasonable, especially considering that most breast lesions are found in the upper outer quadrant of the breast [ACS 03], where the soft tissue is relatively thin and flat.

Round Lesion

There is no body of literature that documents the validity of this assumption. Previous work performed by Wellman [99, 01] employed this assumption in the generation of an inversion algorithm and tested the algorithm on clinical lesions. The clinical results were found to match well with the results on models with round lesions, when one considers the main diameter of the physical lesion. This leads us to accept round lesions as an adequate model to clinically relevant lesions.

Lesion Attached to Substrate

This assumption is made only for the work in this chapter, and will be expanded on in chapter 3.

Homogenous Isotropic Tissues

The main tissues of the breast are glandular, adipose, and fibrous tissues. Glandular and adipose tissues are well modeled by isotropic materials [Thomas 97]. Fibrous tissue, however, is highly directional. Tactile imaging is performed as small compressions with

the breast relaxed. Under these conditions, the sparse ligaments and other fibrous tissues that traverse the breast do not affect its gross mechanical properties and thus the bulk of the breast is well modeled by an isotropic material.

Although each of the glandular and adipose tissue found in the breast can be macroscopically modeled as a homogenous material, in premenopausal breasts the bulk consists of both glandular and adipose tissue. Most breast cancers, however, as discussed in chapter 1, are found in postmenopausal women, where the glandular component is in large part absent. Postmenopausal breasts are therefore well modeled by a single homogenous material, and we will study the effect of varying the stiffness of this material from that of adipose tissue to glandular tissue.

Most pathologies in the breast are composed of a few cells in a disorganized network of fibrous tissue [Ronnov-Jessen 96]. The disordered nature and high density of the fibrous tissue in the lesions provide for homogenous isotropic material properties.

Incompressible Linear Elastic Materials

Biological tissues, by virtue of being comprised mainly of water, can be considered incompressible [Fung 93]. The elastic modulus is shown versus the strain for various breast tissues in figure 1.5. The elastic modulus clearly increases for higher values of strain. This effect is small for the softer tissues such as fat and is far greater for the stiffer tissues. For the entire range shown, fat can be modeled as having a constant modulus with little error. The error in assuming a single elastic modulus increases for stiffer tissues. We can keep the absolute error in lesion modulus to 30% by limiting the strain to 4%.

Frictionless Contact

This assumption is applicable to real tactile imaging situations as long as the surface of the tissue is well lubricated. This is standard procedure with clinical tactile image collection.

Plane Strain

We shall use this assumption to generate an inversion algorithm to estimate the parameters from tactile data. We will test our algorithm on three-dimensional models, which will intrinsically test the validity of this assumption.

2.1.2. Previous Work

The estimation of lesion parameters in tactile imaging has been explored most notably by Wellman [99, 01]. He assumed the model of a round lesion in a homogenous fatty tissue on a stiff substrate as shown in figure 2.3. Wellman showed that finite element analysis on the plane strain problem of the centerline can be used to accurately predict the centerline interfacial pressure distribution of spherical lesions. He used these two dimensional finite element models to devise a tactile map feature-based algorithm to predict the diameter and depth of a very stiff lesion in soft tissue. His results were limited to lesions at least 100 times stiffer than the background fat, which applies only to cases of the stiffest cancers. Nevertheless, he showed that his algorithm's predictions are

more accurate in determining the size of a stiff spherical region than manual palpation [Wellman 01].

Weber [00] reproduced this work and attempted to find a more complete set of lesion parameters that includes the elastic modulus of a lesion of linear elastic material. His method was limited in accuracy, even with the input information of imager displacement, and the accuracy was dependent on the ratio of tumor modulus to background modulus.

Both Wellman and Weber relied on fitting Gaussian curves to discrete-lump tactile maps in order to extract features useful for the inverse model [figure 2.4]. Based on a Gaussian fit, they extracted base, amplitude, and standard deviation features. Although this method has merit, as evidenced by the inverse models already established, it is limited in the features used to establish the inverse model, and potentially useful information is ignored in a Gaussian fit.

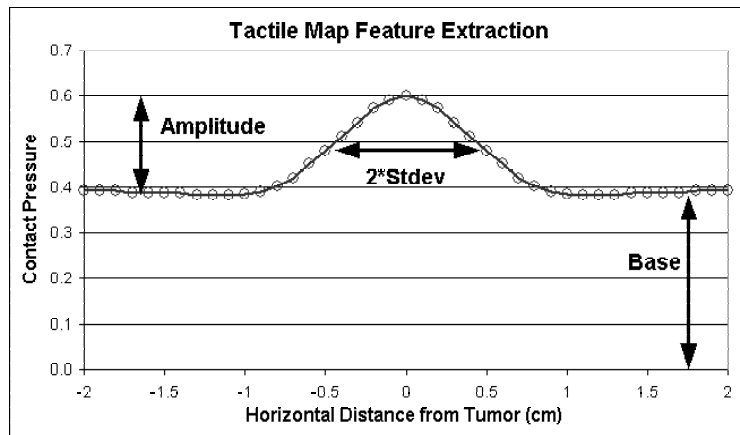


Figure 2.4. Centerline tactile map with extracted features amplitude, base, and standard deviation (Stdev). The tactile map shown here was assembled from finite element data. Note the similarity to a Gaussian curve. Previous work in parameter estimation has relied on the gaussian features indicated. From Weber [00].

Sarvazyan et al [Sarvazyan 97, 98a, Niemczyk 96] have also studied the efficacy of tactile imaging in the detection of cancer, most notably in the prostate. The lesion-detecting algorithm they employ is based on different principles than the algorithms employed by Wellman and Weber. Sarvazyan [98b, 99] captures tactile data collected at different input forces and compares it to an expected anatomy-based map in order to pinpoint areas of mechanical heterogeneity in the organ. To date, the specific parameters of lesion size and elasticity modulus have not been an output of the algorithm employed. Rather, their work has shown that tactile imaging information can provide a Boolean assessment of whether each of the two lobes of the prostate contains a lesion more accurately than a digital rectal exam.

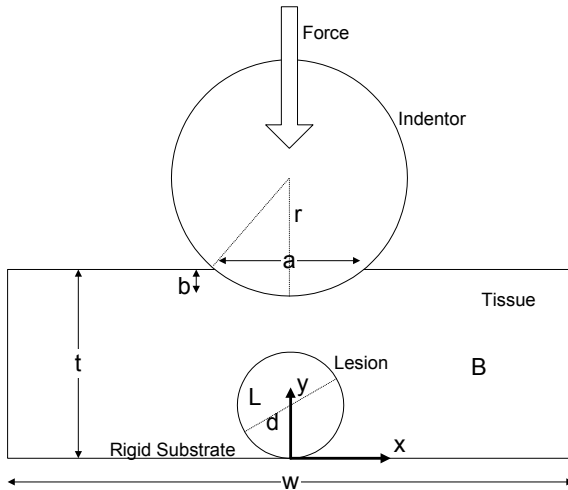
2.1.3. Analytical Solution

The goal of this work is to develop a method for estimating the parameters of tissue from tactile information. This can be seen as an inversion of the relationship between the tissue parameters and the tactile data. Analytical investigation is the most direct way of establishing the mathematical relations between the parameters and the surface stresses produced by normal displacements of the top surface by a cylindrical indentor. There is a body of historical work on the analysis of similar problems, and we look to these first to facilitate our solution.

The first analysis of the stresses of two cylindrical elastic bodies in contact was presented by Hertz in 1882 [Johnson 1985]. He developed a closed-form solution that described the stresses within the entire continuum based on the assumptions of small strains and nonconforming bodies. Goodier [36] developed analysis for stresses in an infinite medium with a spherical inclusion. Eshelby [57, 59] extended this work to an infinite medium with an ellipsoidal inclusion, but focused on stress fields that result from a homogenous field inside the inclusion, which is not applicable to our problem of interest.

Yu and Sanday [91] expanded on this previous work and dealt with the stresses in bonded semi-infinite half-spaces with an inclusion. The geometry for their work is the most similar to the geometry of the current problem, however their work assumes a homogenous field in the inclusion. The work presented here requires surface stresses due to surface displacements, which will not result in a homogenous field in the round inclusion.

There is no existing solution that can be applied to this specific problem, so we return to the two-dimensional problem of figure 2.3 and attempt to find an analytical expression for the pressure at the interface between the indenter and the tissue as a function of the parameters of interest. Figure 2.5 shows the axes and important parameters of the problem and summarizes the assumptions that will be made in seeking a solution.



Assumptions:

- Rigid substrate and indentor
- Incompressible tissues
- Isotropic linear elastic tissues
- Homogenous inclusion in homogenous tissue
- Frictionless contact
- Two dimensional plane strain model

Figure 2.5. Simplified 2-D problem (width $w \rightarrow \infty$) with relevant quantities indicated, and physical assumptions.

We will first tackle the problem as depicted in figure 2.5, and look for the analytical solution to the pressure profile when the indentor is directly over the lesion. As with all mechanics problems, the solution must satisfy the equations of geometry, equilibrium, compatibility, and the constitutive relations:

- Geometry:

The strain tensor $\underline{\varepsilon}$ is defined by its relationship to the displacement \underline{u} of the body

$$\underline{\varepsilon} = \frac{1}{2}(\nabla \underline{u} + \nabla \underline{u}^T).$$

- Equilibrium:

Force equilibrium in continuum mechanics becomes

$$\nabla \cdot \underline{\sigma} + \underline{f} = 0$$

where $\underline{\sigma}$ is the stress tensor and \underline{f} the local force tensor.

Establishing momentum equilibrium requires a symmetric stress tensor (i.e. the stress on the x -plane in the y -direction is equal to the stress on the y -plane in the x -direction, etc.)

$$\underline{\sigma} = \underline{\sigma}^T.$$

- Compatibility:

For this two-dimensional problem, the only nontrivial compatibility relation that remains to be satisfied for a unique solution is

$$2\varepsilon_{12,12} - \varepsilon_{11,22} - \varepsilon_{22,11} = 0,$$

where the subscripts $,ij$ imply derivatives taken in the i and j directions.

- Constitutive Relations:

Continuous media can be characterized by the two dimensional relation

$$\sigma_{ij} = C_{ijkl} \varepsilon_{kl}.$$

Here σ and ε are 2-tensors, due to the symmetry of σ , as stated in the moment equilibrium equation.

The solution to the above equations is subject to the boundary conditions on all surfaces. In this case, we have zero displacement on the bottom edge, a fixed displacement in the shape of the scanhead in the region under the tactile imager, and zero stress on the sides and the areas of the top surface not in contact with the scanhead. We also have zero

shear stress under the scanhead, which follows from the assumptions of slack skin and a frictionless contact. These can be expressed as:

$u_1(x, y = 0) = u_2(x, y = 0) = 0$	Bottom attached to rigid substrate
$u_2(-a/2 \leq x \leq a/2, y = t) = -(r^2 - x^2)^{1/2} + r - b + t$	Displacement under indentor
$\sigma_{11}(x = \pm w/2) = 0$	Stress-free left and right edges
$\sigma_{12}(x = \pm w/2) = 0$	Shear stress-free left and right edges
$\sigma_{22}(x > a/2, y = t) = 0$	Stress-free surface away from indentor
$\sigma_{12}(y = t) = 0$	No surface shear stress

Note that at the interface between the background tissue and the inclusion, displacements are continuous across the inclusion boundary, although stresses will not be due to the different material properties.

Subject to equilibrium considerations, we impose the subjective constraints $\phi_{,11} = \sigma_{22}; \phi_{,22} = \sigma_{11}; \phi_{,12} = -\sigma_{12}$ to the sole non-trivial equation of compatibility. The compatibility equation can then be written as $\phi_{,1111} + \phi_{,2222} - 2\phi_{,1122} = \nabla^2 \nabla^2 \phi = 0$. Solution of the problem now entails finding suitable base functions for ϕ , the Airy stress function, that satisfy the boundary conditions.

In terms of ϕ , the boundary conditions at the top surface are

$$\sigma_{12}(x, y = t - d/2) = 0 = \phi_{,12}(x, y = t - d/2)$$

$$\sigma_{22}(|x| > a/2, y = t - d/2) = 0 = \phi_{,11}(|x| > a/2, y = t - d/2).$$

The normal stresses under the indentor,

$\sigma_{22}(|x| < a/2, y = t - d/2) = \phi_{,11}(|x| < a/2, y = t - d/2)$, are actually the desired solution.

The problem at hand is to find the boundary condition that is consistent with the Airy stress function formulation. We can either guess a boundary condition, establish functions for the Airy stress function that seem reasonable based on the known boundary conditions, and use that to validate our guess of the desired boundary conditions, or we can conjecture the proper form of the Airy stress function based on the known boundary conditions and assume that that form holds for under the indentor, thereby establishing the boundary conditions.

In either case, the solution is not guaranteed to be exact, as it is approached iteratively. The problem statement itself, therefore, which requires finding the contact stresses under the indentor where the displacements are prescribed, precludes an exact solution, and requires iterative methods. Numerical methods for iterating a solution are well established and are used extensively for complicated mechanics problems. Breaking the problem into small components and using Finite Element Methods to solve it is one way of obtaining a solution in which convergence, and thus accuracy, can be checked.

2.1.4. Tactile Scanning

Previous studies on parameter estimation from Tactile Imaging were unable to accurately estimate lesion modulus. These earlier studies developed inversion schemes based on tactile maps, which spatially averages the tactile data to create a single image of the relative pressures collected as discussed in §1.1. This spatial averaging results in a loss of the detailed information found in separate pressure frames. In order to avoid the loss of information inherent in tactile mapping, we propose to develop an inversion algorithm based on a new tactile imaging modality called tactile scanning.

The salient difference between tactile scanning and tactile mapping is that in tactile scanning all of the relevant information in the centerline of the pressure frames is used. The centerline is easily identified as the row or column with the greatest difference between its minimum and maximum values. In tactile scanning, each centerline pressure profile is merely concatenated to the previous pressure frames. The pressure profiles collected overlap spatially.

The data from tactile scanning is best visualized as a Composite Tactile Image (CTI). An example CTI for a single lump model is shown in figure 2.6. The frames for this CTI were generated using finite element analysis, as will be detailed in the following section. This two-dimensional CTI is formed from the one-dimensional centerline pressure frames, collected every 2.5 mm for 80 mm centered at the lump. The pressure frames are

stacked vertically, and the strong diagonal line of increased pressure attests to the symmetry of the imaged model.

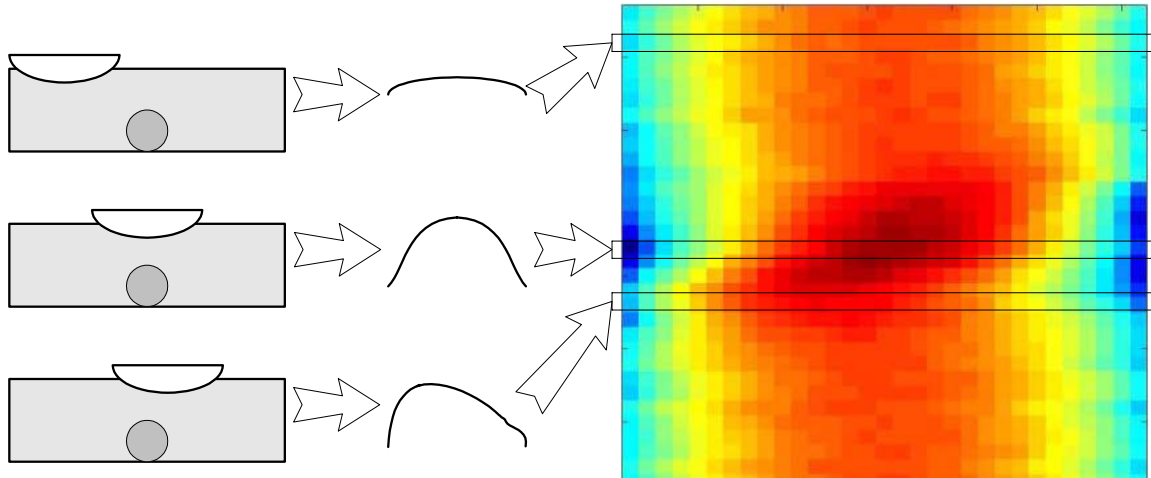


Figure 2.6. Compiling the information from Tactile Scanning into a Composite Tactile Image (CTI). The CTI is visualized as a two-dimensional image, where each row is a distinct pressure frame centerline. The CTI shown illustrates the compilation of the CTI. The pressure data was calculated from a finite element model, with a round lesion of diameter 20 mm embedded in tissue 40 mm deep. The lesion is 10 times as stiff as the background. The pressure frames are collected every 2.5 mm and stacked to form the CTI. Since the lesion and tissue are symmetric in the direction of the scan, when the frames are stacked the CTI is symmetric (in the matrix sense: $a_{ij} = a_{ji}$).

It is important to note that in tactile imaging, the ends of the pressure frames will most likely not decrease to zero. Since the pressure sensors do not cover the entire surface of the imager, the furthest extent of the imager that makes contact with the tissue is not covered with pressure sensors. This has the effect of cropping the pressure frames laterally to the width of the pressure sensor.

2.1.5. Parameter Ranges

The ranges of interest for breast and lesion size and modulus are shown in Table 2.1. The modulus of the background varies from the softest fat to the stiffest glandular tissue, while the lesion modulus varies from glandular tissue to cancer [Krouskop 99]. The thickness range of the breast tissue covers the range expected for the upper outer quadrant of the breast when the woman is laying supine [Gray 01]. This position is the standard position for obtaining tactile images, and the upper outer quadrant of the breast is the most common site of breast cancer, with more than half of all cancers occurring in this quadrant [Komen 03]. The minimum lesion diameter used in this study, 5 mm, corresponds to the minimum lesion diameter that is found by mammography [Lester 99], which is the current gold standard for detecting breast pathology. The maximum lesion diameter is 20 mm, which is the lower limit of invasiveness.

Table 2.1. Range of parameters for breast and lesion modulus and size

Parameter	Background Modulus B	Lesion Modulus L	Tissue Thickness t	Lesion Diameter d
Minimum	7.5 kPa	45 kPa	20 mm	5 mm
Maximum	50 kPa	750 kPa	40 mm	20 mm

2.2. Mechanical Modeling

Wellman [99] showed that finite element analysis can accurately model tactile imaging, and so we have constructed finite element models of the problem in order to obtain surface pressure profiles to study for parameter estimation.

2.2.1. Finite Element Model Construction

A typical finite element model as used in this study is shown in figure 2.7. The finite elements in the regions far from the surface and the lesion are set to a size where the results do not differ by more than 3% from the solution with a much finer mesh. In order to model the lesion as circular in cross section, we require a finer mesh in its vicinity. A finer mesh is also used at the surface, so that the indentation is smooth, and the resultant surface pressure information is spatially resolved. In these regions, a finer mesh will also allow for a more detailed representation of the large spatial variations we expect in the stress field.

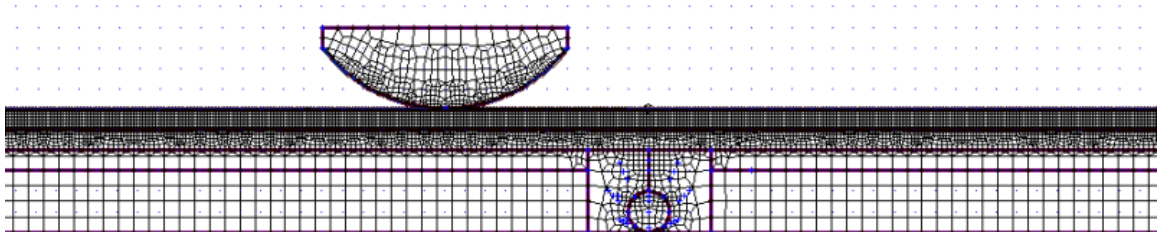


Figure 2.7. Sample finite element model used in this study. This model has 30 mm tissue thickness with an embedded lesion of 10 mm diameter. The tactile scanhead is modeled as a partial cylinder with infinite modulus.

The model is constructed with a plane strain assumption, so that the slice shown in figure 2.7 represents a long indentor above an infinitely long slab of tissue in which is embedded a cylindrical lesion. The models were created in Femap v8.0 (EDS Inc., Plano, TX) and solved using Abaqus Standard 5.8.1 (HKS Inc., Pawtucket, RI) with nonlinear geometry formulation. The Poisson's ratio for each of the materials was set at 0.499, since the glandular and fatty tissues in the breast are mostly water and can be considered incompressible [Fung 93].

The background tissue and the lesion are assumed to be composed of isotropic, linearly elastic tissue. These assumptions are valid within the ranges discussed in §2.1.5. In keeping the assumptions valid, the models in this study were kept to 6% strain for fat, and 4% strain for the softest lesions studied, less for stiffer lesions.

To simulate tactile imaging, the scanhead is indented into the tissue 4 cm to the left of the inclusion by a set vertical force. While maintaining this force, the scanhead is then moved laterally by 8 cm. The increments of the finite element analysis are small, generating one pressure frame for approximately each 0.5 mm of travel. The pressure frame closest to each 2.5 mm increment is recorded in the CTI. This spacing is the most analogous to that of frames collected using the laboratory tactile imager described in §1.4.1., with a data recording rate of 10 Hz and a travel speed of approximately 2.5 cm/s.

2.2.2. Tactile Information from Finite Element Models

Figure 2.8 shows a sampling of the pressure frames obtained from Finite Element Analysis. Pressure frames were obtained every 2.5 mm for 40 mm to either side of the lesion. The pressure frames were cropped to 32 mm in width, corresponding to the width of the pressure sensor area on the laboratory sensor. In order to use all of the tactile information of each frame, we reassemble the frames into a CTI [figure 2.9] as described in §2.1.4. The CTIs vary from having uniform rows (in the absence of a lesion) to exhibiting a very distinct diagonal bar of high pressure in the middle. As the indentor approaches from the left of the lesion, the pressure profile peak will shift to the right, and vice versa.

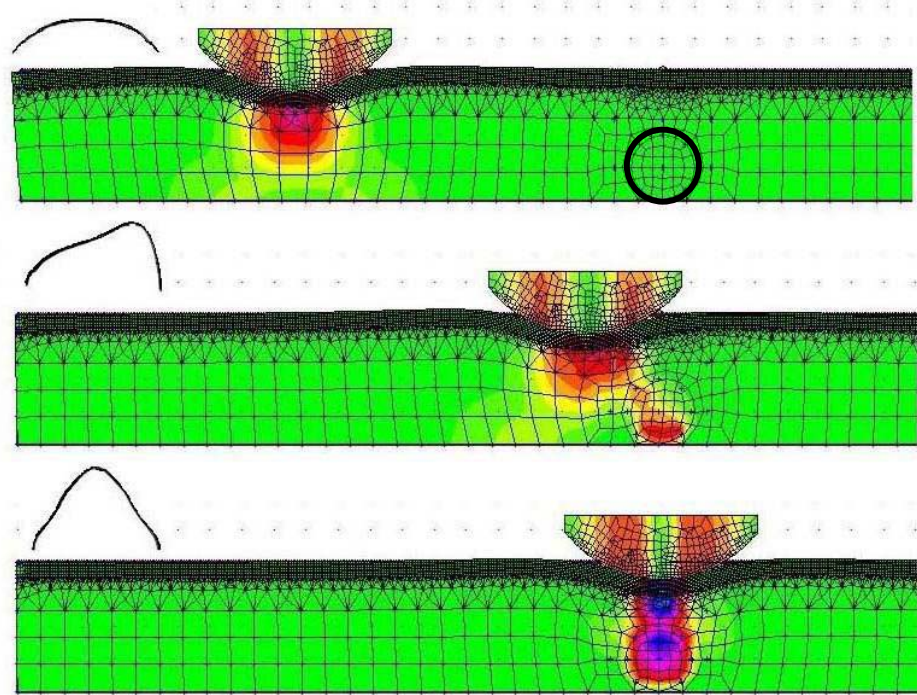


Figure 2.8. Sample finite element model results. The indentor is pressed into the tissue far from the lesion, then scanned across the top of the tissue at the same vertical force. This model has tissue thickness $t = 20$ mm, lesion diameter $d = 10$ mm, background modulus $B = 15$ kPa, and lesion modulus $L = 150$ kPa. The lesion is outlined in the top image for clarity. The force applied is 8.0 N/mm. The pressure profile at the interface of the indentor and the tissue for each frame is shown at left.

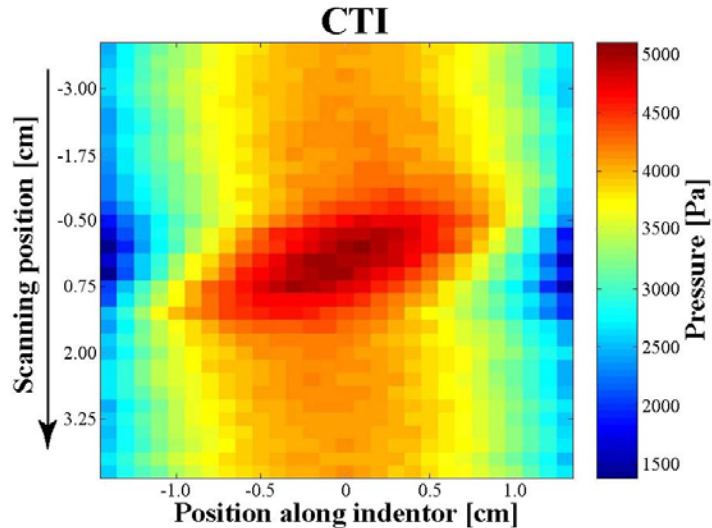


Figure 2.9. Composite Tactile Image from finite element model data. Each row approximates the pressure profile along the centerline of the indentor from a plane strain model. This CTI is a collection of the 33 pressure frames obtained every 2.5 mm over an 80 mm range with the lesion in the center. The CTI data is from a model with parameters $t = 25$ mm, and $d/t = 0.6$, $L/B = 50$.

Typical single-lesion CTIs are shown in figure 2.10. From these images we note that the geometry (d, t) affects the how far the peak of the CTI rises from the background more so than the modulus ratio L/B . The gross appearance of the CTI shows little variation for a constant geometry with a modulus ratio greater than $L/B = 3$.

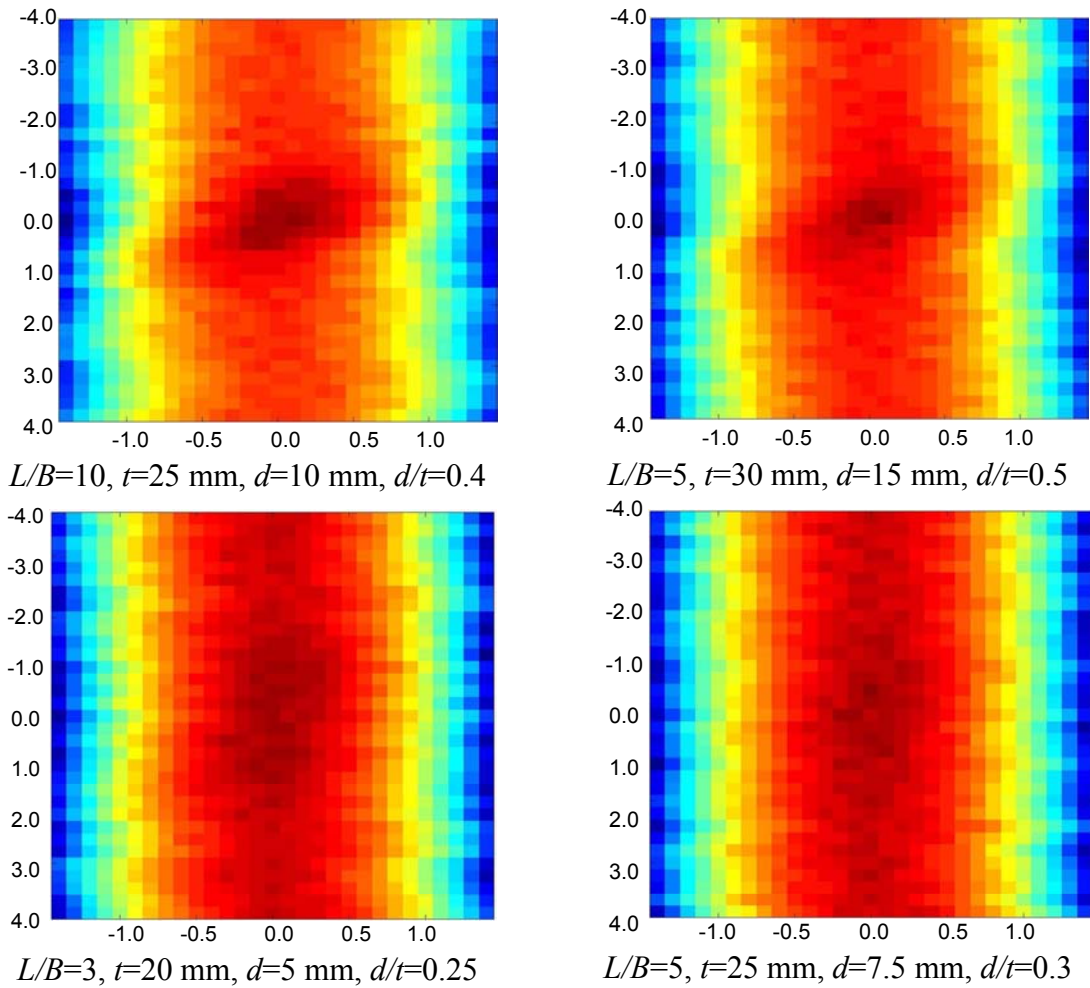


Figure 2.10. CTIs for various models. The frames of these CTIs were obtained at the same force (80 N/mm), and each CTI color scheme normalized to the highest value in the image.

2.3. Inversion Algorithm

2.3.1. Algorithm Development

By lining up the individual pressure frames without performing spatial averaging (as in tactile mapping) we keep all available tactile information. We can vectorize the CTI into a pressure vector P with all the rows of the CTI appended end to end, and similarly construct a column vector G of the parameters of interest. The problem then becomes to find the transformation matrix A that minimizes the error ε in

$$G = AP + \varepsilon$$

$$\text{for } G = \begin{bmatrix} B \\ L \\ t \\ d \end{bmatrix} \text{ and } P = [\text{CTI}]_v$$

where the notation $[\text{CTI}]_v$ implies appending the rows of the CTI together into a row vector.

The above describes a linear system, with the transformation matrix A responsible for a linear transformation between the pressure data P and the parameters in G . The relationship between the pressure in P and the parameters $[B, L, t, d]$, however, is not linear. Figure 2.11, for example, shows the relationship between the peak pressures collected over the lesion to the lesion modulus and diameter and those collected far from the lesion to the tissue thickness. These relationships are highly nonlinear. The same is true of other principal characteristics of the pressure data.

To improve the accuracy of a linear model, we look for parameters in G from which the parameters [B , L , t , d] can be calculated, but which are more linearly related to the tactile information. We therefore consider the following input parameter vector

$$G = \begin{bmatrix} f_1(B) \\ f_2(L) \\ f_3(t) \\ f_4(d) \end{bmatrix}.$$

In order to establish the appropriate functions f_i , we look to mechanics to understand the relationship between the parameters and the pressure frames.

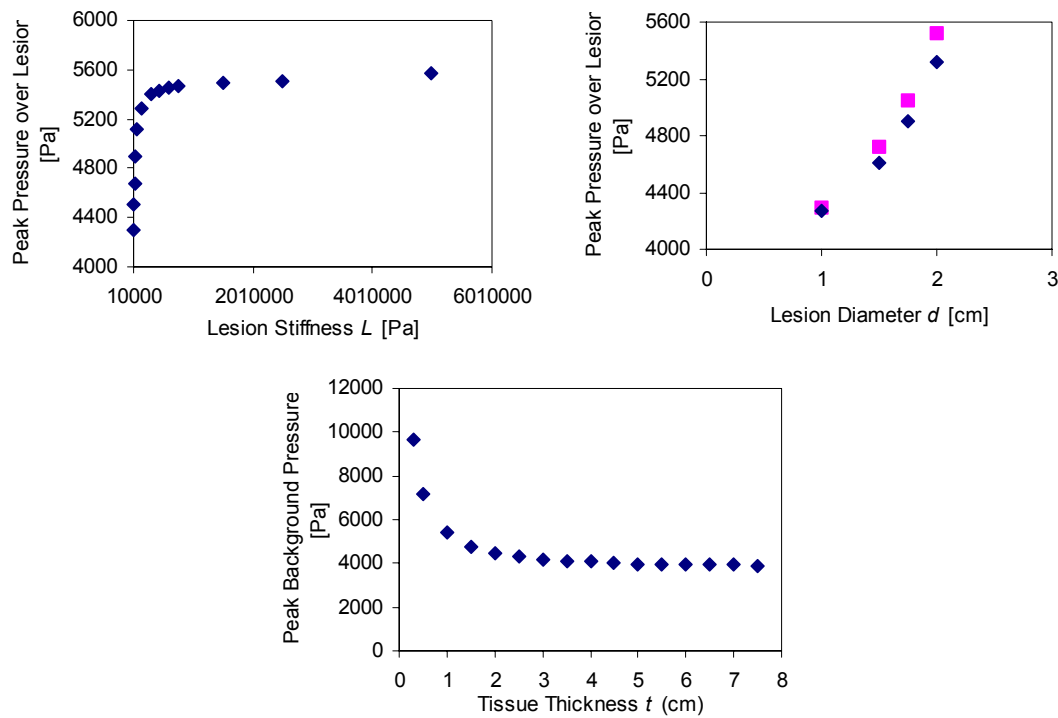


Figure 2.11. Model parameters versus resultant pressure information. The data was obtained on models in which only the parameter of interest was varied. For L : $B = 15$ kPa, $t = 30$ mm, $d = 15$ mm. For d : $B = 15$ kPa, $t = 30$ mm, $L = \{75\text{ kPa}, 150\text{ kPa}\}$. For t : $B = 15$ kPa, $d = 0$.

Far away from the lesion, the parameters that affect the surface pressure are the background modulus B and thickness t . As an approximation, suppose that the total scanhead force F can be described by $F = P A_{\text{sensor}}$ where A_{sensor} is the area of the entire scanhead, and P is the representative pressure recorded. Approximating the tissue directly under the scanhead as a linear spring, as shown in figure 2.12, then

$$F = \frac{BA_{\text{sensor}}}{t} \Delta t$$

where Δt is the indentation distance into the tissue. Then

$$P = \frac{B}{t} \Delta t .$$

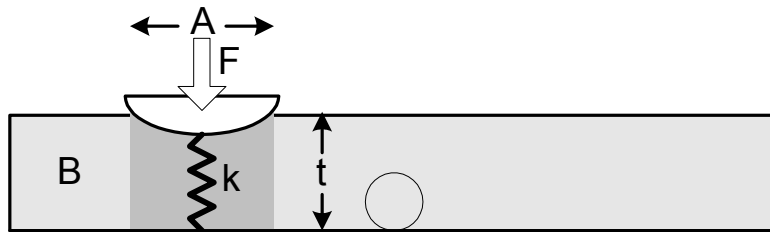


Figure 2.12. Approximating the tissue under the sensor as a spring.

The indentation distance is dependent on the force applied, which is constant across all models. Therefore we see that the pressure information P is related directly to the background modulus B and inversely to the tissue thickness t . Plots of the maximum background pressure versus the linearized parameters B and $1/t$ bear out the linear relationship between these parameters and the peak pressure obtained in the absence of a lesion [figures 2.13 & 2.14].

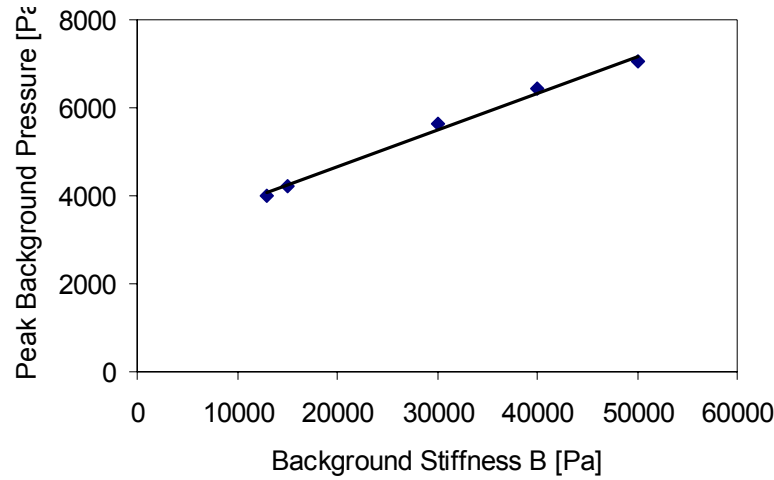


Figure 2.13. Maximum background pressure versus background modulus for finite element models with tissue thickness $t = 40$ mm. The line shows a linear regression ($R^2 = 0.99$).

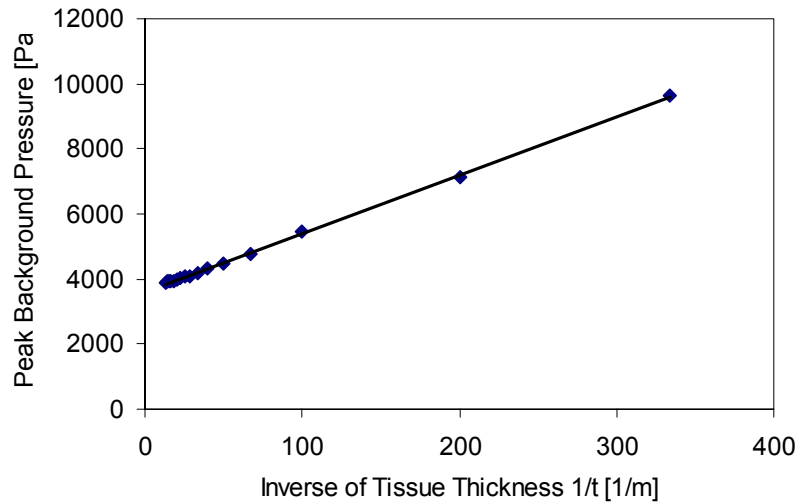


Figure 2.14. Maximum background pressure versus linearized tissue thickness for finite element models with tissue modulus $B = 15$ kPa, and no lesion. The line shows a linear regression ($R^2 = 1.00$).

As an alternate model, the Hertz theory for cylindrical indentation suggests a square root relationship between the peak background pressure and the background modulus [Johnson 85]. A function $P_{background} = f(B^{1/2})$ fits the data in figure 2.13 slightly better

then the linear relationship shown, with $R^2 = 1.00$. With the limited range for the background modulus, however, and the strong linear relationship between the background pressure and modulus, a fit to $B^{1/2}$ will likely show at most only a small improvement over using the modulus B directly. We therefore choose to use the simpler linear model.

Over the lesion, the situation is more complicated. If we consider the lesion and the background tissue above it to be represented by a linear spring each, then the tissue through the lesion can be modeled as two springs in series. The spring constant for the spring through the lesion is L/d while that through the tissue is $B/(t-d)$ [figure 2.15]. The total spring constant k seen by the tactile imager directly over the lesion becomes

$$k = \left(\frac{t-d}{B} + \frac{d}{L} \right)^{-1} = \frac{LB}{L(t-d) + Bd}.$$

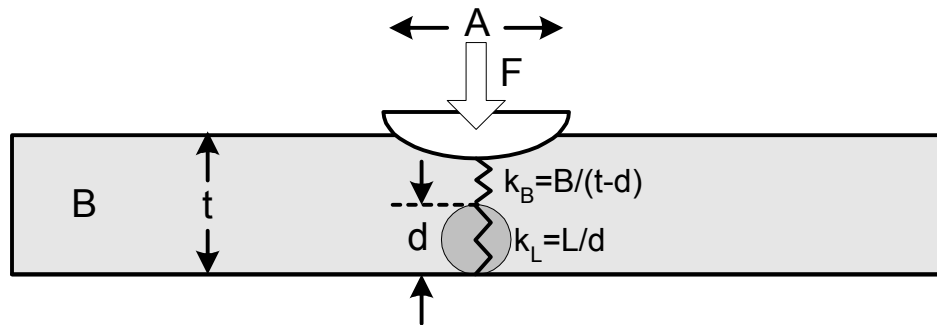


Figure 2.15. Representation of the tissue through the lesion as two springs in series.

In our parameter ranges of interest, $2B \leq L \leq 100B$ [Wellman 99], so in general $L \gg B$.

With this assumption, the above relationship collapses to $k = \frac{B}{(t-d)}$. This is analogous

to the situation far from the lesion, if we take the linearized thickness of interest to be $1/d'$, where $d' = t - d$. Therefore the parameter $f_4(d) = \frac{1}{t-d}$. This is a positive single

valued function in d , and increases as d increases. Plots of the peak CTI pressure versus various single-valued combinations of d and t show that the peak pressure is well related to various $f(d)$, with a slight improvement in the correlation for the function $f(d) = \frac{1}{t-d}$

[figure 2.16].

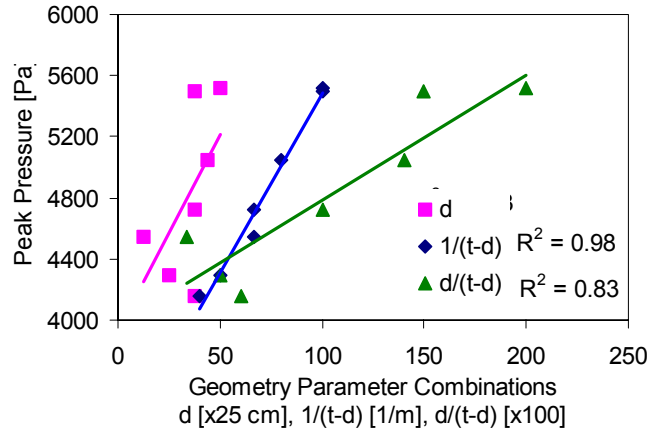


Figure 2.16. Maximum pressure over lesion versus lesion diameter d and two linearized diameters. The data was calculated from finite element models of tissue thickness t between 20 and 40 mm and background stiffness $B = 15$ kPa.

Since the lesion is buried under soft tissue we do not expect a direct relationship between the lesion modulus L and the resulting tactile information. As the preceding linearization for the lesion diameter suggests, the much lower modulus of the background tissue results in a weak dependence of the surface pressure on the lesion modulus. This accords with previous work that found estimating the lesion modulus from tactile information problematic [Wellman 99, Weber 00].

We consider the average modulus through the tissue at the center of the lesion. In practice, we find that using the depth-averaged modulus $S = L \frac{d}{t} + B \frac{t-d}{t}$ yields exponential errors in the estimation of the average modulus and thus the lesion modulus. This points us [Hyvarinen 01] to the use of the natural logarithm of the depth-averaged modulus as the true linearized parameter. A plot of $\ln(S)$ versus the maximum CTI pressure P_{max} shows that indeed the pressure tends to increase more linearly with the natural logarithm of the depth-averaged stiffness [figure 2.17] than with the modulus directly [figure 2.11]. Although this relationship is not as strong as that for the other linearized parameters, it is more linear than that found for other attempts at parameter linearization for the lesion modulus such as L/B and $L^{1/2}$ or $S^{1/2}$.

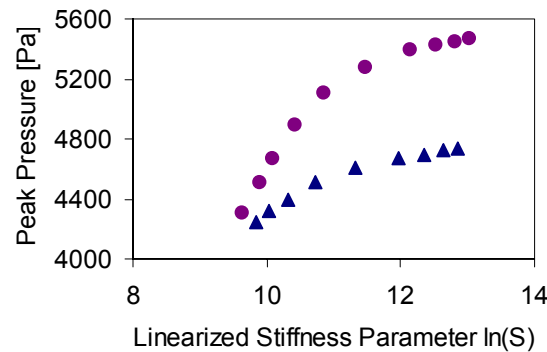


Figure 2.17. Peak pressure versus linearized stiffness parameter (natural logarithm of depth-averaged modulus through the lesion) shown for two sets of finite element models. The upper data set is for models with $B = 15$ kPa, $t = 25$ mm, $d = 15$ mm. The lower data set is for models with $B = 15$ kPa, $t = 30$ mm, $d = 15$ mm. A linear fit through the data sets has an R^2 value of 0.90 for the upper data set and 0.94 for the lower data set.

The linearized parameters used in G thus become

$$G = \begin{bmatrix} B \\ \ln(S) \\ 1/t \\ 1/(t-d) \end{bmatrix}$$

where

B = elastic modulus of background tissue (refer to figure 2.3),

$$S = \text{weighted modulus at lesion center} = \frac{Ld + B(t-d)}{t}$$

and L is the lesion modulus,

t = tissue thickness, and

d = lesion diameter.

2.3.2. Calculating the Transformation Matrix

Applying the above algorithm to tactile scanning data requires determining the transformation matrix A that maps the tactile information in P to the tissue parameters in G . For any tactile imager (modeled or physical) sets of the linearized parameters and the resultant pressure profiles, $\{P, G\}$, are collected for each of M tissue samples that span the range of parameters of interest. These data sets are appended into matrices P_M and G_M and used to find $A = G_M P_M'$, where P_M' is the pseudoinverse of P_M ,

$$P_M' = (P_M^T P_M)^{-1} P_M^T.$$

The transformation matrix A is then found by

$$A = G_M P_M' = \begin{bmatrix} B_1 & B_2 & \dots & B_m \\ \ln(S_1) & \ln(S_2) & \dots & \ln(S_m) \\ 1/t_1 & 1/t_2 & \dots & 1/t_m \\ 1/(t_1-d_1) & 1/(t_2-d_2) & \dots & 1/(t_m-d_m) \end{bmatrix} \begin{bmatrix} P_1 \\ P_2 \\ \vdots \\ P_m \end{bmatrix}^{-1} \begin{bmatrix} P_1^T & P_2^T & \dots & P_m^T \end{bmatrix}$$

We can test how well the transformation matrix maps the system by using this \mathbf{A} to estimate the parameters in a new column vector G_n , whose associated pressure information P_n (a row vector) was not used to calculate \mathbf{A} . The estimated parameter vector \hat{G}_n is

$$\hat{G}_n = \mathbf{A}P_n.$$

Due to nonlinearities in the actual system and other factors such as noise in the pressure data, the error $\varepsilon = \hat{G}_n - G_n$ will not be zero. Obtaining the pseudoinverse of P performs a least-squares fit. Thus the resulting \mathbf{A} is a least-squares fit to the set of transformation matrices that fit each of the data sets perfectly. The above needs only be done once in order to establish the correct transformation matrix for the system at hand.

2.4. The Transformation Matrix

2.4.1. Rank Deficiency

The four rows of \mathbf{A} are independent to the extent that the four underlying parameters are independent. However, for each parameter, the transformation matrix is required to map a long vector of pressure data to a singular parameter. For c frames in one CTI with s pressure points per frame, the pressure vector for each parameter is cs elements long. In the system considered here, we collect four frames per centimeter between -40 mm and 40 mm, resulting in 33 frames of tactile information. With 16 sensors per frame, the

transformation matrix must then map $33 \times 16 = 528$ data points to a single scalar parameter.

We can calculate the transformation matrix using data collected on lesions at the limits and midpoints of each parameter range. With four independent parameters, that results in 81 data sets to use in P_M , which results in a maximum rank of 81. In performing the inversion of P_M , we attempt to find the 528 elements of \mathbf{A}_i from a system with a maximum rank of 81. This is a vastly underconstrained system, and as such we have no guarantee that the \mathbf{A} matrix that we find is an adequate representation of the linear transformations required to calculate the correct G_n from every P_n allowed in our parameter range.

The columns of P , however, are not wholly independent. Besides the symmetry inherent in the underlying data, each pressure value is not entirely independent of its neighbour. In the absence of noise, in fact, the pressure profiles will be smooth and it would be possible to approximate any one pressure quantity from a simple relationship to its neighbours. This strong relationship between the columns of P can simplify the transformation required of the \mathbf{A} matrix so that there may be enough information to construct an adequate \mathbf{A} matrix.

A singular value decomposition of P_M can provide insight into the information content of the transformation matrix. Figure 2.18 shows the largest singular values for a P_M matrix that was composed of 81 data sets calculated from finite element models spanning the

parameter ranges of tactile 2.1. The first singular value corresponds to the average of the P_M matrix, and as expected is much higher than the rest of the singular values. Besides this first singular value, the next two are an order of magnitude larger than the rest. This indicates that most of the information in the pressure matrix is contained in only a few components. There are only three dominant singular values, however, indicating that the information in the pressure data is contained to a large degree in a three-dimensional space. Since we are trying to estimate four parameters, this three-dimensional space may be too confined for accurate estimation of one of the four parameters.

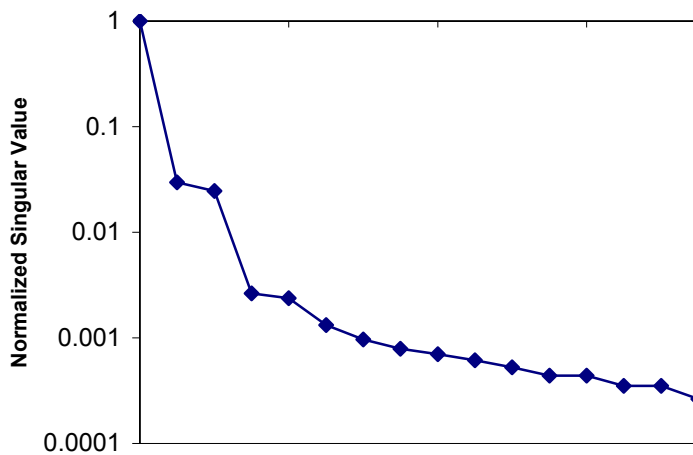


Figure 2.18. First 16 singular values for tactile information matrix P_M . The P_M matrix was created from 81 finite element models which had parameters at the edge and middle of the ranges of interest. The first singular value is clearly dominant, and is due to the high nonzero average of the pressure profiles.

In the rest of this section we will obtain a transformation matrix by three methods. First we will calculate a *numerical* transformation matrix, using the algorithm in § 2.3.2 on finite element model data. Next, we will analyze the singular values contained in the transformation matrix A_i for each linearized parameter and reconstruct an *analytical*

transformation matrix from the dominant singular values. With the knowledge gathered from generating these transformation matrices and mechanical reasoning we will generate a *synthetic* transformation matrix that models the major trends in the data. We will test each of these transformation matrices on the finite element model data sets in order to gain insight into the important features of the mapping inherent in using a transformation matrix.

2.4.2. Visualizing the Transformation Matrix

By performing a least-squares fit to the data, the transformation matrix A automatically picks out the important features of the CTI for inversion of each individual parameter. Each row A_i of A corresponds to one parameter G_i in G , and as such is independent of the other rows, save any dependence potentially present between the G_i . For each linearized parameter, we have

$$G_i = A_i P. \quad 2.1$$

For any linearized parameter i , we can wrap A_i to a matrix of the same dimensions as the CTI, \tilde{A}_i , in order to visualize which aspects of the CTI are important for the parameter G_i .

2.4.3. Numerical Transformation Matrix

The wrapped transformation matrices \tilde{A}_i for each parameter G_i found using the tactile information from the finite element models are shown in figure 2.19. The finite element

models spanned the ranges of interest of the parameters indicated in table 2.1. The 81 models had parameters at the limits and midpoints of the respective range. A singular value decomposition (SVD) of the \tilde{A}_i indicates that, as expected from the SVD of P_M , there are only a few dominant singular values of the transformation matrix. The singular values of the \tilde{A}_i are shown in figure 2.20. For the background parameters B and t , there is clearly one dominant singular value, while for the lesion parameters S and d the second and possibly third values remain significant.

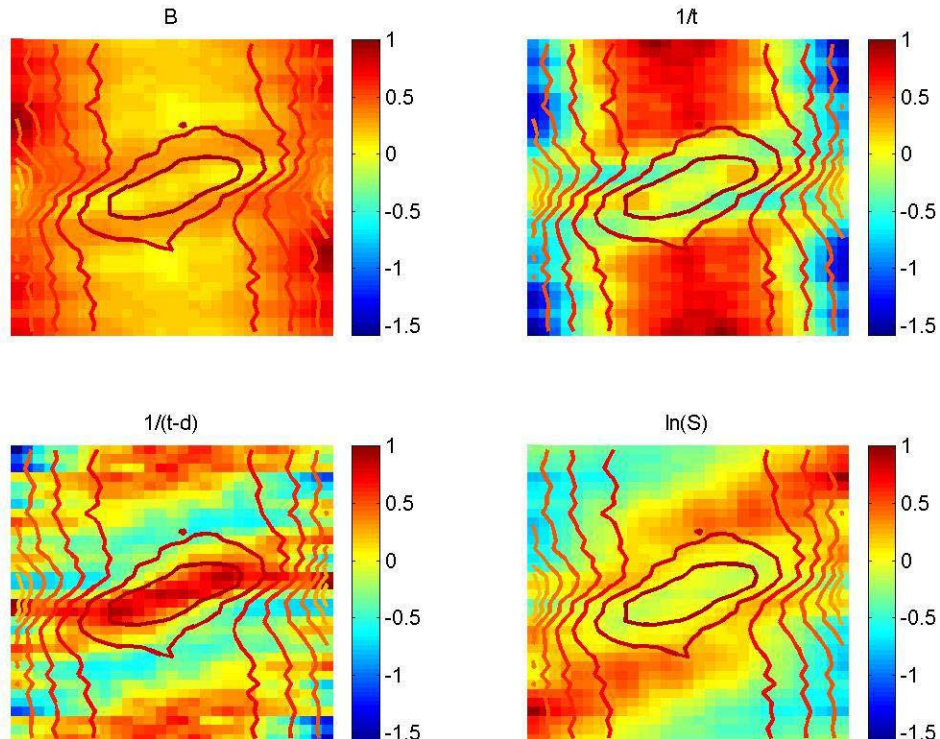


Figure 2.19. Wrapped transformation matrices \tilde{A}_i for each of the four parameters in G . The transformation matrices are shown wrapped to the same dimensions as the CTI, and a set of CTI contours ($B = 15$ kPa, $t = 25$ mm, $d = 10$ mm, $L = 150$ kPa) is indicated for reference. The matrices are normalized to their highest values.

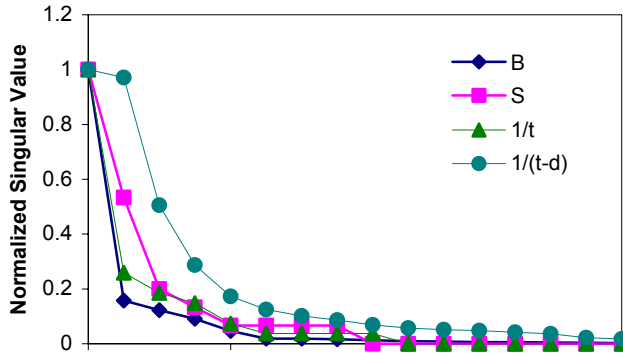


Figure 2.20. Singular value decomposition of the transformation matrices \tilde{A}_i for each linearized parameter in G . The first 16 singular values are shown. As expected, a few singular values dominate the decomposition of the matrices.

2.4.4. Reconstituted Transformation Matrix

In order to determine the importance of the dominant singular values of \tilde{A}_i in estimating the tissue parameters, we reconstitute the \tilde{A}_i using the first and second singular values. In other words, for $\tilde{A} = U S V^T$, the reconstruction using the first singular value is

$$\tilde{A}_{ij}^{SVD1} = U_{i1} S_{11} V_{j1}^T, \text{ and using both the first and second singular values, the reconstruction is}$$

$$\tilde{A}_{ij}^{SVD2} = U_{i,1:2} S_{1:2,1:2} V_{j,1:2}^T \text{ (commas added for clarity).}$$

Figure 2.21 shows the \tilde{A}_i matrices reconstituted from the first singular value and vector for each parameter, while figure 2.22 shows the matrices reconstructed using the first two singular values and vectors. The reconstituted matrices capture the gross features of the transformation matrices as seen in figure 2.19. The discrepancies are shown in figure 2.23. The errors for the background modulus are low, while those for the background thickness and lesion modulus are generally low, but with a few high outliers. The discrepancy between the reconstituted and numeric transformation matrices for the lesion diameter are much

higher on average, which is an indication that there are additional singular values that contain nonnegligible information about the transformation matrix for this parameter.

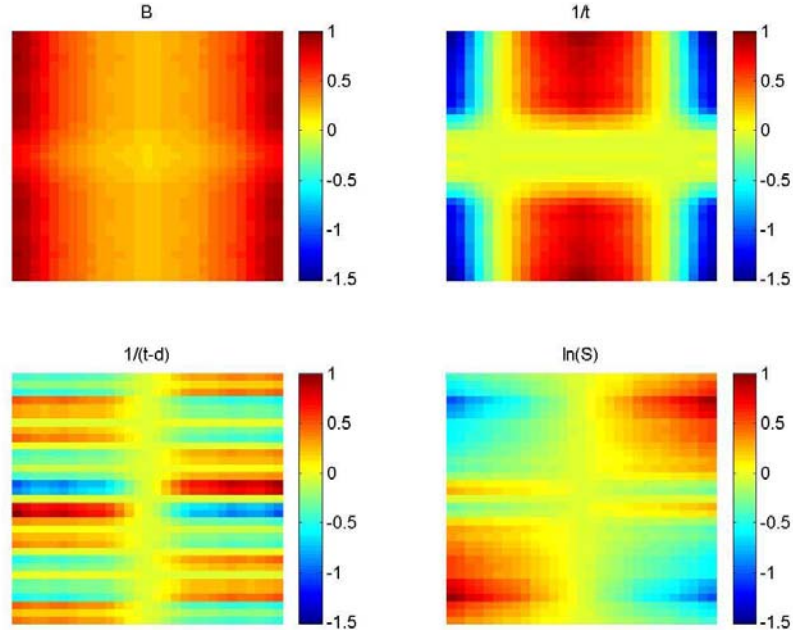


Figure 2.21. Wrapped transformation matrices \tilde{A}_i for each linearized parameter in G , reconstructed from the first singular value and its corresponding vector.

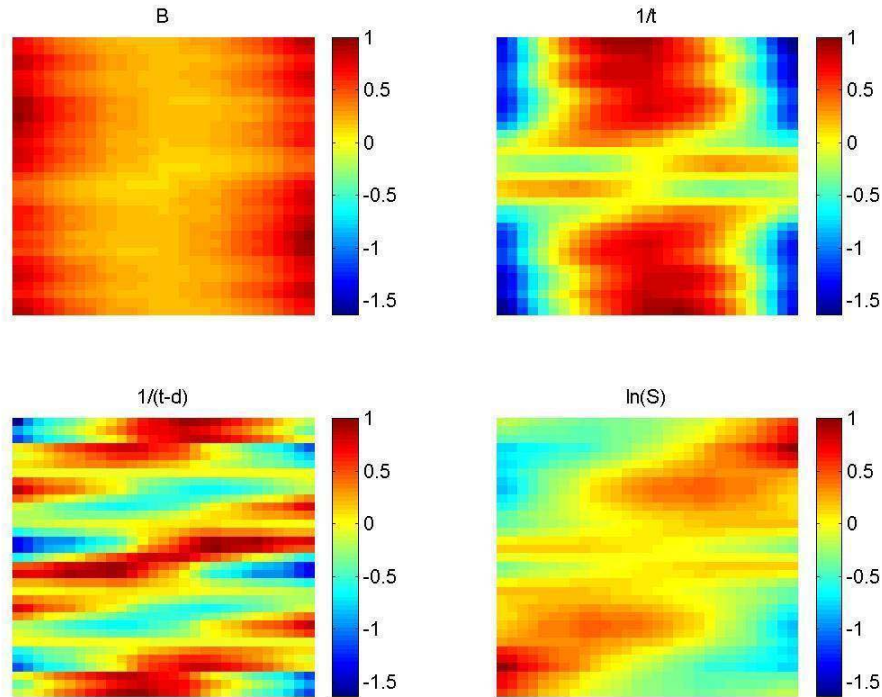


Figure 2.22. Wrapped transformation matrices \tilde{A}_i for each linearized parameter in G , reconstructed from the first two singular values and their corresponding vectors.

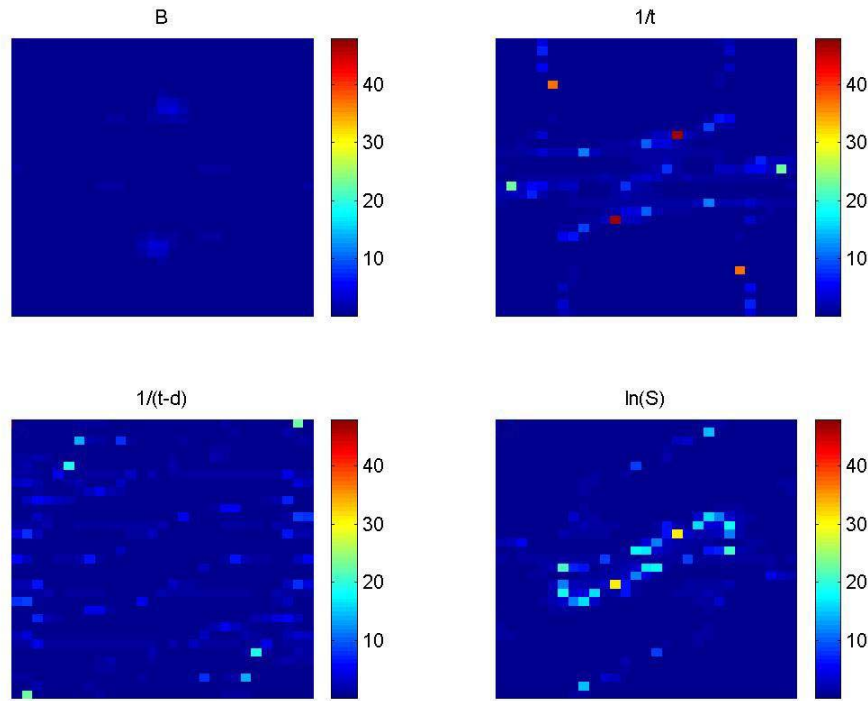


Figure 2.23. Discrepancy between the actual transformation matrices and the matrices reconstructed from the first two singular values. The error is shown as a multiple of the value of the transformation matrix.

2.4.5. Physical Basis of the Transformation Matrix

Figure 2.19 shows that the transformation matrix selects specific regions of the pressure data for determining the required parameters. With the transformation matrix in the form shown in figure 2.19, we can perform pointwise multiplication with the CTI in order to visualize which aspects of the CTI are important for the parameter G_i . This wrapping and multiplication yields the Accumulation Matrix \mathbf{G}^* , whose components G_{mn}^* yield the estimated parameter G_i from

$$G_i = \sum_m G_{mn}^* .$$

The accumulation matrices that result from multiplying the transformation matrices in figure 2.19 with a CTI constructed from a finite element model with parameters in the middle of the range of interest are shown in figure 2.24. The accumulation matrix differs only slightly from the transformation matrix, due to the peaks in the pressure data.

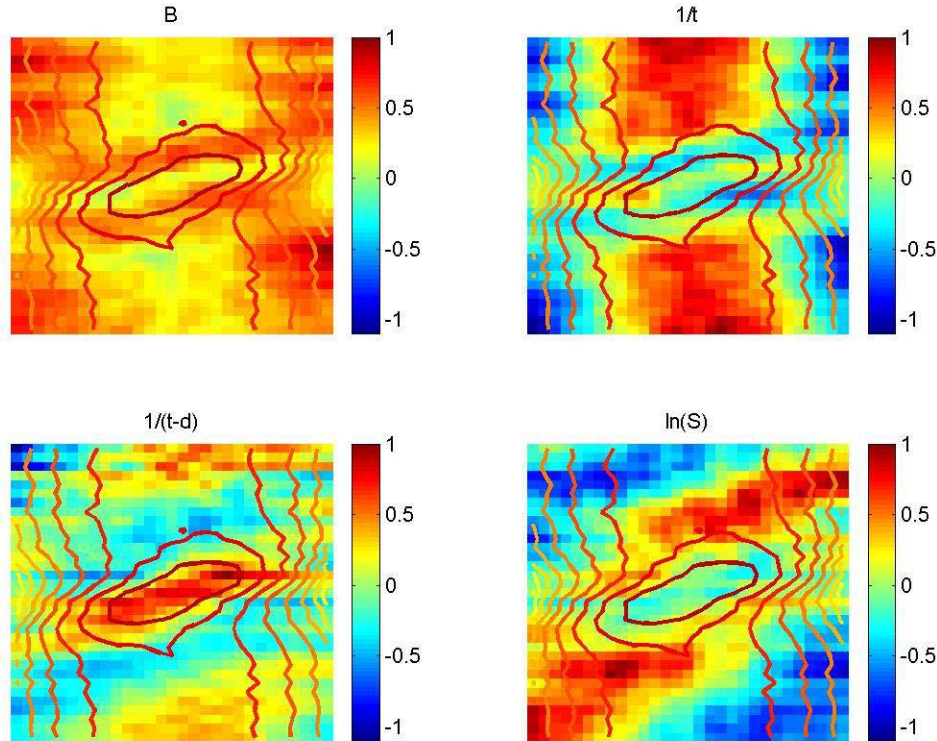


Figure 2.24. Accumulation matrices \mathbf{G}_i^* (normalized). Adding the value at all points will yield the estimated value of the parameter of interest.

As expected, the main regions of interest in calculating the background parameters B and $1/t$ are contained in the frames far from the lesion (at the top and bottom of the transformation and accumulation matrices). Tissue thickness requiring a positive contribution from the pressure peaks in this area and a negative contribution from the

edge. Conversely, the background stiffness requires only a positive contribution from the edge. Part of the reason for this can be seen from figure 2.25, which shows the pressure distribution through the tissue model for the first frame collected (the top row of the CTI). The pressure sensors in the middle of the indentor record a higher pressure stemming from the compression of the underlying tissue between the bottom of the indentor and the rigid substrate. This pressure is related to B/t as discussed in §2.3.1. The sensors at the edge of contact, however, record a pressure that stems from the much lower compression of the tissue located beneath and obliquely from them (i.e. away from the center of contact). This pressure is dependent on the local tissue properties, since the rigid substrate, located approximately t away, plays a minor role. Thus, the edge sensors record information related to B , and the transformation matrix at this edge region is important for the estimation of B . The information recorded at the center is related to both B and $1/t$. Thus, the transformation matrix for $1/t$ renders this region as positive, and subtracts the contribution of B from the calculation of $1/t$.

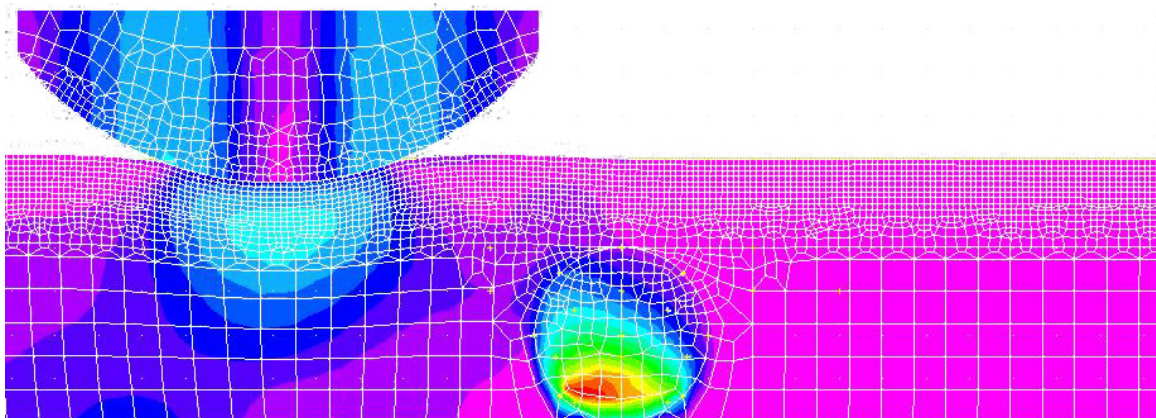


Figure 2.25. VonMises Stresses for furthest frame collection. The scanhead midpoint is 40 mm away from the lesion midpoint along the top of the tissue. The tissue is 30 mm thick and the lesion diameter is 20 mm. The background modulus is 15 kPa and the lesion modulus is 150 kPa.

The situation for the linearized lesion diameter $1/(t-d)$ is analogous to that for $1/t$ discussed above. As discussed in §2.3.1, the peak pressure directly over the lesion is related most strongly to the parameter $B/(t-d)$. Thus, this central region is required to be positive for the calculation of the parameter $1/(t-d)$. We also note involvement of the area corresponding to the positive contribution to $1/t$. This is due to the mathematical relationship between $1/t$ and $1/(t-d)$ for constant d . There is also a negative contribution from the area directly between this central background region and the region of pressure frames collected just off the lesion. Since a larger diameter lesion will extend further laterally as well as in height, it would result in a pressure signature in this region, resulting in a contribution to the pressure frames both in magnitude and in breadth. This area, just off the lesion, being negative in the transformation matrix implies that the combination of these two effects grows faster than linearly with the lesion diameter. Rendering this area as negative for the calculation of the lesion diameter prevents an overestimation of this parameter for larger lesions.

The region for the linearized stiffness parameter $\ln(S)$ is, as expected, the most complex. The accumulation matrix clearly highlights the peaks of the pressure profiles collected just off the lesion, and extends this area to the corners associated with the background modulus. The main area of interest is that of the peaks directly off the lesion, since this area is unique to the stiffness parameter. This indicates that a harder lesion, even if smaller, will affect the peaks of the pressure profiles collected off the lesion more strongly than a softer and larger lesion. This is seen qualitatively in the CTIs shown in figure 2.10. The lesion modulus clearly affects the width of the CTI peak more strongly

than it affects its magnitude, which is more strongly dependent on the lesion diameter, as expected from the above discussion. The area that is highlighted for the stiffness parameter extends from this area dependent on lesion stiffness to the area highlighted for the background modulus. This is expected since the stiffness parameter S is equally dependent on B and L .

2.4.6. Synthetic Transformation Matrix

The accumulation matrices shown in figure 2.24 are more complex than the simple reasoning of the previous section suggests. We can develop a transformation matrix based on the above reasoning, and test this synthetic transformation matrix on the same data used to calculate the numerical transformation matrix. Doing so we can quantify the validity of the insight gathered in the previous section.

The four parameters, B , t , L , and d , each require a unique transformation matrix based on the areas discussed in the previous section. These areas depend heavily on the boundaries between the edges and center of the sensor, and between the areas collected near the lump and far from the lump. The absolute values of the synthetic transformation matrices are set so that the average of the synthetic transformation matrices equal the average of the numerically generated matrices.

Edge versus center of sensor

Assuming a circular function for the pressure profile collected far from the lesion, $P(s) = P_o(w^2-s^2)$ where $w = 16$ mm is the half-width of the sensor and $0 \leq s \leq 16$ mm is the position from the center of the indentor, the pressure profile drops to half of its maximum value at $s = \pm 11$ mm. Therefore we assign the 5 mm bands on the edge of the pressure frames are considered to correspond to the ‘edges’ of the sensor and the central 22 mm to the center of the sensor.

Near lesion versus far from lesion

From the parameter ranges specified in §2.1.5, the maximum lesion size expected has a diameter of 20 mm. For frames collected every 2.5 mm over an 80 mm swath of tissue centered at the lump, the central 9 frames are acquired when the center of the sensor is over the lesion. Frames beyond these central 9 frames are thus considered far from the lesion.

Area for background modulus B

The area used to estimate the background modulus is the intersection of the edge area and the area far from the lesion. The area far from the lesion is shortened by one frame to ensure that the majority of the pressure sensors are off the lump for each frame. The resulting transformation matrix for the background modulus is shown in figure 2.26a.

Area for tissue thickness $1/t$

The positive area corresponding to the tissue thickness is the intersection of the central area and the area far from the lesion, with the latter once again foreshortened by one frame to ensure that the majority of the sensels are off the lump for each frame. This is flanked by negative areas corresponding to the edge of the sensor. The resulting transformation matrix is shown in figure 2.26b.

Area for lesion diameter $1/(t-d)$

This area stems from the pressure information collected over the lesion. Therefore, this area extends over the central frames (foreshortened one frame on each side so that we encompass the frames most likely to be collected over the lump). The width of this area is 17.5 mm, the width that encompasses 75% of the lesions encountered. The section of each pressure frame that is taken as positive is centered over the peak of the pressure profile (i.e. since adjacent frames are obtained 2.5 mm apart, the area of each frame taken as positive for this parameter slides over 2.5 mm for each frame away from the central one).

Similarly to the transformation matrix for the tissue thickness, we note the need for a small negative area. Since the linearized parameter depends on both t and d , this area cannot correspond to the area for tissue thickness. We thus choose a small strip to either side of the central frames as the offset for the lesion diameter. This corresponds to the

negative area in the numerical transformation matrix for this parameter. The resulting transformation matrix is shown in figure 2.26c.

Area for stiffness parameter $\ln(S)$

Given the discussion above regarding the width of the CTI, this area extends diagonally from the center in the frames off the lump towards to the edge of the sensor closest to the lesion when the sensor is far from said lesion. Figure 2.25 shows that even at the furthest extent of the pressure frame collection, the edge of the pressure profile is still weakly influenced by the lesion. Thus we allow this region to extend to the corner of the transformation matrix, corresponding to this edge of the pressure profiles. The width of this region is the same as for the lesion diameter.

The area thus described overlaps with half of the area of for the background modulus. The signal from the background modulus, however, can easily overpower the expected weak contribution of the lesion modulus. In order to minimize the influence of the background modulus, we set the area corresponding to the rest of the frames collected off the lesion as negative. The resulting transformation matrix is shown in figure 2.26d.

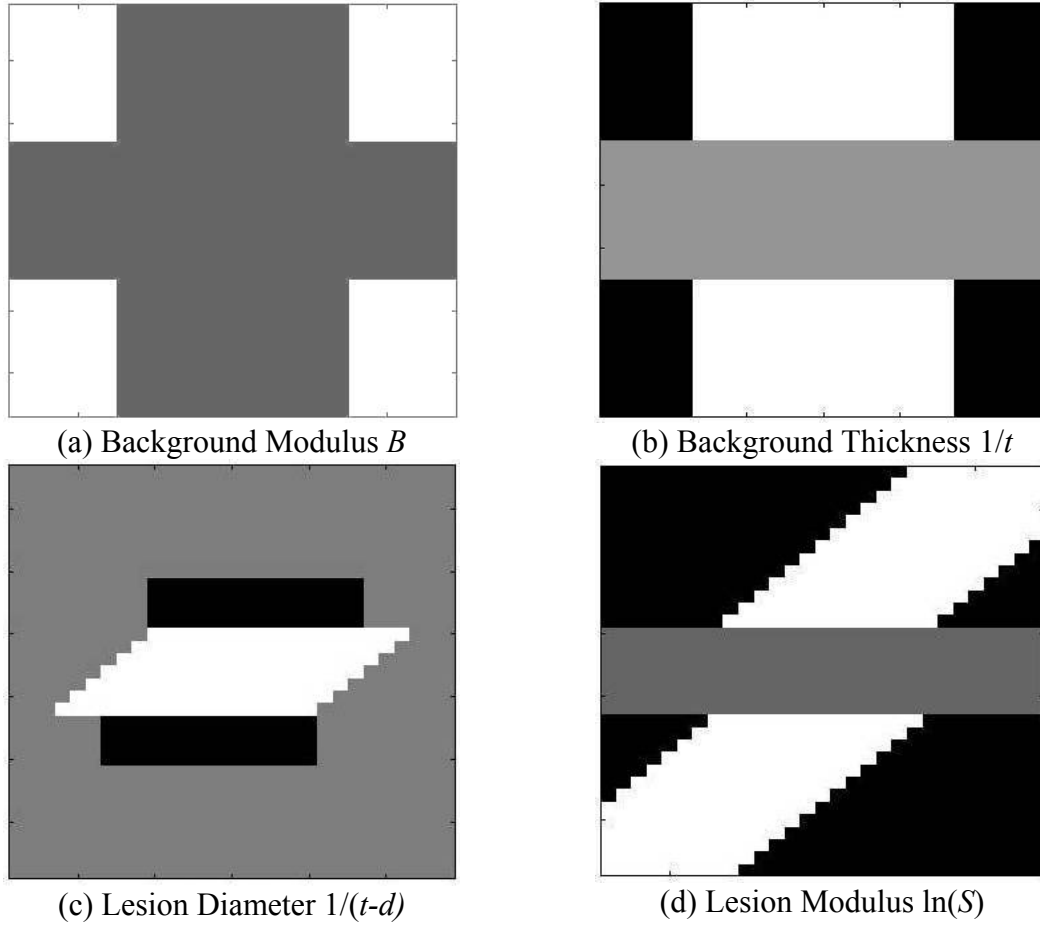


Figure 2.26. Synthetic transformation matrices based on analytical knowledge for parameters indicated. Positive value regions are indicated in white, negative values in black, and zero in gray.

2.5. Parameter Estimation Results

2.5.1. Results from the Numerical Transformation Matrix

The “all-but-one” algorithm outlined in §2.3.2 was followed to create a transformation matrix from the pressure data collected from finite element models. For each of 83

models, the other 82 models were used to compute the transformation matrix used to invert the data. In order to populate the parameter space, the 83 models included at least two models from each extreme of the parameter ranges of interest, with the rest evenly spaced through the parameter ranges [Appendix A.1]. The transformation matrices that result from this method are qualitatively identical to those shown in figure 2.19, differing only slightly ($< 5\%$) in absolute values.

Figure 2.27 shows the results of estimating the background modulus B . The mean absolute error of estimating B directly is 2.7%, and only 2.3% when using $B^{1/2}$ in G . Figure 2.28 shows the results of estimating the lesion modulus, tissue thickness, and lesion diameter over the entire parameter range. The mean absolute errors are less than 9% for the geometry parameters t and d , but is almost 100% for the lesion modulus L . This is not entirely surprising, given the fact that the singular values in P_M showed that the information in P_M is largely limited to three dimensions [figure 2.18].

Given the accuracy by which we can estimate the background modulus, we will assume that the background modulus can be found accurately *a priori* by collecting pressure frames off the lesion. This information can be used such that a tailored transformation can be applied to the rest of the data. This allows us to limit our algorithm to transformation matrices created from sets of data with the same background modulus. This reduces the parameter space required for calculating the transformation matrix and may lead to a better estimation by essentially limiting the required information to a subspace of P_M . For the rest of the discussion, we limit the background modulus B to 15

kPa to best model the average Young's Modulus of human breast fat. The new transformation matrix is created from all but one of the 32 model data sets with background modulus 15 kPa [Appendix A.2]. The results of estimating the three variable parameters are shown in Figure 2.29. The mean absolute errors decrease, with estimates of the geometry parameters incurring 1.9% mean absolute error (MAE) for the tissue thickness t , and 11.7% for the lesion diameter d . If we discount testing the algorithm on parameters at the extremes of the parameter ranges where the estimation is based on extrapolation, the mean absolute error for tissue thickness estimation drops to 1.5% and that for lesion diameter estimation to 6.9%. The mean absolute error for calculating the modulus parameter $\ln(S)$ is 3.3%, though this translates into a mean absolute error of 32.1% in estimating the lesion modulus L , given the errors in the other parameters included in S .

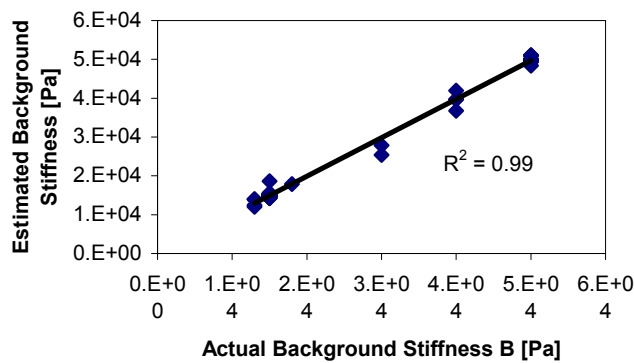


Figure 2.27. Estimating the background modulus B from surface pressure frames collected from finite element models. The mean absolute error is 2.7%.

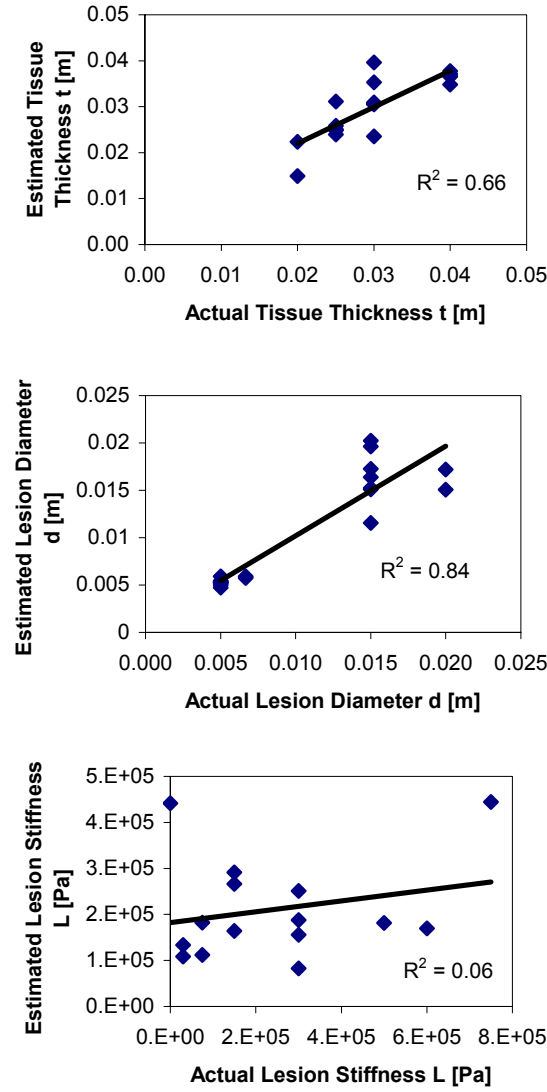


Figure 2.28. Estimating the parameters t (tissue thickness), d (lesion diameter) and $S = [Ld+B(t-d)]/t$ using a numerical transformation matrix created from 83 finite element models with parameters that span the range of interest. The regression coefficients for each estimation are indicated.

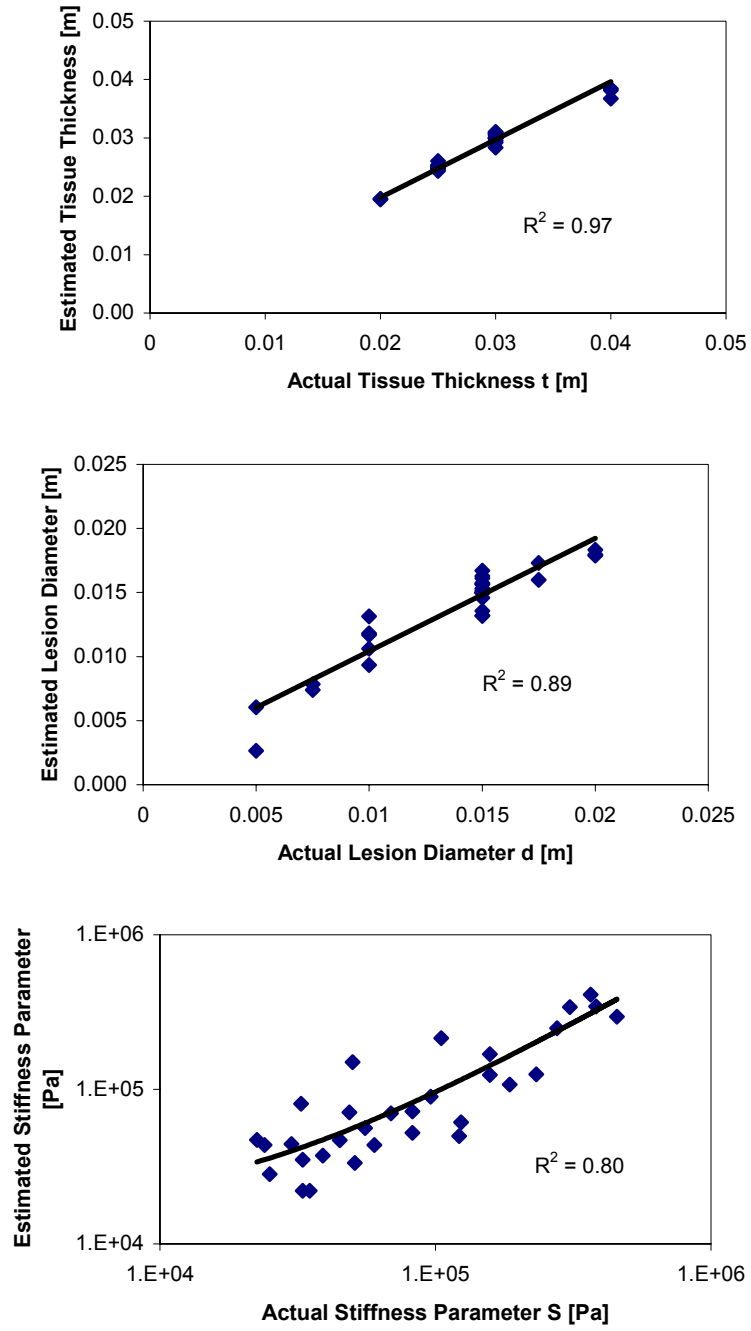


Figure 2.29. Estimating the parameters t (tissue thickness), d (lesion diameter) and $S = [Ld+B(t-d)]/t$ using a numerical transformation matrix created from 32 finite element models with a constant background modulus ($B = 15$ kPa). The regression coefficients for each estimation are indicated.

We may be able to estimate the lesion modulus more accurately by first estimating the geometry and then tailoring the accumulation matrix to the specific geometry and using it to estimate the lesion modulus. To test this, 9 models were created with the lesion modulus spanning the entire range of interest, and the other parameters constant ($B = 15$ kPa, $t = 30$ mm, and $d = 15$ mm). The all-but-one method was used to generate and test the transformation matrix. The further reduction of the parameter space inherent in this simplification improved the resulting estimation of the lesion modulus to a mean absolute error of 15.7% [figure 2.30]. This error drops to 13.2% if we discount the points estimated through extrapolation (i.e. the two points at the ends of the data range). The errors incurred are dependent on the underlying errors in the predictions of d and t . These errors are quantified for representative cases in figure 2.31. From this figure we see that the error of the estimated lesion modulus increases as the modulus ratio L/B grows. In practice, this is offset by the fact that as the lesion modulus increases, the estimation of the geometry parameters improves [figure 2.32].

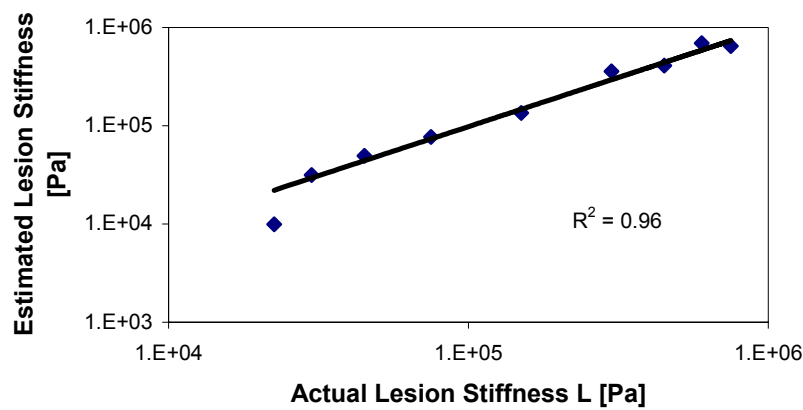


Figure 2.30. Estimated lesion modulus L from models with $B = 15$ kPa, $t = 30$ mm, and $d = 15$ mm.

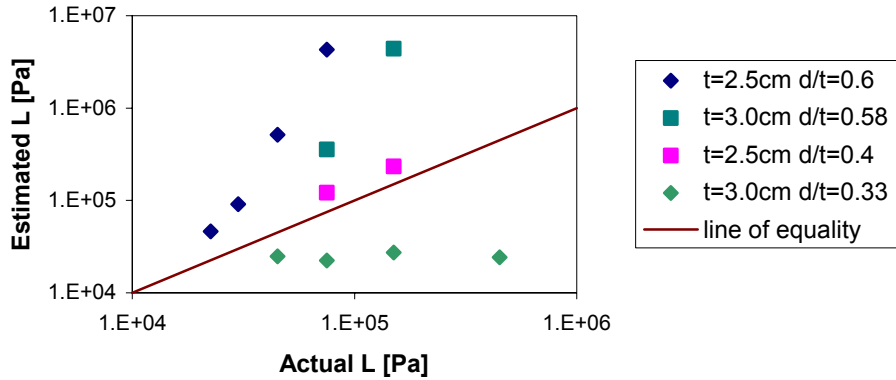


Figure 2.31. Error in estimated lesion modulus based on erroneous d/t estimation. The transformation used was formed from models with $t = 30$ mm and $d/t = 0.5$. The models tested are shown in the legend. The error increases for greater lesion modulus and is larger for a greater error in predicted t and d/t . If the actual d/t was higher than predicted, then predictions of the lesion modulus L using that transformation matrix will be too high, and vice versa.

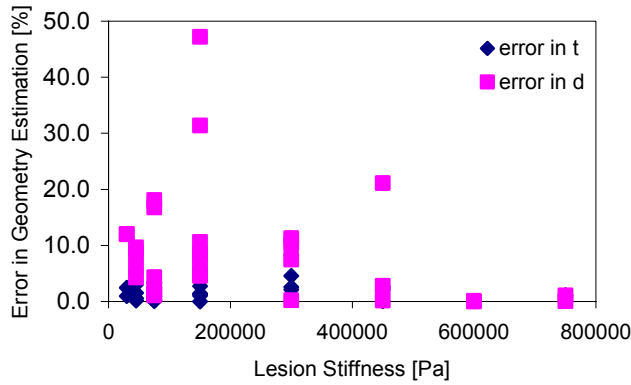


Figure 2.32. Error in estimating geometry parameters versus lesion modulus for the cases in figure 2.29. The errors tend to decrease as the lesion modulus grows.

2.5.2. Results from the Reconstituted Transformation Matrix

The inversion algorithm was applied to the 32 models with constant background modulus once more, using the transformation matrix reconstituted from the first two singular values of each transformation matrix A_i . The results in this case are summarized in table 2.2 and shown in figure 2.34.

Table 2.2. Mean Absolute Errors in estimating the linearized parameters using the numerically generated transformation matrix and the reconstituted transformation matrix.

Linearized Parameter	MAE using numerical A from §2.3.4	MAE using reconstituted A from figure 2.22
B	0.16%	0.31%
$\ln(S)$	3.3%	3.2%
I/t	2.0%	1.1%
$I/(t-d)$	6.3%	2.3%
L	32 %	58 %
t	1.9 %	1.9 %
d	11.7 %	6.3 %

In general, the errors are comparable. The large error in L is due to the estimated linear parameter values forming a narrow cloud around the central estimated value resulting in the small slope of figure 2.34a. Therefore, although the absolute errors in the linear parameter are low, the true estimation error is much higher. This indicates that singular values beyond the first two help estimate the tissue modulus effectively. These subsequent singular values, omitted in the reconstructions used here, would provide more detail about the actual parameter, resulting in a more accurate estimation.

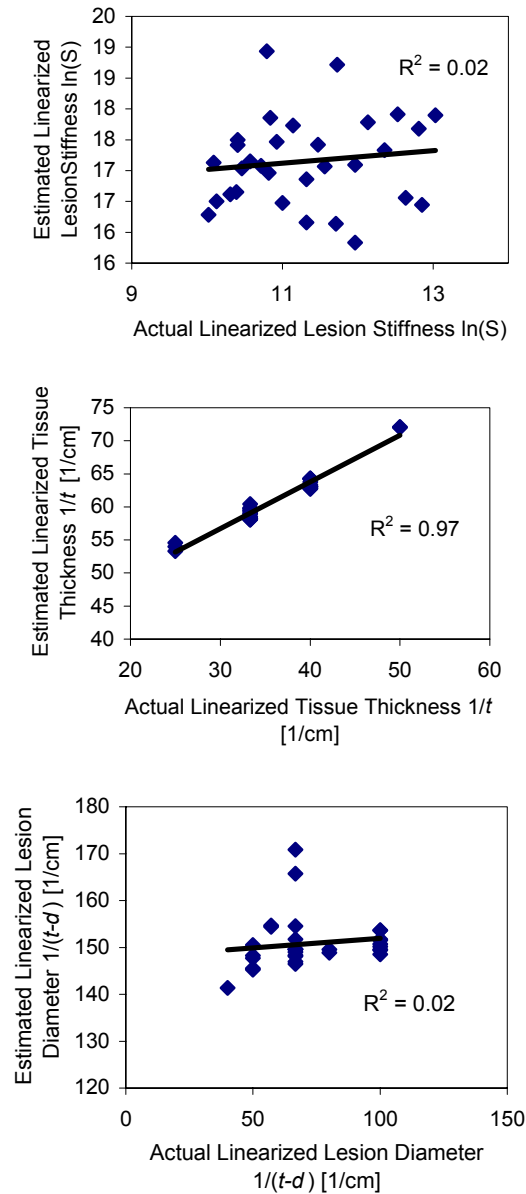


Figure 2.34. Estimating the parameters of interest using transformation matrix A reconstituted from the first two singular values and vectors of the numerical transformation matrix.

2.5.3. Results from the Synthetic Transformation Matrix

The parameters of 32 finite element models with a constant background thickness were estimated using the synthetic transformation matrices shown in figure 2.26. The results are tabulated below. The relationship between the actual and estimated parameters exhibits a larger offset for the estimations using the synthetic transformation matrices than for the numerically generated matrix. In practice this is acceptable, as long as one knows the function of the line relating the estimate to the actual value. The mean absolute error of estimation to this line is shown in table 2.3, along with the mean absolute error for the estimation using the numerical transformation matrix.

Table 2.3. Mean Absolute Errors in estimating the linearized parameters using transformation matrices that are numerically or synthetically generated.

Linearized Parameter	MAE using numerical A from §2.3.4	MAE using synthetic A from §2.3.6
B	0.16%	0.32%
$\ln(S)$	3.3%	4.5%
I/t	2.0%	2.9%
$I/(t-d)$	6.3%	20.3%

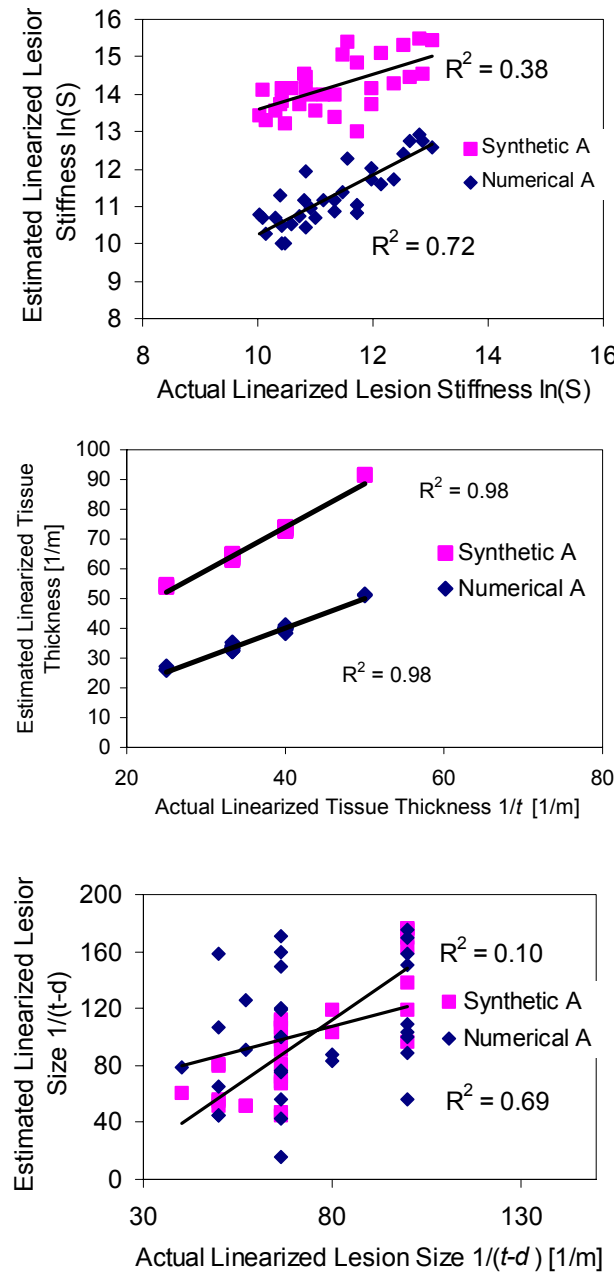


Figure 2.33. Comparison of estimation using the numerical transformation matrix of §2.3.4 and the synthetic transformation matrix of §2.3.6.

From table 2.3 and figure 2.33, we see that the errors from the synthetic transformation matrix are somewhat larger, but on the same order as those from the numerical generated matrix. This suggests that, to the degree that the idealized transformation matrix was based on the analytical reasoning, the reasoning in §2.3.5 is correct. Our results are consistently worse, however. The actual mechanics of our system are beyond the scope of the simple models discussed. The synthetic transformation matrix does not capture the details evident in the numerical transformation matrices. Given the comparable results, however, it is clear that the areas which the synthetic transformation matrix does not address are not vital to the estimation of the tissue parameters.

2.6. Towards Physical Data

2.6.1. Noise Analysis

The finite element model data has intrinsic noise from the discrete element formulation. This noise is well modeled as a uniform noise with a mean that is 3% of the signal magnitude. Real systems, however, are expected to have noise up to 10% of the signal level as discussed in chapter 1. To examine noise effects on the estimation process, this increased noise was modeled by incorporating a uniform random noise in the pressure profiles – both the data sets used to find the transformation matrix as well as the files we tested the estimation on. The results of estimating the parameters of interest with noisy pressure data are shown in figure 2.35.

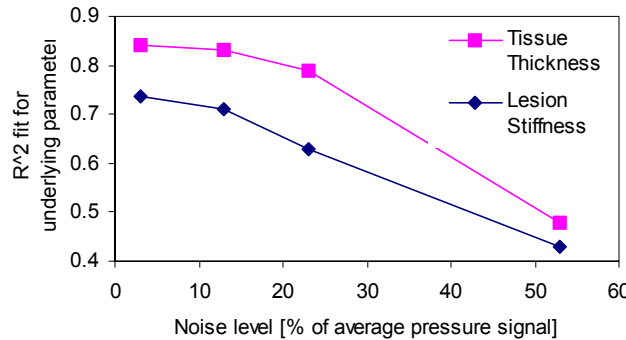


Figure 2.35. Robustness to uniform noise for estimation of tissue thickness (top) and lesion modulus (bottom). The R^2 value remains fairly constant until the noise reaches 10% of the signal value, then falls off as noise increases.

The parameter estimation method is robust to noise since the transformation matrix that is found is a least-squares fit through the space of the transformation matrices that provide the perfect fit for each set $[P, G]$. Collecting multiple overlapping frames also aids in filtering out random noise. This process automatically filters out random noise provided the signal to noise ratio is sufficiently high. From the plot above, we see that the highest levels of estimation accuracy are maintained for signal to noise ratios greater than 10. This level of noise is greater than that expected in real systems.

2.6.2. Tactile System Calibration

The finite element data used in the previous sections was used to both calculate the transformation matrix and test the inversion. In practice, we can employ the same method on physical data. A few Composite Tactile Images should be obtained on lesions

embedded in tissue where the geometry and moduli are known. This parameter and tactile information can be used to find the initial transformation matrix A that can then be used to estimate unknown parameters from tactile information. The values of the parameters in the *a priori* data sets provide the bounds on the ranges of parameter estimation. Barring drift in the tactile imaging system, system calibration occurs automatically in creating the transformation matrix.

2.7. Experimental Validation

In order to test our algorithm on a real system, physical models of spherical lumps embedded in soft material were constructed as described below. The pressure frames for the centerline of the lump were assembled into CTIs as for the finite element model data. For each of the 32 models constructed, a transformation matrix was created from the other 31 models and tested on the data of interest. The parameters for each model are shown in Appendix A.3.

2.7.1. Physical Model Construction

The spherical lesions were made of RTV6166 Silicone (GE). The modulus was controlled by the ratios of the two polymerization chemicals, so that the sphere moduli were between 125 kPa and 500 kPa. The silicone was injected into a mold made of RTV

Mold Rubber (Alumilite Corp., Kalamazoo, MI) so that seven spherical lesion sizes were achieved, ranging from 9.5 to 25 mm in diameter. A thin layer of 500311 Dry Film P.T.F.E. (Sprayon, Cleveland, OH) was sprayed into the mold before pouring the silicone. The soft rubber mold was clamped between rigid ends to assure no flexion in the mold as the spheres hardened. The batches of silicone spheres with different moduli were colorcoded using urethane dyes (Alumilite Corp.) and a cylindrical sample created by allowing at least 30mL of silicone to harden inside the syringe used to inject the silicone into the sphere mold, resulting a cylindrical sample for uniaxial stiffness testing. This allowed for accurate measurement of the actual modulus of each batch of spheres created.

In order to keep the physical models required to a manageable number, the background tissue was simulated with the same RTV6166 Silicone as the spheres, mixed to a modulus of 15kPa, to approximate the modulus of breast fat [Wellman 99], and constant across all models. With the spheres anchored at least 80 mm apart on the bottom of clear rectangular containers with flat bottoms [figure 2.36], the background silicone was poured at different thicknesses, corresponding to the parameter ranges in section 2.1.5. Before imaging, a 0.8mm layer of latex rubber was laid on the surface of the silicone, to simulate skin and to maintain the integrity of the silicone during tactile imaging.

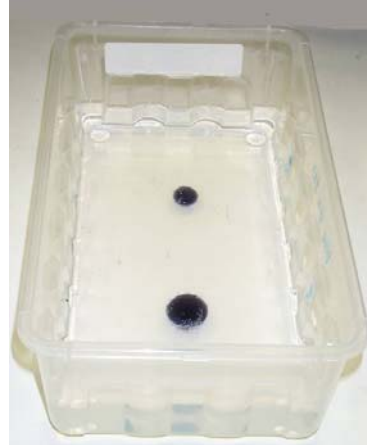


Figure 2.36. Physical model of spherical lesions embedded in soft tissue. The two spheres (dark blue silicone) are attached to the bottom of the container, and embedded in a thick layer of soft silicone. The spheres can be imaged separately using a tactile imager.

2.7.2. Data Collection

At first pass, 8 models were constructed with 2 different spheres each. The laboratory tactile imager introduced in §1.4.1 was mounted on a linear driver and used to scan the surface of the models at 10Hz, moving at 25 mm/s. Weights totaling 1.5 kg were placed on the sensor, resulting in an average sensor pressure of 6.6 kPa. The latex skin was removed from the models and a second layer of silicone added to the models to create models with thicker background tissue. In all, therefore, 32 combinations of lesion modulus and geometry were imaged.

An example tactile map is shown in figure 2.37. This map is constructed from the overlapping pressure frames recorded. The centerline of the frames was found as the row of frames that contained the highest peak (averaged over five frames to eliminate the effect of noise). These centerline pressure frames were assembled into a CTI for each model so that the inversion algorithm discussed above could be applied.

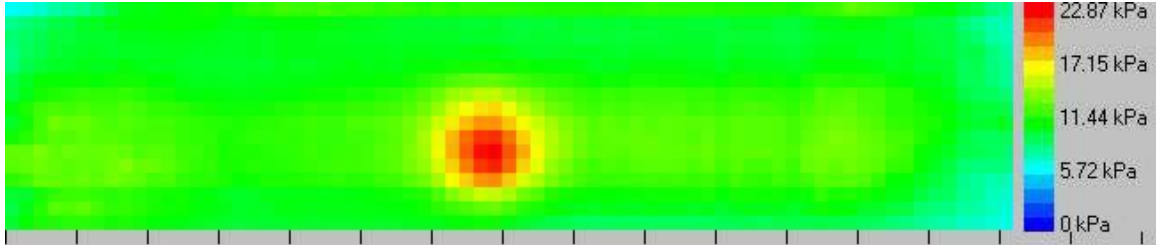


Figure 2.37. Tactile map of a silicone sphere embedded in softer silicone, representing a stiff lesion in soft breast tissue. The parameters of the model are background modulus $B = 15 \text{ kPa}$, lesion modulus $L = 430 \text{ kPa}$, tissue thickness $t = 25.5 \text{ mm}$, and lesion diameter $d = 14.1 \text{ mm}$. The marks along the bottom of the map are at 10 mm spacing. The frames that make up this map were recorded individually and the centerline assembled into a CTI, in order to estimate the model parameters.

2.7.3. Experimental Parameter Estimation Results

The results of estimating the parameters from physical model data are shown in figure 2.38. The errors are summarized in table 2.4. The errors in estimating the geometry are higher than the errors in estimating the lesion modulus. Errors in estimating these parameters may be due to errors in the actual values used for generating the transformation matrix. The model thickness measurement may have errors up to half a millimeter, inherent in the difficulties in measuring the thickness of a soft material. As well, since the second layer was mixed and poured a few weeks after the first layer, there may be a modulus mismatch in the thicker half of our models. This would manifest as an error in the observed tissue thickness. The sphere diameter was calculated based on careful measurements of the rigid spheres used to cast the mold. The silicone spheres, however, did not always fill the mold completely when poured, and the registration of the two halves of the mold was not always perfect (errors of up to 1 mm were observed). Lack of proper mold filling affected the larger spheres to a greater degree, while misregistration of the mold halves had a larger impact on the actual diameter of the

smaller spheres. The modulus of the spheres, on the other hand, was measured repeatedly on samples from the same mixture as the spheres were made of, and so the only errors this was prone to were an improperly mixed silicone mixture and degradation of the silicone over time. Mixing of the silicone was done as carefully as possible, and since these models were cast after much experience had been gathered, it was not observed to be an issue. The silicone itself is also not prone to degradation in the time frame of the model data collection, and so the actual values used for sphere modulus are considered reliable.

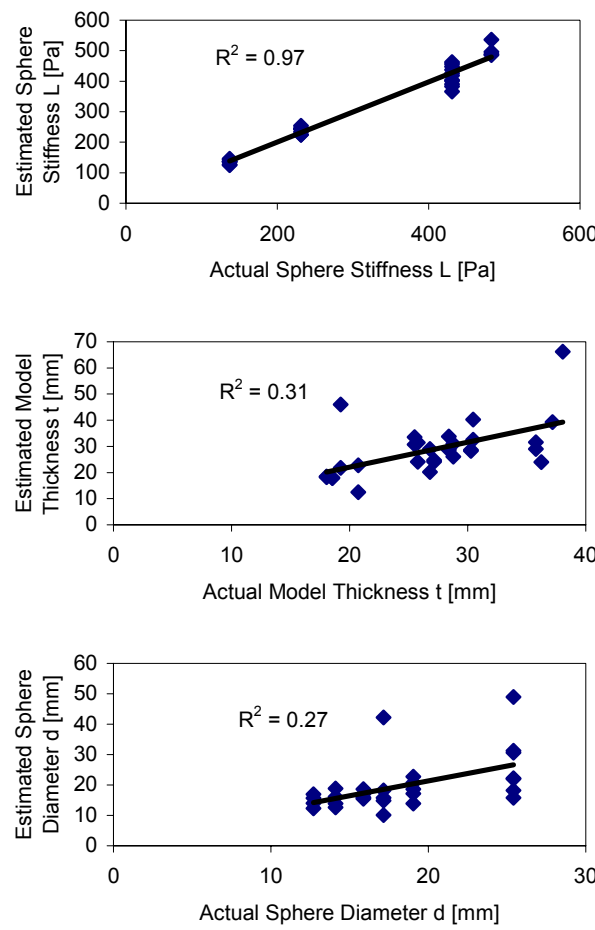


Figure 2.38. Estimating the parameters of physical models using the inversion algorithm developed in this chapter.

Table 2.4. Errors in estimating the parameters of silicone models of a spherical lesion attached to the substrate of a soft tissue.

Parameter	Mean Absolute Error [%]
Lesion Modulus L	5.4%
Lesion Diameter d	16.5%
Tissue Thickness t	13.7%

2.8. Discussion and Future Work

2.8.1. Summary

This chapter presented an algorithm for the estimation of tissue parameters from tactile information. We focused on determining the parameters that define the problem of a round lesion attached to the hard substrate of soft tissue. The parameter estimation algorithm that we proposed relies on a linear relationship between the tactile pressure data and a set of linearized tissue parameters. The transformation matrix at the heart of the inversion algorithm is calculated from sparse data, however since the data follows predictable patterns, the transformation matrix can be modeled by only a few areas of distinct information. This was shown by comparing the estimation results from the transformation matrix to the results of a matrix generated from mechanical reasoning, and to the results of reconstituting the transformation matrix using only its first two singular values and vectors. Since the results were comparable, the transformation matrix must in

large part contain information that is spanned by a few dimensions and thus a linear system, such as the one developed in this chapter, is appropriate for the estimation required.

The parameter estimation algorithm was applied to surface pressure data calculated from finite element models. The estimation of the background modulus was accurate to within 2.3% mean absolute error. If we assume that this is an accurate representation of the background modulus, and use this value in subsequent calculations, the mean absolute errors for the other parameters are 1.9% and 11.7% for the geometry parameters of the tissue and lesion, respectively, and 32.1% for the lesion modulus. These errors are incurred for a background modulus analogous to human breast fat, and can be different for different values of the background modulus. It is reasonable to expect, for example, that with a stiffer background tissue the lesion will have less of an effect on the surface pressure profiles, and so estimating the lesion parameters in these cases may result in larger errors. Previous work by Wellman [99, 01] and Sarvazyan [98c] has shown that even in these cases, however, tactile imaging is more sensitive than human palpation. Any higher error that is incurred, therefore, should still provide for clinically relevant results.

The errors incurred in estimating the parameters of interest from finite element models were low enough to encourage applying the algorithm to data collected on physical models. The errors in estimating the geometry parameters from the 32 physical models

constructed were 13.7% for the tissue thickness and 16.5% for the lesion diameter, while the error in estimating the lesion modulus was 5.4%.

2.8.2. Discussion of Estimation Results

Tactile imaging is inherently a nonlinear process. The linear algorithm developed in this chapter proved successful in estimating the salient parameters of imaged models within the errors noted above. Previous attempts [Wellman 99, Weber 00] at determining tissue parameters from tactile information were unable to estimate modulus information, and instead assumed a model of a rigid lesion. These methods studied tactile information after it had been assembled into a tactile map. The loss of information inherent in the spatial averaging required to generate a tactile map was most likely the greatest contribution to the inability to extract the lesion modulus. The spatial averaging, however, may have aided in the estimation of the lesion size. In Wellman [99], an error of 4% was noted for the estimation of lesion diameter from data obtained on physical models similar to those constructed here. This was for rigid lesions, however. In comparison, when we estimate lesion diameter for the physical models with $L/B = 29$, we obtain a MAE of 10.6%. The increased error is to be expected due to the increased difficulty in estimating parameters of a soft inclusion, as well as possible errors in the physical model data collected, discussed below.

The main key for the success of our linear algorithm is the linearization of the estimated parameters. The linearization functions used were based on basic mechanical analogies and examination of the relationship between the parameters and the resulting pressure information. The linearized parameters were such that the resulting relationship between them and the tactile data features such as the pressure frame peak were approximately linear. The linear algorithm will yield better parameter estimates if the relationship between the parameters of interest and the tactile data was closer to perfectly linear. Possible improvements to the results obtained in this chapter may thus be seen by determining more effective linearization functions. This may stem from a more thorough understanding of the underlying mechanics or from functions fit empirically to the pressure data.

In the case of the finite element model data, the estimation of the background modulus and geometry parameters had smaller errors (MAE for tissue thickness $t = 1.9\%$, lesion diameter $d = 11.7\%$) than the estimation of the lesion modulus (32.1%). The background tissue is in direct contact with the scanhead, and so the pressure profiles collected far from the lesion parameters are directly affected by the background parameters. Similarly, since the lesion is much stiffer than the background, the lesion compresses far less than the background tissue, and so the lesion diameter affects the surface pressure through the effective reduction of background tissue thickness above the lesion. The lesion modulus, however, has the smallest effect on the tactile information collected on the surface of the tissue. This manifested itself in the difficulty in ascertaining an appropriate linearization function, and resulted in the largest error being found for this parameter.

The errors incurred in estimating the parameters from physical model data are in general higher than those incurred in estimating the parameters from finite element data. This is to be expected since the tactile scanning data from the real models has greater noise, as well as additional sources of error such as uneven model thickness and tilt of the model with respect to the scanning direction. The error in estimating the lesion modulus from the physical model data (5.4%), however, was lower than that for the finite element data (32.1%). This is due to the fact that the lesions themselves were larger in the physical models (minimums were 12.7 mm in the physical models and 5 mm in the FE models), due to difficulties in casting small spheres accurately. Although the smaller range for the lesion diameter did not decrease the errors in estimating the lesion diameter, it aided in the estimation of the lesion modulus, as the larger lesions resulted in a stronger signature from the lesion in the pressure data.

The finite element models were constructed with a plane strain assumption, in which a round lesion models an infinitely long cylinder. This would result in a stronger contribution from the cylinder than that expected from a spherical lesion and thus we may expect smaller errors in the estimation of the lesion modulus from the plane strain finite element models. The results obtained from the physical model results, however, showed a decrease in the errors of estimating the lesion modulus, as discussed above. Therefore, we can conclude that the plane strain approximation used in the finite element models in order to simplify analysis did not diminish the development of an inversion algorithm for tactile information.

2.8.3. Towards Clinical Data

The finite element models used for the above analysis modeled the nonlinear contact problem and the nonlinear geometric deformations, but did not model the nonlinear material properties of real tissues. The physical models studied, although more realistic in several ways, were constructed from homogenous materials with a linear elastic modulus. The physical models were three-dimensional, and imaged with a physical sensor that is similar to that expected to be used clinically. The edges of the constant thickness background tissue in the physical models, however, were constrained by the rigid sides of the model container. Clinical cases will not have such well-defined boundary conditions, and instead will involve tissues of varying thickness, in which are embedded lesions that are not perfectly spherical. In addition, biological tissue is inhomogeneous even at the macroscopic level, and exhibits a greater elastic modulus with increasing strain. Although our linear algorithm showed low errors in estimating the required parameters from the model data collected, the estimation errors will most likely increase in a clinical setting with less constrained boundary conditions and nonlinear tissues.

The effect of the rigid sides of the physical model, which required the background tissue to bulge up, is unknown. The models were constructed such that the lesions were far from the sides as compared to both their diameter and the distance from the surface, so the effect of the rigid sides is expected to be minimal. The varying tissue thickness of

physical tissue will affect the estimation of this background parameter, since the estimation algorithm was developed to estimate a single constant related to the tissue thickness. Given the symmetric data collected in the CTI as presented here, an average tissue thickness should be the parameter of interest. This condition will be explored in detail in the next chapter.

Nonspherical lesions will also affect the performance of the estimation algorithm. Barring extreme cases where the lesion is very thin in the depth dimension, distortions in this dimension are expected to have a minimal effect on estimating a representative lesion diameter, as evidenced by the minimal effect the plane strain assumption had on the estimation results. Considering the areas of the CTI involved in estimating the lesion diameter, we expect that the maximum diameter through the vertical dimension will be the representative size estimated by the algorithm.

A nonspherical lesion shape will also affect estimation of the lesion modulus. Considering the areas of the CTI involved in calculating this parameter, an asymmetry in the lesion shape will most likely result in an average depth-averaged modulus being calculated. The extent of dependence of the estimation on the actual lesion shape should be explored in detail. In chapter 4 we will explore the problem of estimating the parameters of a lesion of varying height.

The effective elastic modulus of biological tissue increases with increasing strain. The algorithm developed here estimates only one parameter for modulus for each of the two

tissues modeled. This is not sufficient to capture the entire stress-strain relationship of the materials, however in the case of physical data will result in one salient feature of the curve being calculated. Since we collect our tactile data at a constant force, tissue with a lower average modulus will be subjected to greater average strain and is thus imaged at a representatively higher modulus and vice versa. Although this will reduce the effective extent of the range of tissue moduli, this effect is small compared to the difference in moduli between tissues in the breast, and so should not greatly affect the ability to discern the difference between imaged tissues. Small differences in the modulus within the bulk of each tissue will at worst manifest as noise in the data, whose effect on the success of the estimation algorithm is minimal.

The data studied in this chapter was collected with a constant input force. In a clinical setting, a human operator will perform the data collection, and so the total input force is expected to vary. Although we can limit the data collection to pressure frames collected within a small range of input force, this range cannot be infinitely narrow, due to human variability. Due to the nonlinear stress-strain relationship of biological materials, we cannot fully account for the varying total force by simply normalizing the collected pressures. Indenting the tactile scanhead by different forces into the same tissue, however, probes the tissue at different strains and depths, and thus provides an even more complete picture of the tactile extent of the tissue than probing at one force. We can then use the tendency towards a varying input force to our advantage, and, for example, require users to scan the surface of the tissue a few times at different forces. By keeping frames collected within a few narrow ranges, we can estimate the parameters of interest

for each pressure range and obtain a more complete picture of the underlying tissue. Although estimates of the geometry should not change, this method may enable us to obtain a more detailed stress-strain curve for the constituent tissues.

2.8.4. Future Work

The ultimate goal of developing the estimation algorithm is to take this work to a clinical setting. The expected difficulties discussed above in dealing with clinical data may result in increased estimation errors. The possible sources of error can be explored more fully by obtaining data from physical tissue such as excised biological tissue before a final move to *in vivo* data.

The estimation technique outlined here may be improved upon by the addition of further information. For example, ultrasound information can be used in conjunction with our algorithm to generate a more accurate estimate of the tissue geometry. An ultrasound transducer can easily be incorporated into the tactile imager scanhead. The merits of such an approach will have to be weighed against the resulting increase in cost of the combined device. Obtaining multiple scans at different levels of input force may help also reduce these errors and provide more detailed information on the imaged lesion. The value of either technique should be studied on models in work similar to in this chapter before being applied to clinical data, so that we may understand its contribution in a controlled setting.

The ideal test bed for this work is tactile data obtained on women with a known lesion that is about to be excised, similar to the clinical trial of the work performed by Wellman [99]. Upon excision, the parameters of interest can be measured directly and compared to the estimates generated from application of our algorithm. With proper accounting for the errors inherent in imaging physical tissue, the accuracy of parameter estimation from tactile imaging can be established. Low errors may make this technique useful in applications such as breast cancer screening, or for long term tracking of benign lesions.

Chapter 3

Round Lesion in Soft Tissue

3.1. Introduction

The analysis outlined in chapter 2, for the case of a lesion resting on a rigid substrate, models many cases of breast pathology. There are several cases of interest, however, where a more appropriate model would allow for the lesion not to be attached to the substrate. This includes not only cases of breast pathology in women with large breasts, but also conditions in other organs.

Most solid organs, such as the liver and prostate, do not have a rigid substrate like the chest wall provides for the breast. Lesions that develop in these organs, however, are subject to the same mechanical constraints as those that develop in the breast, and therefore tend to be round. Pathologies in these organs, then, can be modeled by a round lesion embedded in soft tissue. A rigid substrate can be considered on one side of the model to represent the skeletal structure near the organ. This model is illustrated in figure 3.1. Nonpathological features, such as the large blood vessels of the liver, are also well modeled by this figure, where the inclusion is a cylinder of pressurized liquid

instead of a solid lesion. We would like to develop a method of estimating background, lesion and vessel parameters from these organs based on tactile information obtained on their surface. Practically, this will eventually need to work with a smaller tactile imager that can be employed in minimally invasive surgical settings, however as a first pass, we will work with the tactile imagers at hand and determine a method for estimating parameters of interest on these organs.

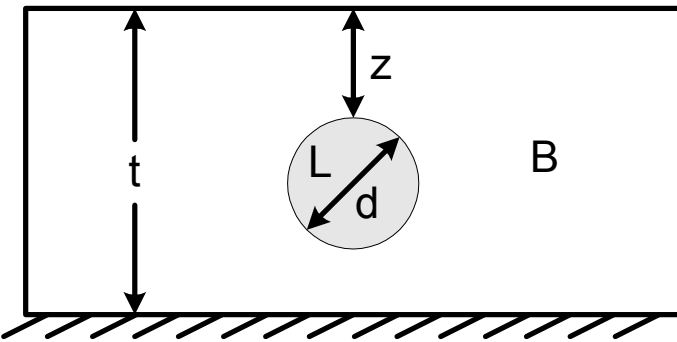


Figure 3.1. Model for parameter estimation from tactile information. The lesion is allowed to ‘float’ in the tissue, and is no longer attached to the rigid substrate. The other parameters and assumptions remain the same as in figure 2.2.

In this chapter we will study the applicability of the algorithm developed in chapter 2 to the case of a round lesion wholly encased in soft background tissue. To the parameters for estimation B , L , t , and d (Background and lesion modulus, tissue thickness, and inclusion diameter, respectively) we therefore introduce a fifth parameter, z , the depth of the lesion, which must also be estimated from the tactile information. We will study the estimation method on results obtained from finite element models constructed with the same assumptions of chapter 2. We will divide the study into two sections: the first for studying solid lesions, such as breast pathology in large breasts or liver, and the second for hollow lesions, such as large veins in liver.

3.2. Mechanical Modeling

A plain strain finite element was constructed with the same finite element mesh geometry for the upper portion of the model as in figure 2.8. The model was extended under the lesion so that the lesion was now completely enclosed by the background tissue and ‘floating’ above the substrate at various heights. The model is composed of incompressible, isotropic, linearly elastic tissue. The interaction between the indentor and the tissue surface is frictionless.

In the modeling of solid lesions stiffer than the background in which they are embedded, we are interested in modeling within the physiological range of the human breast. To that end, the parameter ranges as outlined in §2.1.5 were used, with the addition of the height h of the bottom of the lesion above the substrate. The height h , which varied from 5 mm to 40 mm, is related to the depth z shown in figure 3.1 as $z = t - d - h$. This range encompasses the expected geometry of breasts with a high fat composition and the maximum expected thickness of the human liver beneath a lesion. The parameters for the models created are listed in appendix A.4. In the modeling of blood vessels, we are interested in modeling the large vessels in human livers, with an eye towards testing our algorithm on porcine liver. This requires different parameter ranges than the breast models. The background modulus B of the soft inclusion models was therefore varied in the range of 10 kPa to 15 kPa, in order to encompass average moduli ranging from human to porcine livers [Carter 01, Ottensmeyer 01]. Based on the anatomy observed

during the dissection presented in §1.4.4. and expected human anatomy [Gray 02] the thickness t of the model tissue varied in the range of 40 mm to 60 mm. Also, the vessels, whose diameter d varied in the range from 5 to 10 mm, were set in the middle of the tissue. This reduced the liver models to 4 parameters:

B = background modulus

t = tissue thickness

z = depth

$=(t-d)/2$, where d is the vessel diameter

V = vessel pressure

where the vessel pressure V is considered instead of the lesion modulus L of the earlier models.

Finite element models of liver with a central vessel were studied for vessel pressure in the range of 0Pa to 5Pa, corresponding to the pressure ranges expected for the hepatic vein. It was found that the tactile information that results from modeling tactile scanning of these models varied by less than 5% over the entire pressure range. Therefore, it was decided to eliminate the vessel pressure and model the liver as a slab of tissue with a hollow cylindrical area in the center. The parameters for the liver models created are listed in appendix A.5.

3.2.1. Linearized Parameters

In the case under study here, we have a new parameter, z , the depth of the lesion, to account for in our estimation algorithm. For a lesion stiffer than the background, we surmise that due to the relative incompressibility of the lesion, the pressure recorded above the lesion will be related to z in a similar manner that the background pressure is related to the tissue thickness. Therefore we take the inverse of the depth of the lesion, $1/z$, as the linearized parameter for our algorithm. A plot of the linearized parameter $1/z$ versus the maximum pressure seen over the lesion confirms that this linearized parameter is a positive increasing value [figure 3.2].

The addition of the new parameter also changes the parameter used for the lesion size d . Earlier we had taken the parameter $1/(t-d)$ as the linearized parameter in our algorithm. In this case, since the models of interest are much thicker, and we know that the surface material affects the tactile frames more than the deeper material, we take d/z as the linearized parameter from which to estimate the lesion diameter d . Figure 3.2 shows that indeed, the parameter d/z is more directly related to the pressure calculated over the lesion than the parameter $1/(t-d)$.

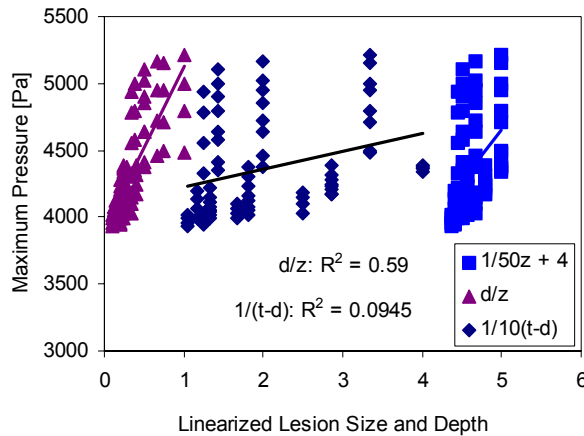


Figure 3.2. Linearized geometry parameters for solid lesion embedded in soft tissue. The values on the x -axis have been linearly scaled in order to plot the values on the same axis.

For the case of the embedded vessel, the maximum pressure calculated over the vessel shows a wide spread for the depth parameter z , however a slightly improved linear fit can be seen to the parameter $1/z$ ($R^2 = 0.04$) than for the plain parameter z ($R^2 = 0.03$). Although both values do not seem well related to the maximum pressure calculated over the vessel, the slight improvement for $1/z$ prompts us to use this in the estimation algorithm.

Finite element analysis was performed on the 95 models created, and tactile scanning data was calculated every 2.5 mm for an 80 mm extent centered on the lump. The data was compiled into Composite Tactile Images, and used to find the transformation matrix \mathcal{A} as outlined in §2.2.6. The all-but-one algorithm was used to test our linear inversion algorithm on the finite element data.

3.3. Solid Lesion Results

The results of estimating the parameters of interest for the finite element models created with a single floating solid lesion are summarized in table 3.1.

Table 3.1. Error in estimating the underlying parameters for models with a floating lesion.

Parameter	Mean Absolute Error in Estimation
Background Thickness t	2.9%
Lesion Diameter d	14.1%
Lesion Depth z	7.9%
Stiffness Parameter $S = [Ld + B(t-d)]/t$	35%
Lesion Modulus L	94%

The errors shown in table 3.1 were incurred in estimating lesion modulus when the transformation matrix A was created from files spanning the entire range of interest. The errors in estimating the geometry parameters are on par with those for a fixed lesion. The errors in estimating the lesion modulus, however, are too large to be of clinical use, so a different approach must be taken for these models.

Closer examination of the composite tactile images generated from these models shows an interesting trend in a simple value called the Composite Tactile Image Amplitude (*CTIa*). The *CTIa* is a measure of the strength of the signal contained in the CTI. It is a ratio of the highest values contained in the frames, specifically the highest value of the CTI, CTI_{peak}^{\max} , to the lowest highest value in a frame, CTI_{peak}^{\min} , normalized to yield zero in the absence of a lesion:

$$CTIa = \frac{CTI_{peak}^{\max}}{CTI_{peak}^{\min}} - 1$$

In cases such as the ones under consideration, that of a CTI taken of a single lesion embedded in the middle of the region of data collection, the highest value occurs centrally, while the lowest high value occurs in the center of a background frame. Since the data contains some noise, the actual values used for the $CTIa$ are averages of a 3×3 region in the CTI, corresponding to 3 values along a frame by three adjacent frames.

The $CTIa$ is fairly stable across lesion modulus for models of the same geometry, and a plot of $CTIa$ versus lesion modulus shows the $CTIa$ values clustering for similar geometries modeled [figure 3.3a]. Plotting $CTIa$ versus a dimensionless geometry ratio d/z for all models confirms this separation of the data [figure 3.3b]. We see a distinction around $CTIa = 0.125$. The tissue parameters within the ranges of interest result in $CTIa$ clusters that do not cross this line. If the ranges of interest were much larger, the trends evidenced in figure 3.3a are expected to continue, and the division at $CTIa = 0.125$ will disappear. This division may also blur in the presence of noise larger than that present in the finite element data. With a random noise, however, simple averaging should be able to account for the majority of it and this should only contribute to errors in a small percentage of the cases studied.

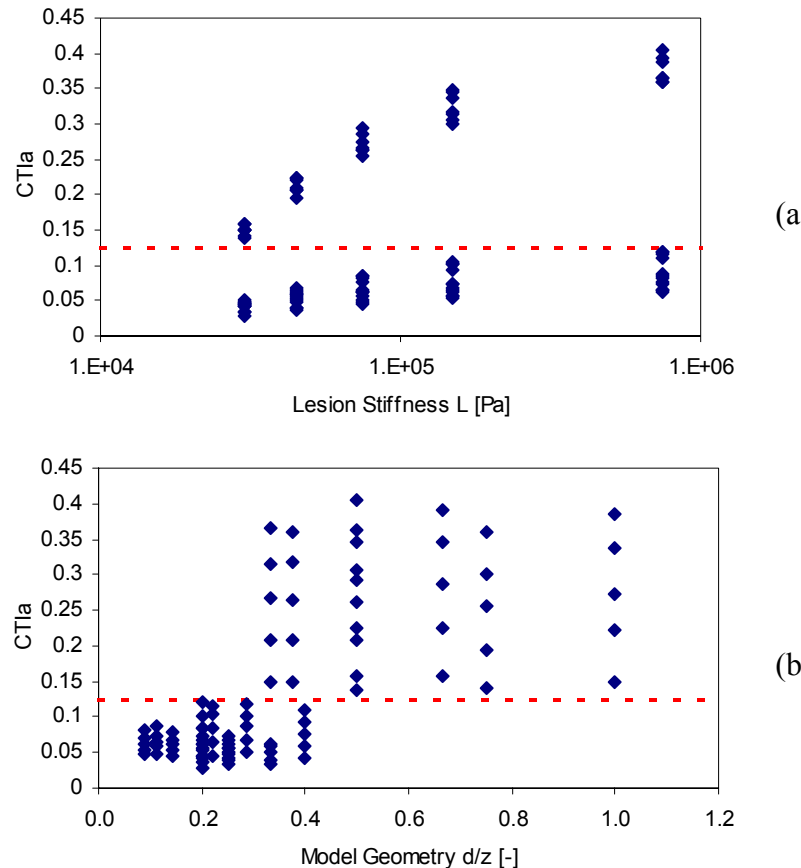


Figure 3.3. The $CTIa$ for cases of a solid lesion in soft tissue shows a separation for values greater or less than 0.125, indicated by the dashed line. (a) $CTIa$ versus lesion modulus. The $CTIa$ aggregates according to the underlying geometry. (b) $CTIa$ versus model geometry.

This result provides a new way of approaching the parameter estimation for floating lesions. Namely, breaking up the data set into two parts, one with high $CTIa$ values and one with low $CTIa$ values. This necessitates the generation of two transformation matrices. Since each transformation matrix will be created with less data, this is computationally more expedient than keeping one large data set. Practically, once the tactile information is collected, the $CTIa$ is calculated in order to ascertain which

transformation matrix to apply to the data. Using this approach on our finite element data, the errors incurred are those shown in table 3.2 and figure 3.4.

Table 3.2. Error in estimating the underlying parameters for models with a floating lesion using different transformation matrices based on the $CTIa$

Parameter	Mean Absolute Error	
	$CTIa < 0.125$	$CTIa > 0.125$
Background Thickness t	2.2%	3.6%
Lesion Diameter d	6.3%	7.5%
Lesion Depth z	2.2%	3.6%
Stiffness Parameter S	13.6%	7.5%
Lesion Modulus L	33.1%	11.8%

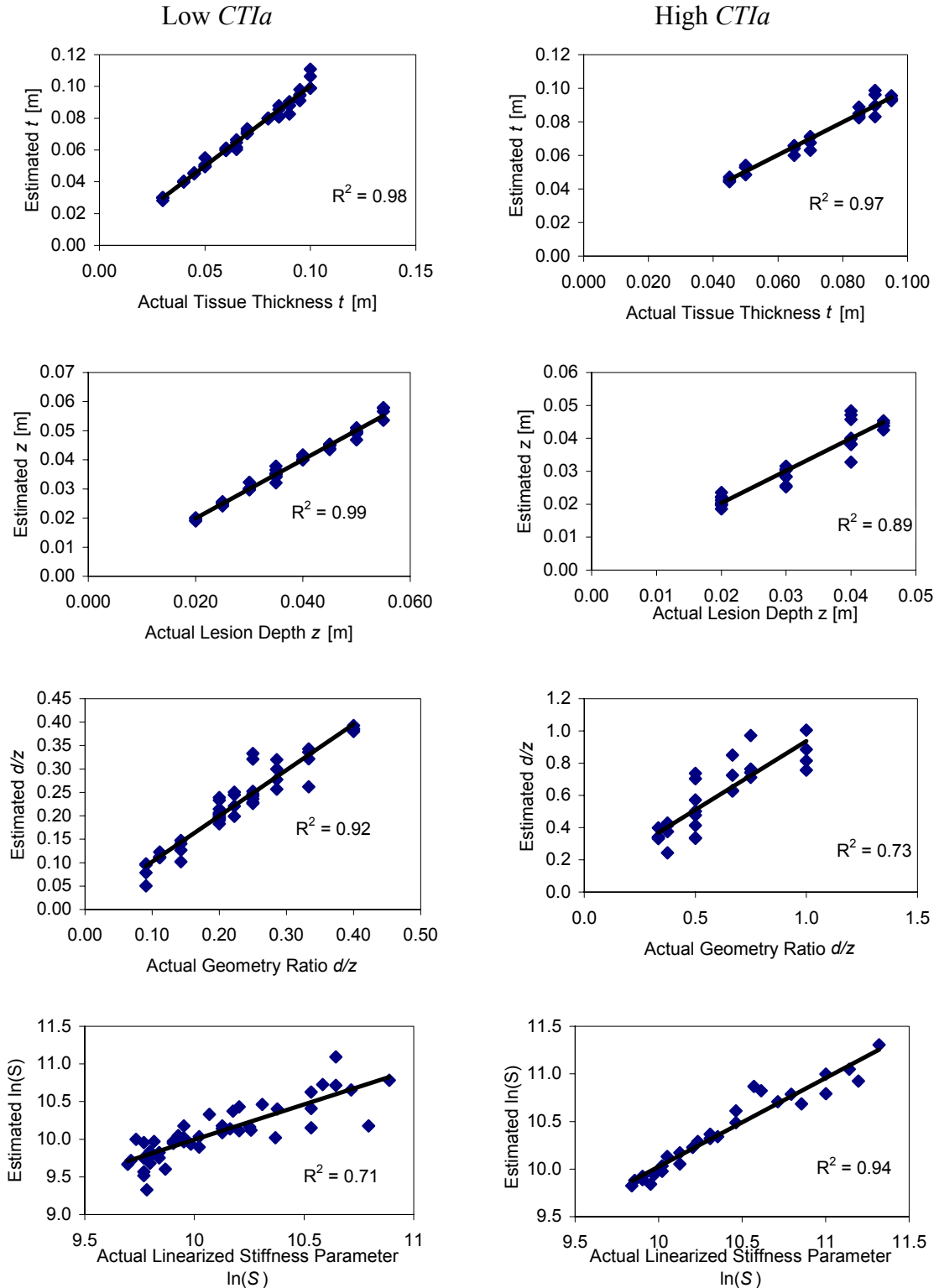


Figure 3.4. Results of estimating underlying parameters for finite element models of a solid lesion embedded in soft tissue.

3.4. Vessel Parameter Estimation

As a preliminary test of our algorithm, finite element models of liver segments with hollow vessels were used to obtain the required tactile information. Thirty-six models were analyzed that spanned the range of parameters outlined in §3.2. Tactile scanning data was recorded every 2.5 mm, and the pressure frames recorded in CTIs. In this case, since the inclusion is softer than the background, the CTI centerline is the inverse of that from the previous sections. As shown in figure 3.5, the hollow vessel manifests as a region of lower pressure in the middle of the CTI.

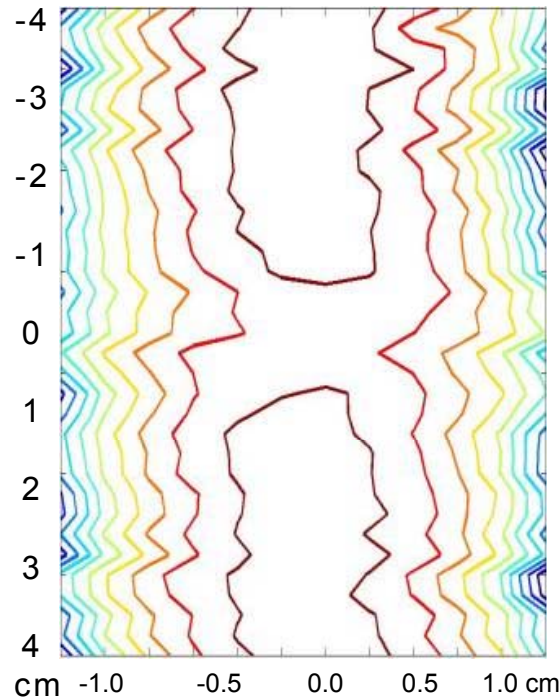


Figure 3.5. Contour plot of a Composite Tactile Image obtained from a model of liver tissue with embedded hollow vein. The axes indicate distance along the sensor (x-axis) and distance from vessel (y-axis). The CTI values are slightly lower in the middle, indicating the presence of a soft area.

In this case, the $CTIa$ is the ratio of the maximum of a background frame to the maximum of a frame collected over the vessel. The $CTIa$ increases with decreasing vessel diameter, and is equal to zero in the absence of a vessel. Although this trend was indeed seen [figure 3.6], there was no clear-cut point at which we can separate the models to yield two distinct accumulation matrices. For the range of parameters used, the $CTIa$ varied between 0.025 and 0.095. Because of this lack of separation, all the results were lumped together to generate one transformation matrix.

As in the previous sections, for each of the model data sets, the other 35 models were used to generate a transformation matrix to estimate the parameters from the pressure frame data. The results of estimating the model tissue and vessel parameters are shown in figure 3.8 and summarized in table 3.3.

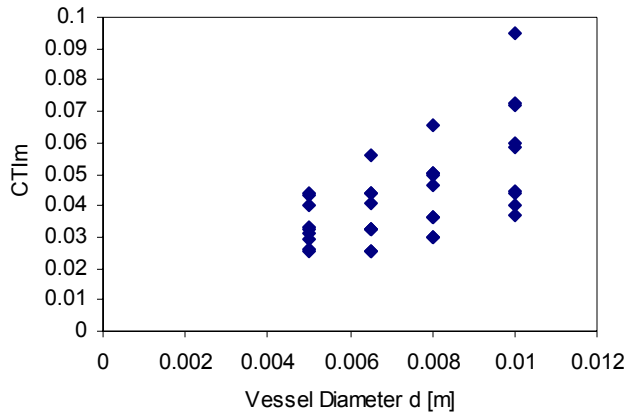


Figure 3.6. $CTIa$ for finite element model data of liver with hollow vessel.

Table 3.3. Mean Absolute Error in estimating the underlying parameters of liver finite element models.

Parameter	Mean Absolute Error in Estimation
Liver Modulus B	0.81%
Liver Thickness t	9.3%
Vessel Depth z	7.2%

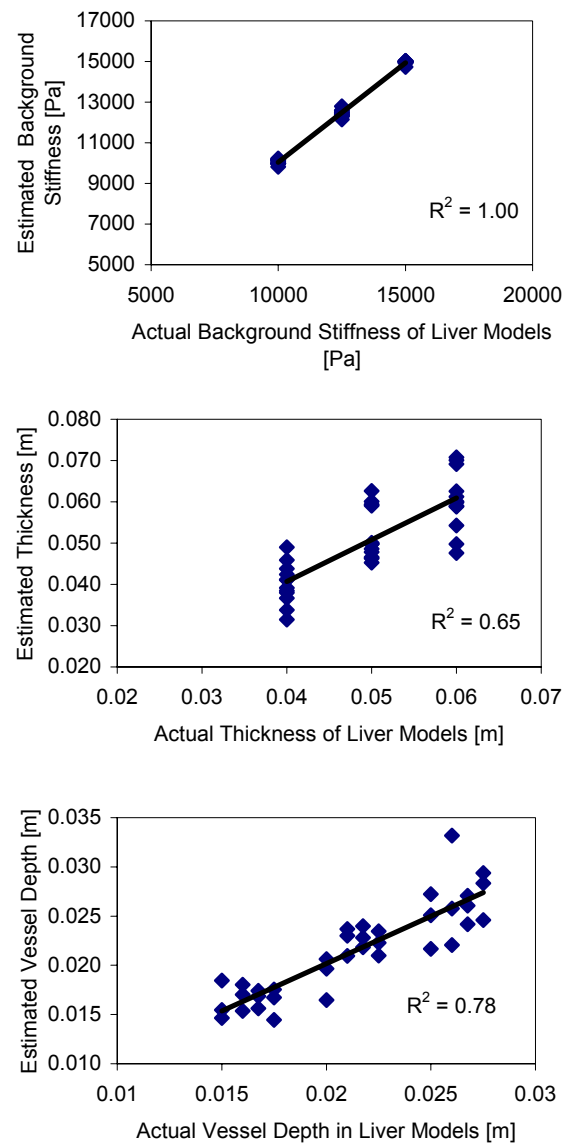


Figure 3.8. Estimating underlying parameters from finite element models of livers with embedded vessels.

3.5. Experimental Results

In order to test our parameter estimation algorithm on real tissue, two porcine livers were obtained. The livers were from healthy 40kg pigs and were harvested within one hour of sacrifice. They were immediately flushed with heparin to eliminate blood clots. Perfusion with physiological saline solution at 36°C was started approximately one hour later. Each lobe was imaged with the laboratory tactile imager discussed in §1.4.1 and tracked in three-dimensions. Vessels were found in tactile images as shown in figure 3.8.

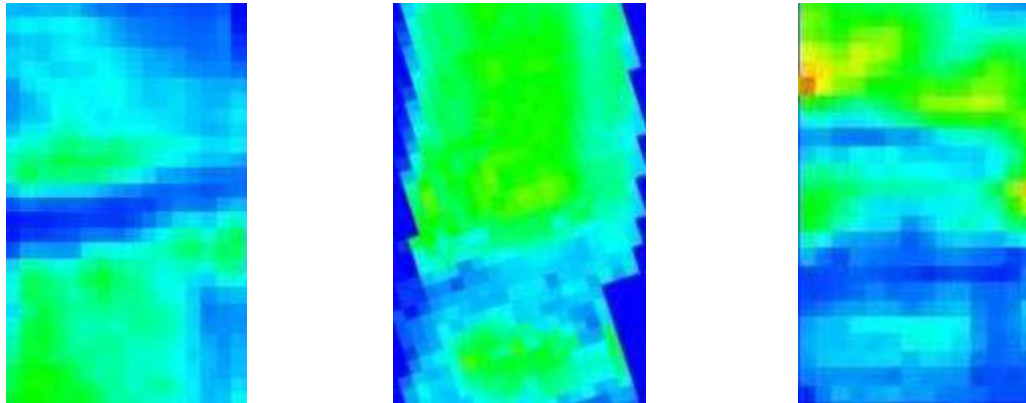


Figure 3.8. Tactile maps of sections of porcine liver lobe, showing decreased pressure over vessels. The left and center images show one vessel each spanning the width of the image, indicating the presence of a large vessel beneath the surface. The image at right shows two vessels running from left to right, with the upper one leaving a smaller impression in the tactile image (due to smaller size or greater depth). The images shown are approximately 80 mm x 40 mm.

Eight vessels were found in the two porcine livers, and multiple tactile images were made of many of the vessels, to result in 14 usable maps for testing our inversion algorithm. For each set of tactile image data, tactile frames were extracted every 2.0 mm for a 40 mm linear region centered on the vessel. This tighter spacing was prescribed by the fact

that the thin porcine liver lobes vary considerably in thickness, and even over a 40 mm section the thickness varied up to 15 mm. Since the images were obtained using a hand-held sensor the pressure applied varied for each frame. The average pressure across all the frames of interest was 18.2 ± 10.3 Pa.

For each set of data in turn, the transformation matrix was found using the other 13 sets of data and the parameter estimation tested on the set in question. The actual parameters were recorded after tactile imaging was complete by dissecting the liver lobes and measuring the vessel diameter, depth from surface, and total tissue thickness. The background modulus was assumed to be the same across all samples, since the subjects were both healthy pigs of the same age raised together. The results of estimating the actual parameters using our inversion algorithm are summarized in table 3.4 and shown in figure 3.9. The vessel depth and diameter were calculated independently since in the thin livers available for our study, an assumption of a perfectly centralized vessel would have resulted in a nontrivial error source.

Table 3.4. Results of estimating the underlying parameters of porcine livers with large embedded veins.

Parameter	Mean Absolute Error in Estimation
Liver Thickness t	20.0%
Vessel Diameter d	25.6%
Vessel Depth z	13.6%

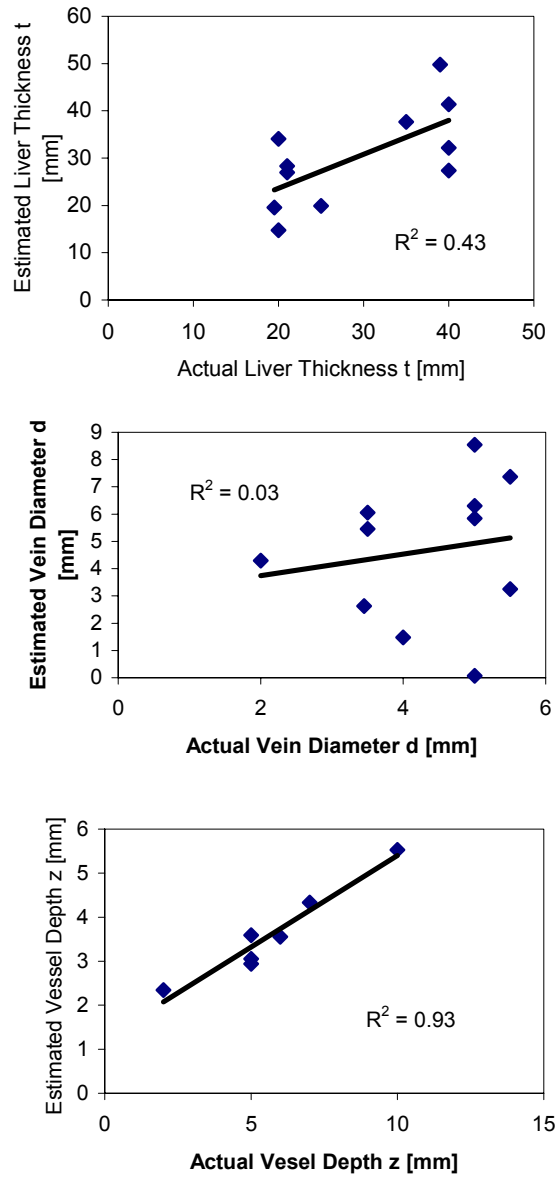


Figure 3.9. Estimating underlying parameters of a vein embedded in porcine liver tissue.

3.6. Discussion and Future Work

This chapter has detailed the estimation of parameters from models and physical structures with a lesion embedded in tissue but not attached to the substrate. We broke the problem into two parts, the former dealing with lesions stiffer than the background, as in cases of breast or liver pathology, and the latter dealing with inclusions softer than the background, such as estimating the geometric parameters of a large vein in the parenchyma of a liver.

In the case of a solid lesion embedded in soft tissue, we found that estimating the model parameters was improved by breaking up the data into two sets, depending on the value of the Composite Tactile Image Amplitude ($CTIa$). Estimations of the background and geometry parameters showed comparable errors between the low and high $CTIa$ values, however the estimation of the lesion modulus had notably lower errors for models with a high $CTIa$. This is to be expected since a high $CTIa$ implies that a stronger signal from the lesion is contained within the tactile frames.

Estimation of parameters for the case of a solid lesion was facilitated by a separation found in the data sets, depending on the $CTIa$. Such a division was not found for the case of a hollow vessel, most likely due to the range of the parameters of interest. Figure 3.3 shows the spread of the $CTIa$ for the cases of a solid lesion studied above. If the lesion modulus was allowed to continue to increase, the trend of the lower data clusters will

continue, and eventually overlap the values of the data in the upper trend. The lesion modulus required for this, however, is outside the physiological range of interest. In the case of the hollow vessels, the range of interest does not allow for a clear delineation of the data.

For the case of a hollow vessel embedded in tissue, the results obtained on the finite element models showed promisingly low errors. The estimation on physical livers tested resulted in errors approximately twice those of the finite element models. This is not surprising, given the unconstrained data collection in the laboratory setup and the nonlinearities inherent in the tissue properties not modeled in our finite element analysis. A prime difference between finite element analysis and physical data collection is the large range of input pressures observed during physical data collection. This variable is controlled to better than 1% in the finite element analysis, but was observed to vary up to 30% in the physical data collection, due to human operation of the tactile system.

This non-zero input pressure range affects the data in two ways. The first is that due to the nonlinearity of the tissue modulus, we inadvertently probe the tissue at different effective moduli. Because of this, we cannot simply normalize the frame information by the difference in the total applied force. However, this change in the effective background modulus will result in an incorrect measure of the tissue thickness, since we had assumed a constant background modulus. The wide range of input pressures also affects the way the tissue is probed in that as the tactile imager is indented further into the tissue, the surface pressure is informed from deeper tissues [Sarvazyan 98], which results

in information that our simple parameter system cannot handle. This problem of a wide range of applied forces can be improved by implementing software control on the tactile data, only allowing data to be obtained in a fixed range of total force, and providing positive feedback to the user when they are operating in the acceptable range.

The sensor used was not ideal for the porcine livers tested, as their stiffer parenchyma and thin cross-section requires a flatter sensor to allow all of the pressure sensors on the tactile imager to contact the tissue. With the sensor used, in almost 10% of tactile frames only 14 of the 16 centerline sensors recorded any contact pressure. Rather than present the inversion algorithm with artificial zeros at the end of frames, all of the frames were truncated to 14 pressure points in width. This did not adversely affect the mathematics of the algorithm, as it has been shown to work for a sensor of finite width smaller than the contact area. The smaller number of data points, however, decreases the oversampling buffer than aids tactile scanning in performing parameter estimation accurately.

With only eight vessels found in the two livers studied, the parameter range was sampled only sparsely. Obtaining extra maps on some vessels allowed for estimation of all map parameters, since we were not extrapolating for any one variable. Maps taken on the same vessel were not identical, and so represented different maps taken on vessels with similar parameters. Since these double maps were not identical, however, they may have negatively affected the parameter estimation, by providing a different pressure signature for the same parameters. As seen by the distribution along the x -axes in figure 3.9, the duplicate maps were well spaced over the tissue thickness and vessel diameter, but were

biased towards larger diameter vessels since the smaller vessels were difficult to image repeatedly, most likely due to temporary collapse. Therefore, although the total parameter range was spanned, the estimation of the vessel diameter was most likely adversely affected since the range spanned by the majority of the data was narrow, with more than one pressure profile representing the same diameters.

The liver parameters were only recorded after all maps were taken, by cutting the lobe perpendicular to the vessel along the line of data recording. Recording the parameters this way is the most direct and readily available method, however may have contributed incorrect vessel parameter information. Since the cutting and data recording were done by hand, the planes of tactile data and dissection may be offset by a few millimeters. In this range, the vessel diameter and tissue thickness may vary as well. The vessel diameter may vary by up to a millimeter and the tissue thickness by twice that. The liver parenchyma also was prone to swelling in the cut plane. This is due to the natural tension that is present in the liver, maintained partly by the perfusion under which the data was recorded. Perfusion was necessary, however, in order to maintain mechanical viability of the liver, so that despite the above sources of error, subsequent maps recorded on the same vessel record approximately the same conditions. These sources of errors contribute mainly to the input parameters, and may adversely affect the apparent estimation by presenting incorrect information for the creation of the transformation matrix. These errors can contribute a relatively large error to the parameters in question, and so the above work should only be considered a proof of concept for the use of tactile

scanning to record liver vessel parameters. Within these constraints, the algorithm performed remarkably well in estimating the underlying parameters.

With the data separated according to the *CTIa*, the results obtained from the finite element data for floating lesions are comparable to those obtained in the previous chapter for fixed lesions. Therefore, the next step in the study of estimating the geometry and modulus of an inclusion embedded in tissue should be on data obtained from physical models. Once the estimation algorithm is shown to work well for physical models, actual tissue with embedded inclusions can be studied. Much like the work described above for analyzing actual liver vessels, tactile data should be obtained immediately before dissecting the tissue for measuring the actual parameters. Reasonable results from this will be a required step to moving on to estimation of lesion parameters *in vivo*.

In the case of liver vessel parameter estimation, further work should be conducted on physical livers, after the main causes of error noted above are addressed. Specifically, a flatter indentor should be employed for porcine livers so that the tactile frames involve all of the available pressure sensors. Also, a method for applying a near-constant force should be utilized. This can be as simple as generating a specific sound for when the data collected is in a narrow range around the ideal input pressure [Wellman 01]. Obtaining larger porcine or bovine livers may also help since they would be closer in thickness to human livers. Ideally, human *ex vivo* livers will be tested before moving ahead to an *in vivo* setting using a smaller tactile imager in minimally invasive data recording.

Chapter 4

Continuous Estimation

4.1. Introduction

The parameter estimation problems outlined in the previous two chapters are based on ideal models that are most realistic when compared to organs composed of a homogenous tissue with an isolated inclusion. There are important cases, however, that include a more diffuse region of stiff tissue. This includes the cases of young premenopausal women and women with fibrocystic change. Both of these cases involve glandular tissue and possibly lesions which have palpable features under a layer of surface fat. This is depicted schematically in figure 4.1. These cases are difficult to record in most imaging modalities, including mammography and manual palpation [Pennypacker 99]. However, especially in the latter case of fibrocystic change, since these women are at a higher risk for developing breast cancer [Thomas 97], monitoring of their underlying fibrous tissue is extremely important. Such monitoring is invaluable in determining when a lesion has developed.

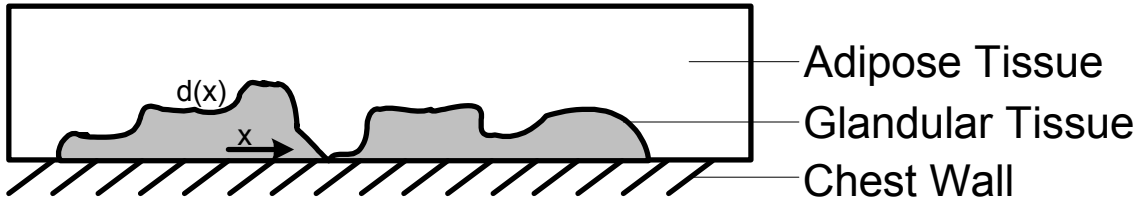


Figure 4.1. Model that represents the case of fibrocystic disease and young women with stiff glandular tissue. The total thickness is assumed to be uniform regionally, but the thickness of the glandular tissue layer varies continuously.

In this chapter we develop a method for estimating the shape of the underlying layer of glandular tissue in cases such as that in figure 4.1 from the tactile information obtained in tactile scanning. The general problem of estimating a substrate with continuously varying thickness and modulus is ill conditioned, so we will simplify the system and gain as much insight as possible from the simplified problem. Since a linear algorithm with linearized parameters showed success in discrete parameter estimation in chapters 2 and 3, we will seek a linear algorithm for this inversion.

4.2. Estimation Approach

A stylized example of the case under consideration is shown in figure 4.1. The uneven base layer is glandular tissue, while the overlying fat allows for a smooth surface. Assuming the fat and glandular tissue layers are each composed of tissue with uniform modulus, which we denote by B and L respectively, we can describe this case by the total tissue thickness, t , and a function that describes the thickness of the base layer, $d(x)$. We seek an inversion algorithm that allows us to estimate $d(x)$ from the surface pressure data collected from tactile scanning.

Tactile Scanning results in a pressure signal, P , that varies over space, x , and depends on the underlying geometry and tissue moduli (t, d, B, L). In the case under discussion, each layer will be assumed homogenous, and the geometry can be summarized as a function of the base layer thickness $d(x)$ and the constant total thickness t . With this in mind, the pressure signal, $P(x, t, d, B, L)$, can be written as $P(x)$, with $d(x)$ the only variable input quantity. The ideal estimation method would allow for immediate estimation of $d(x)$ as $P(x)$ is collected. Figure 4.2 shows the estimation scheme, with a filter estimating $d(x)$ from $P(x)$. An ideal estimation would yield an error $e(x) = 0$.

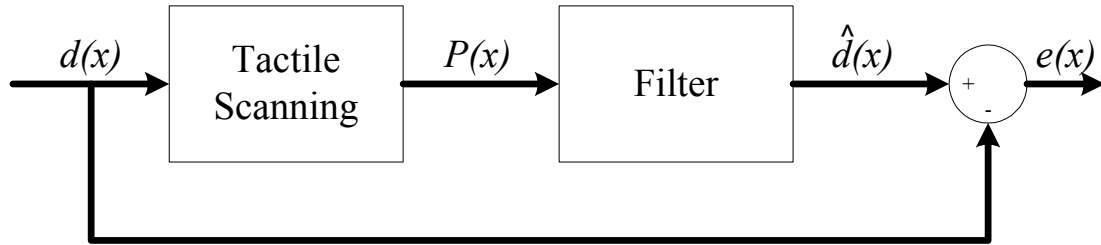


Figure 4.2. Filter representation. An ideal filter based on the impulse-response of a noise-free system would extract the input function such that the error $e(x)$ would be zero everywhere.

We propose an estimator based on the impulse response $H_P(x)$ that results from an impulse base thickness $\delta_d(x)$. The input $d(x)$ would then be related to the output $P(x)$ by

$$P(x) = H_P(x) * d(x) \quad (4.1)$$

where $*$ denotes convolution. This is the basis of the linear system, where the output $P(d_T(x))$ that results from $d_T(x) = d_1(x) + d_2(x)$ is $P(d_T(x)) = P(d_1(x)) + P(d_2(x))$. Based on our work documented in previous chapters, we expect a linear relationship between

the pressure P and a combination of base layer thickness $d(x)$ and total thickness t . In previous sections the parameter $1/(t-d)$ was used to provide the linear relationship between lesion diameter and peak pressure. In this case, however, we want a null signal when the input parameter is zero, whereas $1/(t-d)$ only approaches zero as the tissue thickness t becomes infinite. As found in Chapter 2, a linear fit between maximum pressure and $d/(t-d)$ is almost as good as the fit to $1/(t-d)$ (R^2 difference of less than 0.02). Thus, we take the nondimensional function $d/(t-d)$ as our input parameter, and look for an algorithm to estimate the function $D(x) = d(x)/(t-d(x))$ from the pressure frames collected in tactile scanning.

As in previous chapters, we turn to finite element models of the system to model tactile scanning. From the model data, we can gain an understanding of the relationship between the input parameters and the output pressure in order to generate our algorithm. In developing our estimation algorithm we will establish the linearity and practical limits of the system to help establish an understanding of the full range of the utility of using tactile imaging for the cases under consideration.

4.2.1. Pressure Output

In the proposed system, we vary only one input parameter, namely the thickness of the glandular layer, d . Changes in this one input parameter should be sufficiently captured by the variation in one output parameter, and so we consider the peaks of the pressure frames as the response to this input. The peak of the pressure profile is selected based on

the work of the previous chapters, which indicated that for a pressure profile collected over a lesion with diameter d , the peak of the profile was most directly related to d . Thus, we look at the maximum pressure $P(x)$ to try to estimate $D(x) = d(x)/(t-d(x))$.

4.3. Mechanical Modeling

The case under scrutiny here, as shown in figure 4.1 can be discretized as shown in figure 4.4, such that the function $d(x)$ becomes a discrete function of the indicial position n , $d(n)$. Discretizing the image in this way allows us to directly model this case with finite elements, where the elements at the base levels are the same size as the discretization sampling size. In keeping with the assumptions of the previous sections, we construct this case with a plain strain model. The materials are modeled as linear isotropic materials, representing fat and glandular tissue, with Young's moduli of 15kPa and 150kPa respectively, and Poisson's ratio of $\nu = 0.499$ for each. Figure 4.5 shows a typical finite element model created for this purpose.

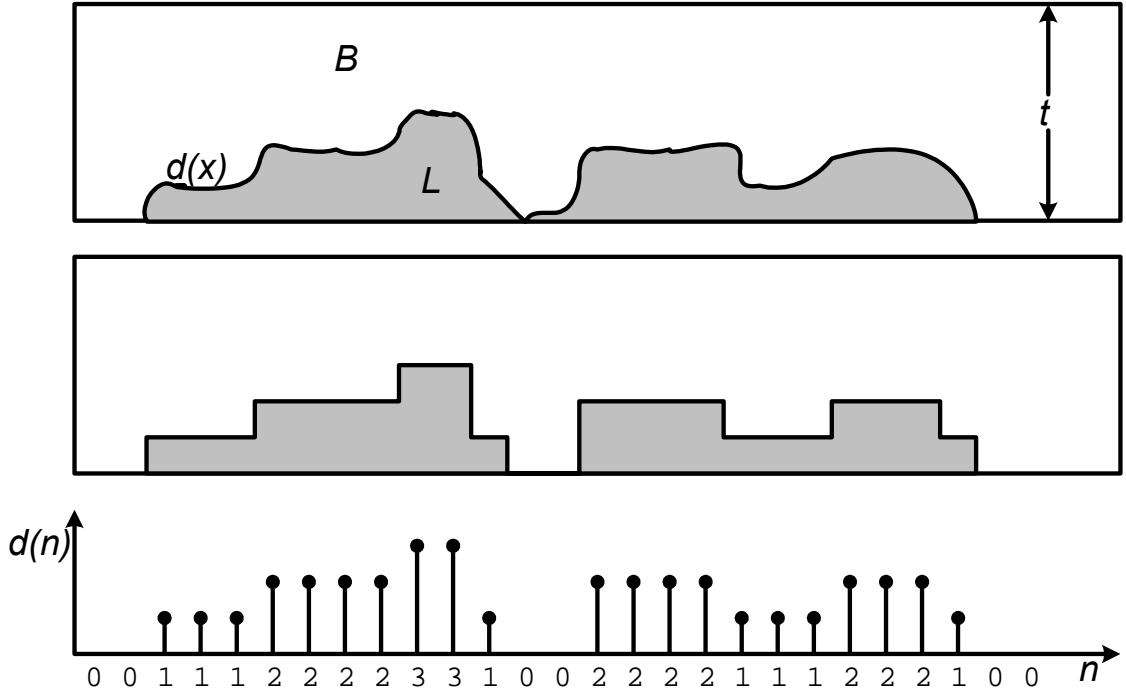


Figure 4.4. Discretizing the case of a base layer of varying thickness leads to a discrete function $d(n)$. Top: a base layer of glandular tissue with variable thickness underneath a layer of fat, with constant total thickness. This figure represents an extreme case of base layer variability. Middle: modeling the top case with discrete elements. Bottom: discrete input signal $d(n)$.

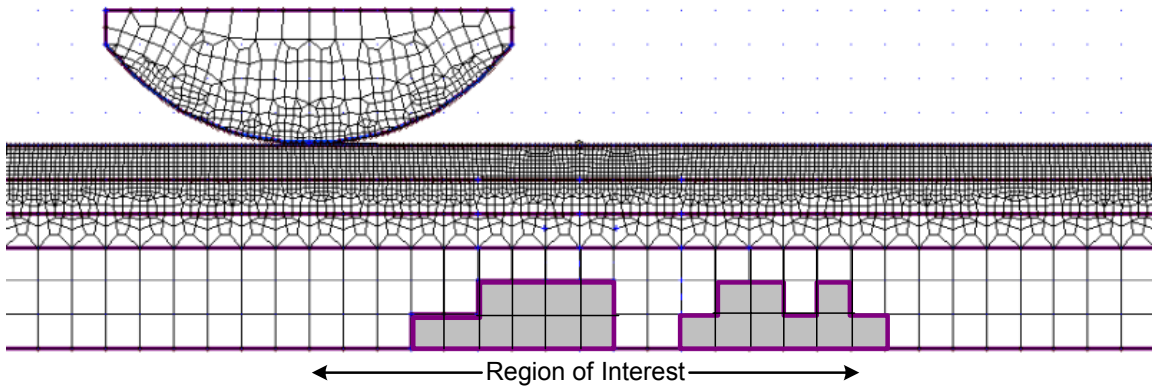


Figure 4.5. Finite element model showing a slab of tissue of uniform thickness. The tissue is made of fat, with a base layer of glandular tissue of varying thickness in the region of interest. The fat and glandular tissues are both modeled as linear elastic isotropic materials. The elements along the bottom are 0.5×0.5 cm.

The tactile imager was modeled as a cylindrical indentor as in the models of the previous sections. It was indented with a force of 80 N/m at one end of the tissue slab and slid across the surface of the tissue. Pressure frames were collected every 0.25 cm.

4.4. Linearity

We propose to develop an inversion scheme based on the impulse response $H_P(x)$ to an impulse base thickness $\delta_d(x)$. The use of an impulse response is based on the assumption that the system can be modeled linearly. In order to test the linearity principle, five models (one master and four sub-models) were constructed as shown in figure 4.6. In these models, the total tissue thickness, t , is 3 cm, while the glandular layer varies from 0 to 1 cm thick. The models were constructed so that various combinations of the sub-models should result in a pressure profile like that of the master model if linearity holds for our system. We model a flat area of constant $D(x)$, a gap between two lumps, and a lump with a step difference in $D(x)$. From figure 4.6 we expect the following relationships for the pressure profiles:

$$\begin{aligned} P_T &= P_a + P_b \\ P_T &= P_a + P_c + P_d \end{aligned} \tag{4.2}$$

This assumes a zero pressure frame when there is no glandular tissue beneath the fat, which is not the case. This can be accounted for, however, by subtracting a standard

background pressure distribution from each pressure frame. This background value is the pressure frame that would be recorded on tissue of the same thickness as the sample but composed entirely of fat, *i.e.* $D = 0$.

Testing linearity on these models will not provide an exhaustive proof of the linearity of our system. However, it will allow us to study the limits of linearity at superposition with a gap and without. We expect this to be representative of the most extreme case encountered clinically, that of a perimenopausal breast undergoing discrete glandular involution.

With the background value subtracted, the superposition of the relationships in equation 4.2 above is shown in figure 4.7. Figure 4.7 shows the peaks of the pressure frames collected every 0.25 cm for the 8 cm of the models shown in figure 4.6. A plot of the peaks is essentially a plot along the curve that follows the highest contour of the composite tactile image for each model. As expected, the peaks of the pressure frames indeed show the greatest relative signal amplitude, compared with other quantities that we can extract from the pressure frames, such as the width or edge slope of the frames.

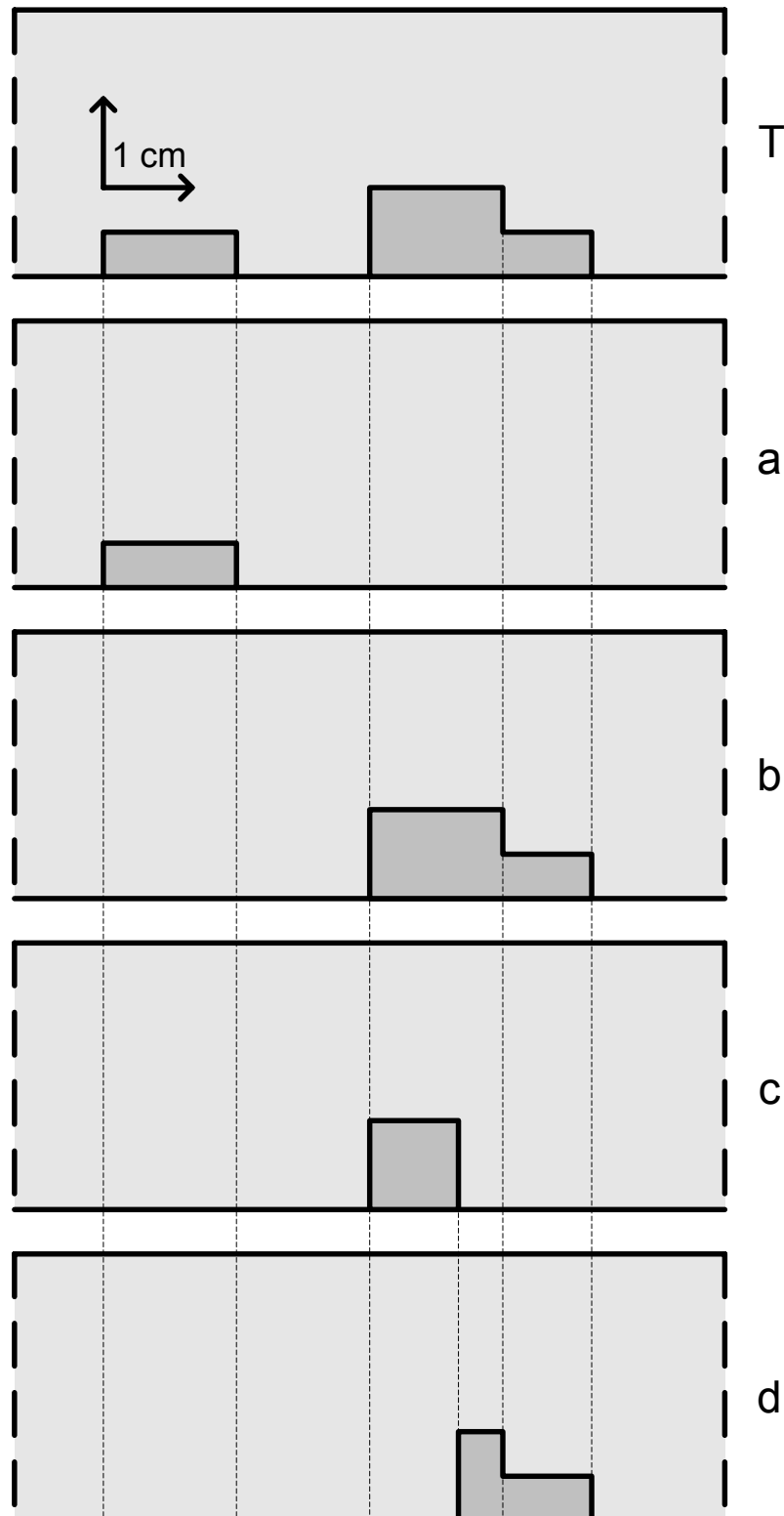


Figure 4.6. Five models were created such that the principle of superposition can be tested. Neglecting the background modulus, various combinations of the lower four models can be superposed to create the same glandular tissue layer as the top model. Specifically, $T = a + b = a + c + d$.

The superposed pressure functions exhibit a similar shape to that resulting from the total input in both cases. The case of $P_a + P_b = P_T$ is accurate to within 5% mean absolute difference. The second case, of $P_a + P_c + P_d = P_T$ has mean absolute difference of 36%. This is partly due to the noise at the tails of the profile, which introduces a higher relative error. Aside from the noisy tails, the maximum difference is 48% of the signal and occurs at the maximum value of the superposition.

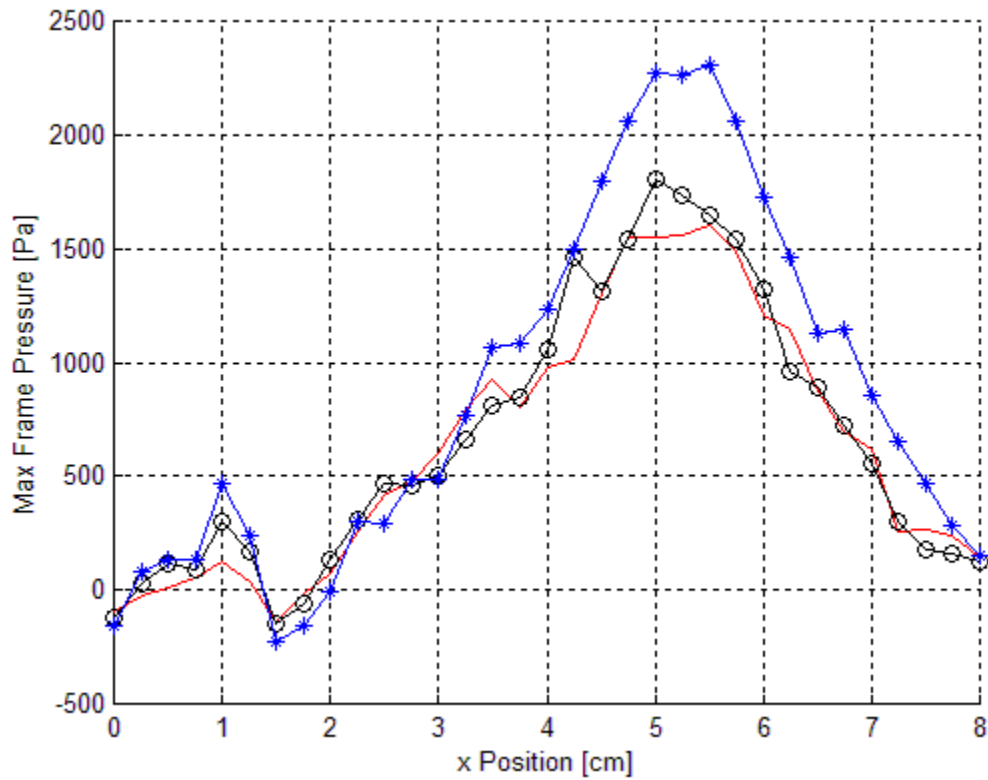


Figure 4.7. Result of superposing the peak pressure (less the background) for the tactile information from the models shown in figure 4.6. Solid (red) = P_T , Circles (black) = $P_a + P_b$, Stars (blue) = $P_a + P_c + P_d$.

The errors in the superposition of the second case are mainly due to the overshoot in the pressure profile for the larger section of glandular tissue on the right. In this case this section was superposed by two adjacent pieces, so the smearing of the underlying information inherent in tactile imaging due to the overlying layer of soft tissue cause overlapping pressure information at the edges of stiff lumps. The general shape of the pressure profiles, however, is correct. This indicates that superposition of the underlying glandular layer does not create spurious data, such as a singular peak in the pressure profile that would otherwise result only from a spike in $D(x)$. This, then, shows a limit to the estimation of $D(x)$ from $P(x)$, in that $P(x)$ may overestimate $D(x)$ in the presence of dense superposition. Since the underlying shape of the pressure profile is correct, however, we move ahead to developing the appropriate impulse response.

4.5. Algorithm Development

The first step in developing the inversion technique is establishing the impulse response which is the basis of signal superposition of the system. With the impulse response established, we surmise that the relationship between the input and output is a convolution of the input with the impulse response. Thus, to estimate the input signal using the output, we must deconvolve the output pressure signal with the impulse response.

Given the discretization shown in figure 4.4, the basic impulse input is shown in figure 4.8. In discrete systems such as this, the proper impulse is one sampling interval long and one unit high. We model this as a singular element of glandular tissue at the base of a model composed entirely of fat. This results in a rectangular impulse input of glandular tissue 0.5 cm wide and 0.5 cm high.

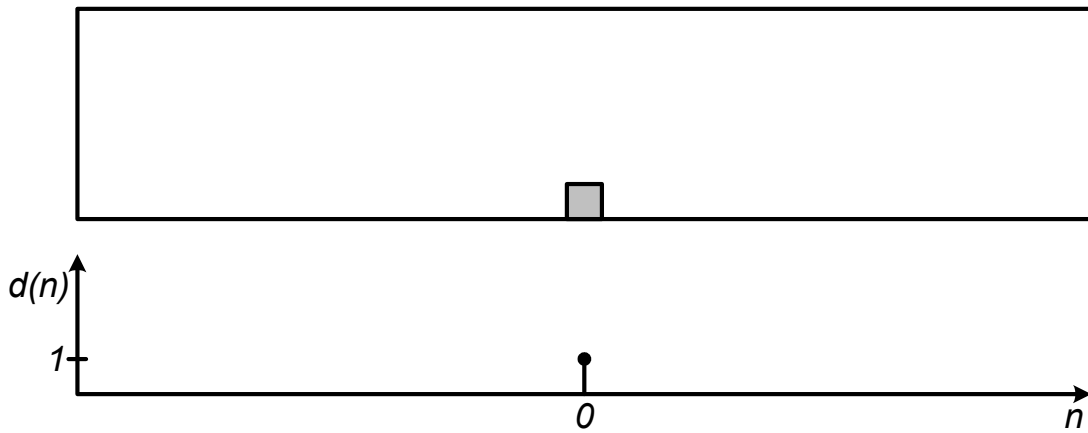


Figure 4.8. Impulse input $\delta_d(n)$ for the discretization scheme shown in figure 4.4.

The ideal discrete impulse input, however, is too small to create a distinctive pressure signal in most models of physiological thickness, so we turn to modeling the impulse input by a glandular impulse one element wide and two elements high (0.5 cm wide and 1.0 cm high). The response to this modified impulse input for tissue thickness $t = 3$ cm is shown in figure 4.9 (leftmost plot). The response to this 1cm high impulse is well-modeled by a gaussian function with a peak of 195 Pa and a standard deviation of 0.92 cm (standard deviation in the indicial value $n = 3.7$). In order to test whether our modification of the unit impulse, based on the principle of superposition, was acceptable,

we also model impulses three and four times as high as the true impulse (1.5 and 2.0 cm respectively). The resulting pressure responses and gaussian fits are shown in figure 4.9.

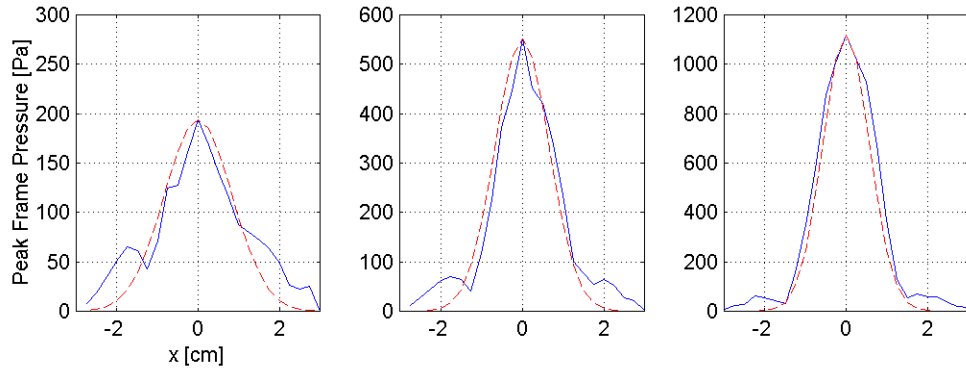


Figure 4.9. Peak Pressure Profile for impulses of different heights in background tissue 3cm thick. The actual data is shown in solid blue, with a gaussian fit superposed in a dashed red line. From left to right, the impulse height was 1cm, 1.5cm, and 2cm. The standard deviations for the three gaussians are 1.18, 0.95, and 0.82 cm respectively. The standard deviation for the first case is higher due to the contribution of the tails in the data, whose absolute magnitude does not change for each of the impulse responses.

The pressure responses to the impulse inputs of varying heights are shown in figure 4.9. The standard deviations of the best fit gaussian curves were 0.95 ± 0.1 cm (0.1 cm standard deviation). Although this shows a 10% variation, we will consider the central value as representative of the cases we expect in patients. This allows us to extrapolate the height of the gaussian to the theoretical response of the true impulse input. Figure 4.10 shows the heights of the impulse responses to impulse inputs of varying heights in tissue 3 cm thick, versus the function $D = d/(t-d)$. As expected, the relationship between D and the peak of the pressure response to an impulse input is well modeled as linear ($R^2 = 0.98$). Combining the result from this gaussian peak fitting with the average variance

of 0.975cm found for the responses to the impulses of varying height yields an impulse response of

$$H_p(x) = 575e^{(-x^2/1.9)} \quad (4.3)$$

for $t = 3\text{cm}$.

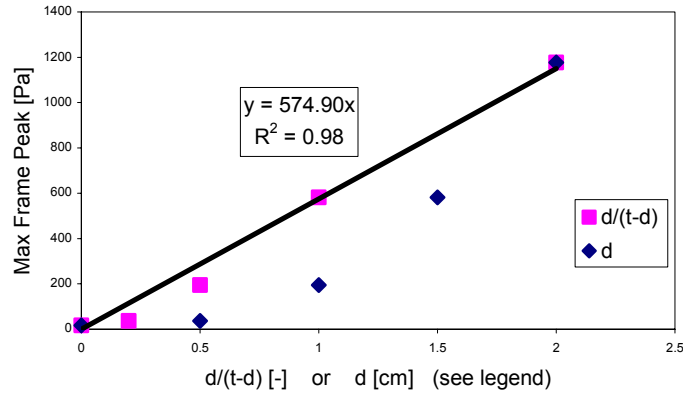


Figure 4.10. Thickness of glandular layer, d , and linearized thickness $D = d/(t-d)$ versus the magnitude of a gaussian fit to the pressure frame peaks for tissue thickness $t = 3\text{ cm}$. The linear fit to the $d/(t-d)$ data is shown, and as expected it fits the data well.

Similar analysis for models of varying thickness yields similar impulse responses, a sampling of which is shown in figure 4.11. The variance for gaussians fit to these impulse responses does not change appreciably over the range of tissue thickness of interest, giving a standard deviation of $0.94 \pm 0.2\text{ cm}$ for 7 models with total tissue thickness t increasing 0.5 cm in the range of {2.0 cm, 5.0 cm}. The lower variation in these standard deviations is partly due to testing impulses greater than 1.0 cm high, such that the errors introduced by the noisy tails is minimized.

Figure 4.12 shows the height of all impulse responses studied for 14 models in this range of tissue thickness and impulse heights between 1 cm and 3.5 cm. The data can be fit to a linear relationship to $d/(t-d)$ with moderate errors ($R^2 = 0.77$). Combining this result with

the variance data above, we can generate a generic impulse response valid for all tissue thicknesses of interest and with background modulus at the physiological human breast fat modulus of 15kPa. This impulse response is

$$H_p(x) = 398e^{(-x^2/1.8)}. \quad (4.4)$$

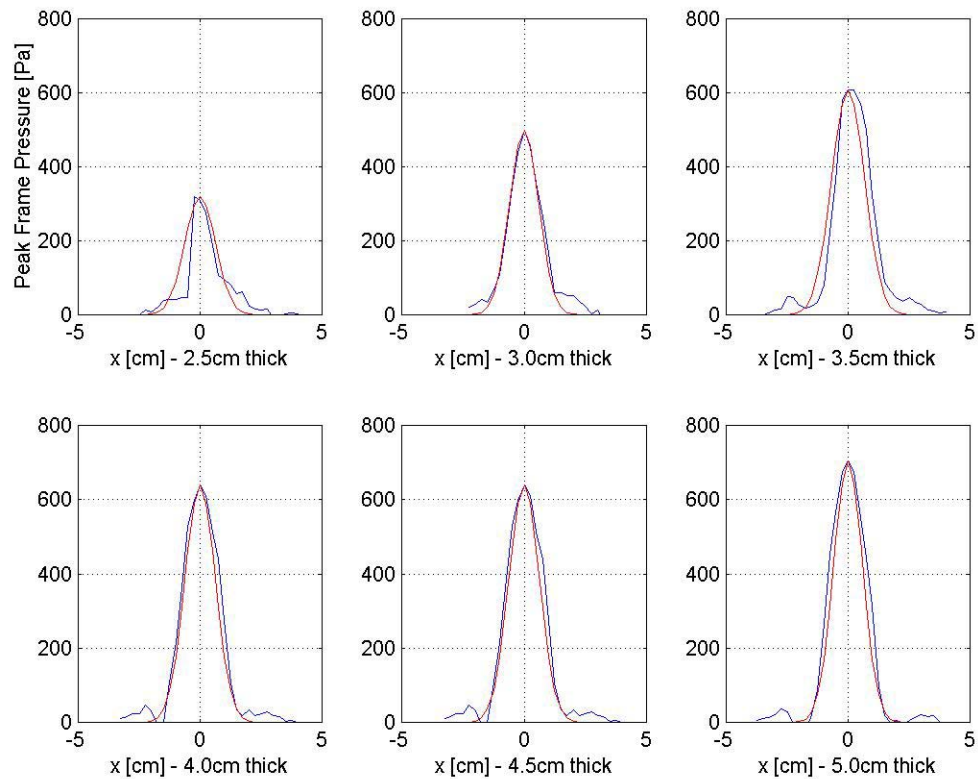


Figure 4.11. Impulse responses for tissues of varying thickness. The impulses had height d that was 1.5cm less than the model thickness. The standard deviations of the impulse responses for models of increasing thickness are 0.95, 0.92, 0.97, 0.94, 0.94, 0.92 cm respectively.

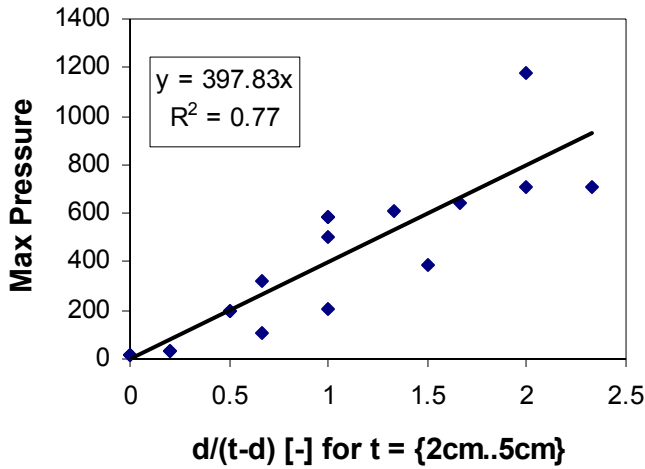


Figure 4.12. Impulse response height versus linearized base thickness. The data can be fit to a straight line with moderate error.

The impulse response generated (equation 4.4) is valid across the range of tissue thickness $2.0 \text{ cm} \leq t \leq 5.0 \text{ cm}$ and impulse height $0.5 \text{ cm} \leq d \leq 3.5 \text{ cm}$, though for each specific combination of d and t the ideal impulse response is slightly different from that of equation 4.4. This will be the cause of error in parameter estimation, however the errors are minimized as much as possible in the range of interest. Practically, if one had an independent means of calculating the total tissue thickness t (for example, from a compatible device such as an ultrasound transducer), a more accurate impulse response can be applied, tailored to the specific tissue under study.

4.5.1. Estimating the Glandular Tissue Thickness

With the impulse response $H_P(x)$ and the output signal $P(x)$, the input $D(x) = d(x)/(t-d(x))$ can be calculated by deconvolving $H_P(x)$ and $P(x)$. There are several established methods for performing a deconvolution. In our case we choose a matrix deconvolution method,

as it is more robust than time-domain (polynomial division) deconvolution and frequency domain (spectral division) deconvolution, given the noise in our signal $P(x)$ [Hansen 98].

Matrix deconvolution requires that a matrix Γ be constructed such that its rows are the convolution of the rows of an identity matrix \mathbf{I} with the impulse response H_P , such that for each row i of Γ ,

$$\Gamma_i = \mathbf{I}_i * H_P^T$$

where the transpose of the impulse response is taken since it is assumed to be contained in a row vector.

Once the matrix Γ has been established, the deconvolution of the signal P and the impulse response H becomes

$$D_{est} = [\Gamma^T \Gamma + \lambda \mathbf{I}]^{-1} \Gamma^T P$$

where \mathbf{I} is the identity matrix and λ is a regularization parameter.

If the signal $P(x)$ was free of noise, the regularization parameter λ should be set to zero. In our case, the system is not noise-free, so λ was nonzero. In order to determine an appropriate value for λ , we created 12 finite element models with varying $D(x)$ and obtained their attendant $P(x)$. The λ for each of these models is that which minimizes the error

$$e(D_{est}) = \sum_n (D_{est} - D)^2.$$

The λ thus found was $1.5 \times 10^4 \pm 8.6 \times 10^3$ across the test models. For a few models, the error did not minimize for increasing λ , however a plateau was reached by $\lambda = 10^4$

beyond which the error did not decrease by more than 10%. For these models, λ was assumed to be equal to 10^4 . In light of the average regularization parameter, $\lambda = 1.5 \times 10^4$ was used for all the models tested. A smaller λ will allow noise in the pressure signal to have a larger contribution to the reconstructed signal, however a larger λ should be avoided, as that would result in increased smearing of the data.

4.6. Effect of the Background Modulus

In the previous section we found that the impulse response width does not vary greatly over the tissue thickness range of interest. The only other background parameter than can affect the width of the impulse response is the background modulus. The background modulus range is not very large, since fat modulus is fairly consistent among subjects [Wellman 99]. Nonetheless, for an impulse composed of glandular tissue at the physiologic value of 150kPa, varying the background modulus yielded the changes in standard deviation shown in figure 4.13 (lower curve). Due to the low modulus of the impulse, it is not possible to run models beyond the small range of the curve shown in figure 4.13: higher background modulus would be indiscernible from the underlying glandular layer, while the finite element models do not converge for lower values of background modulus. To avoid this problem, we increased the modulus of the impulse tenfold to 1.5 MPa and analyzed models with this higher Young's Modulus for the base layer in order to study the effect on the width of the impulse response. This is shown in the upper curve of figure 4.13. The shape of the dependency between the width of the

impulse response and the underlying background modulus remains approximately the same for the two cases studied.

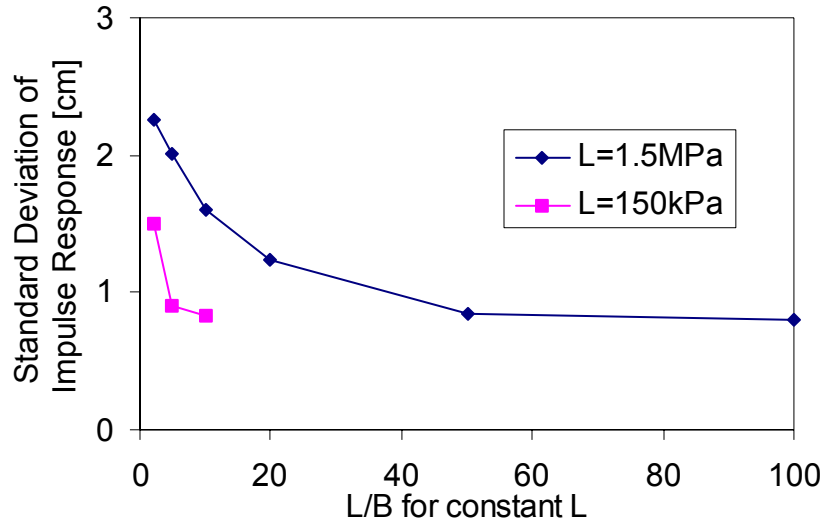


Figure 4.13. Change in width of impulse response with changing tissue modulus. B is the modulus of the background (fat) tissue, while L is the modulus of the glandular tissue layer.

The approximate mean physiological ratio of background fat modulus to glandular tissue modulus is between 1:3 and 1:10. The width of the impulse response increases for increasing background modulus around this physiological value. Once again, therefore, we see that the impulse response needed should be tailored to the specific parameters of the tissue under study. The actual modulus of human breast fat, however, is more predictable than that of other breast tissues [Wellman 99] and so a varying background modulus B should not be a large source of error.

4.7. System Resolution

Since the pressure response is discretely sampled from signals that are not noise-free, we expect that our system will be unable to distinguish features smaller than a particular resolution limit. In order to study the actual resolution of the system, we created models with two underlying impulses of glandular tissue. A schematic of the result from these models is shown in figure 4.14. The trough in the deconvolved signal between the two impulses increases as the impulses get closer together. Plots of the height of this trough normalized to the average height of the peaks are shown in figure 4.15. The reconstructed signal shows almost no trough for an impulse separation of less than 1cm. At maximum separation a plateau is reached where the trough does not reduce further. This trough is reached by the time the separation equals 2 cm, or 2 standard deviations of the impulse response with overlying fat modulus in the physiological range, and gives us a quantitative measure of the expected resolution of the system.

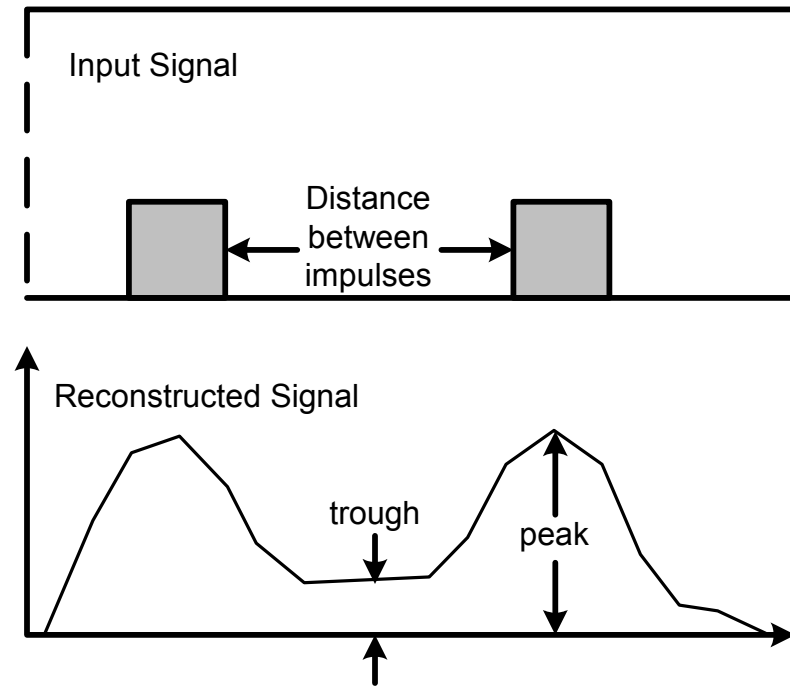


Figure 4.14. Model with two impulses created and reconstructed signal. The reconstructed signal is from a model with tissue thickness $t = 4.0$ cm and distance between impulses of 3.5 cm.

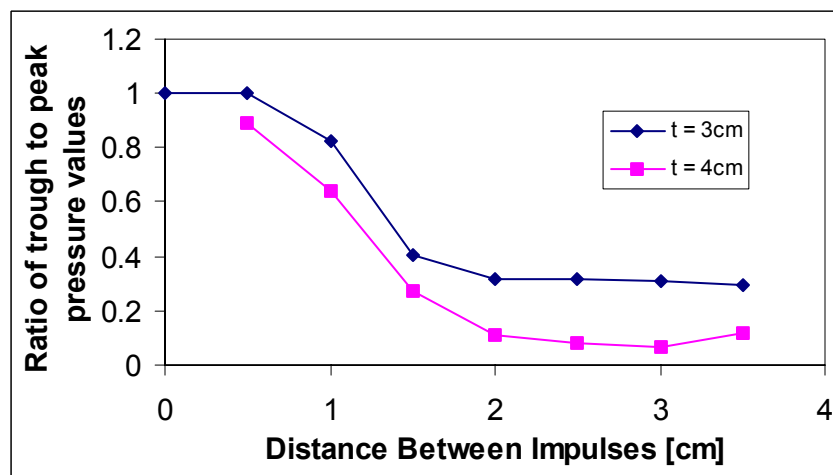


Figure 4.15. System resolution. The peaks become clearly discernable as resulting from two distinct regions at a distance greater than 1.5cm, and the trough settles into its minimum value at 2cm, which is twice the standard deviation of the gaussian impulse response.

4.8. Results and Discussion

The impulse response of equation 4.4 developed in the previous section was used to estimate the underlying base layer thickness from the resulting peak pressure profiles collected from tactile scanning on various finite element models. After subtracting the background pressure, matrix deconvolution was employed to deconvolve the actual signal from the impulse response. This method is fast enough to be applied to real time data collection.

A typical result is shown in figure 4.16. In general, for input signals that contained features greater than 1cm wide, the reconstructed signal showed a mean absolute error of less than 20% in estimating the input parameter $d/(t-d)$. The reconstruction of input signals with features smaller than this is far poorer, with errors greater than 30% of the signal. A typical example is shown in figure 4.17, and as expected, a great part of the error stems from the narrow gap in the glandular tissue. The reconstructed signal not only smoothes the two lumps, it also estimates that the first lump does not start for almost a centimeter after its actual rise. This may be due to the proximity of the large lump to the small lump – since the tactile imager scanhead is wider than the distance between the lumps, the larger lump can be ‘supporting’ the scanhead as it approaches and moves over the smaller lump, and essentially shielding the smaller lump from the stresses that would result in a distinctive pressure signature. Since the lumps are only 1 cm apart, the result shown in figure 4.17 fits well with the expected signal loss of the resolution study shown in figure 4.15.

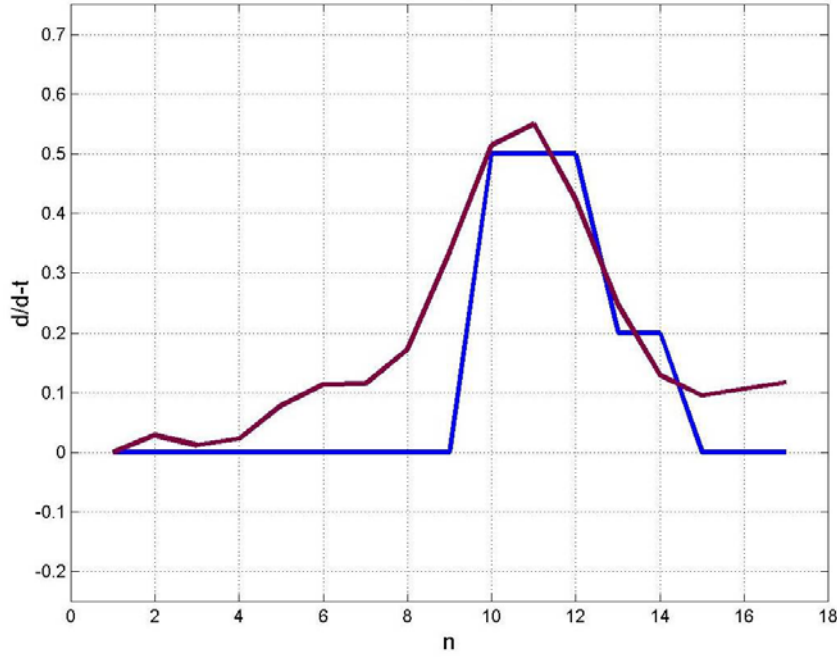


Figure 4.16. Reconstruction (purple) of the original signal (blue) shows good tracking. The small plateau on the right in the original signal manifests as a shallower slope on the right than on the left. The index n corresponds to tactile scanning intervals of $x = 0.5\text{cm}$.

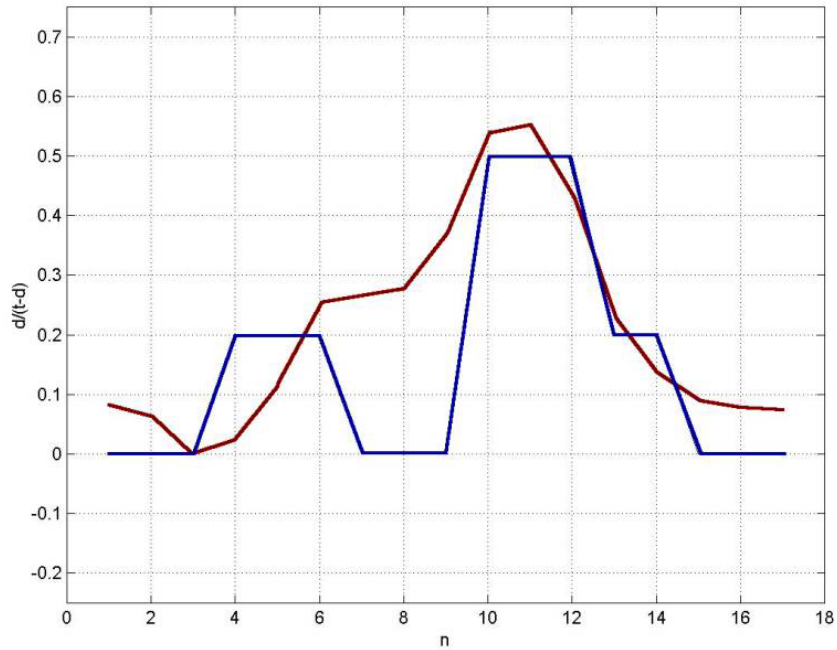


Figure 4.17. Reconstruction (purple) of the original signal (blue) using the impulse response of equation 4.4. Lumps with a 1cm separation are not distinguishable as discrete. The index n corresponds to tactile scanning intervals of $x = 0.5\text{cm}$.

4.9. Discussion and Future Work

Tactile imaging is inherently a nonlinear process, with a resultant pressure profile that depends in a complex way on the underlying tissue parameters. In this chapter we have modeled the relationship between the maximum frame pressure and a linearized glandular tissue thickness as linear, and applied a deconvolution algorithm to estimate the tissue thickness from the pressure data. Limits to the estimation of the tissue thickness are reached for features narrower than 1 cm that cannot be detected with this method. Limits to the quality of estimation are seen if the imaged tissue parameters do not fall into the range of study. For example, if the background modulus was much higher than 15 kPa, the resolution would be even worse. Although the impulse response developed minimizes the error of applying a linear system to the physiological range of interest, tissue with parameters at the extremes of this range will show a larger error than tissue with parameters at the median of the range.

The analysis presented in this chapter was all for two-dimensional plain strain models with linear elastic materials. Further analysis would explore three-dimensional models, both finite element and physical. The problem of nonlinear material properties and the effect of the scanhead shape on the resolution should also be explored.

Physical tissue is nonlinear [Wellman 99] and strain hardening. Applying our linear algorithm to real tissue will introduce errors based on the tissue moduli increasing with applied pressure. Specifically, as the tissue is compressed, the effective modulus

increases, and based on the analysis of chapter 2, we expect that this will result in an underestimation of the tissue layer thickness.

Since a scanhead with a smaller radius of curvature can be indented further into tissue, and record pressures at greater angles due to its curvature, one may surmise that the resolution along the depth of the scanhead, the direction not studied here, would be worse than that found in this study. The relationship between scanhead radius and resolution, along with other tradeoffs associated with the scanhead shape, may prove to be an interesting result that can make this system more valuable for clinical use.

Chapter 5

Mammography Registered Tactile Imaging

5.1. Introduction

Mammography is the gold standard in screening for breast pathologies. It records the radioopacity of breast tissue, and results in a complicated image which radiologists learn to interpret mainly by experience [Jatoi 97] to detect suspicious areas. Manual palpation, in the form of the Clinical Breast Exam (CBE), is an established adjunct to the screening process [Kopans 00, ACS 03], since many diseases of the breast, including cancer, manifest as a change in tissue stiffness [Ronnov-Jessen 96]. The complete picture of breast cancer screening includes both palpation and mammography, and doctors are advised that “screening for breast cancer is best done by including both mammography and clinical breast examination in the screening process” [US 94].

Tactile information, such as position of a localized stiffness, is useful in mammographic evaluation, as the area of the stiffness is even more carefully scrutinized. However, since CBEs rely on a qualitative assessment of the palpable extent of breast tissue and are

performed by a clinician different than the radiologist, the information from the CBE is often not used in conjunction with the mammogram.

Mammography and tactile imaging, in their basic physics, are based on two different phenomena (radiological density vs. mechanical stiffness). Because of this underlying difference, lesions may show up well only in one modality rather than both: a palpable lump might not have a radiographic signature different than the background tissue, and similarly, a radiographically opaque lump can be nonpalpable. In most cases, however, pathologies are at least marginally visible in both modalities, and so when one imaging modality picks up the signal of an underlying pathology, one may find evidence of the pathology present in the other modality with greater scrutiny. These two imaging modalities, mammography and palpation, therefore, can serve to reinforce one another. This is the basic premise of the current breast cancer screening protocol, which calls for both mammographic and tactile information.

5.1.1. Motivation

Tactile imaging quantifies palpation [Wellman 01], and is an imaging modality that can be performed at the same time and in the same plane as a mammogram. It is our supposition that tactile imaging can be seamlessly incorporated into the breast cancer screening protocol and improve the success of breast cancer screening.

Establishing tactile imaging as a valuable adjunct to screening mammography will require an increase in the positive predictive value ($PPV = \frac{TruePositives}{AllPositives}$) for regular screening visits. This rests on the hypothesis that the information on lesions and other irregularities in breast stiffness that is contained in a tactile image will enhance radiologists' ability to detect malignancies in mammograms. While mammography and tactile imaging are based on distinct physical phenomena, many masses are at least marginally visible in both modalities. Features in the tactile image will thus indicate areas for heightened scrutiny by the radiologist reading the film. This promises to increase the sensitivity of mammography, and because tactile imaging is a non-invasive imaging technique that can be quickly and easily performed by mammography technicians, patient compliance will be high and incremental costs will be small.

5.1.2. Chapter Layout

It is our supposition that the information from the tactile imager can add value to breast cancer screening as it is performed today. An important first step in establishing and realizing this utility is spatially registering the tactile images to mammograms, so that the information in the tactile image is displayed in parallel to that in the mammogram. Tactile images of the breast are generally collected with the woman laying supine [figure 5.1], while mammograms are obtained with the woman standing and her breast resting on a mammography plate [figure 5.2]. Even if the tactile image was obtained in the same plane as a mammogram, however, the breast tissue is compressed differently in the two modalities, and so registration is not readily performed.

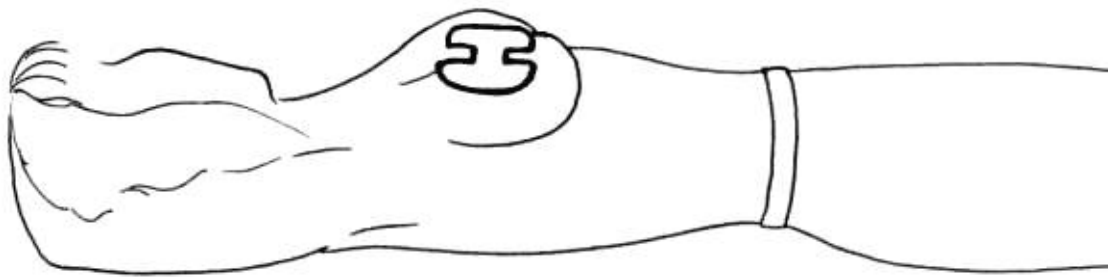


Figure 5.1. Obtaining a tactile image. With tactile imaging technology currently in clinical use, the woman lays supine while the tactile imager is gently pressed into the breast tissue. A tactile map is collected by moving the tactile imager across the breast tissue in multiple strokes. Ultrasound images of the breast are also collected in this manner.

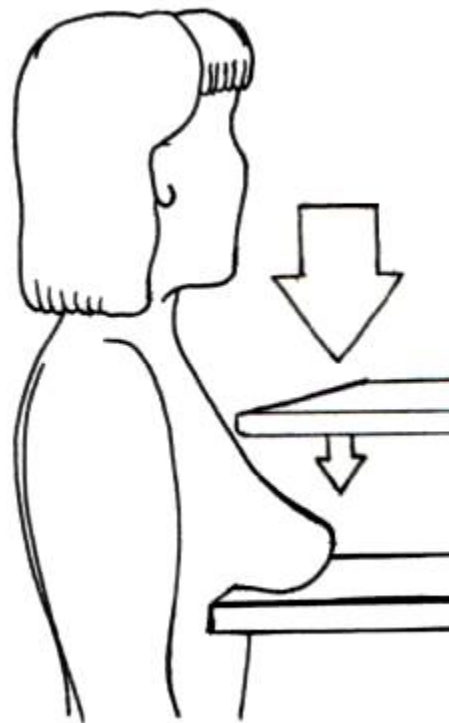


Figure 5.2. Obtaining a cranio-caudal mammogram. The breast is rested on the rigid bottom plate and compressed by the top plate in the direction of the small arrow. X-rays pass through the breast in the direction of the large arrow and expose film stored in the bottom plate. In this way, a vertical projection of the radioopacity of breast tissue is obtained.

Registration of the tactile image and the mammogram requires an understanding of the relative motion of the breast incurred in each imaging modality. The mammogram is obtained with the breast compressed between two parallel plates for the greatest compression and spreading the patient can tolerate. In contrast, the tactile image is obtained by indenting the breast with a small scanhead stroked over the surface of the breast. The breast is stretched as the tactile image is obtained, but due to the lower compression and the small area of contact the total deformation under tactile imaging is different from and less than that under mammography. The difference in the deformation of the breast tissue as the tissue is imaged under each modality must be accounted for in order for registration to occur.

In this chapter we develop an algorithm to account for the difference in deformation inherent between cranio-caudal mammography and tactile imaging performed with the woman standing, and apply it to preliminary clinical data. We first discuss mechanical modeling of the deformation fields of the two imaging modalities. Three dimensional finite element models of breasts of various sizes are built and compressed under the two modalities in order to obtain representative deformation fields under each type of compression. A transformation algorithm is developed to register the modeled tactile imaging deformation to the mammographic deformation. A physical breast model is constructed which can be subjected to tactile imaging and mammographic compression. Results of applying the transformation algorithm to the physical model data are presented. Finally, we present a preliminary evaluation of the registration applied to clinically collected mammograms and tactile images.

5.1.3. Further Clinical Application

The work presented in this chapter can be applied to imaging modalities beyond tactile imaging and mammography. Specifically, other imaging modalities that are currently being tested for their utility to breast cancer screening and diagnosis include ultrasonography [ACS 03], magnetic resonance (MR) imaging [Maier 98], and diffuse optical tomography [Durduran 02]. Ultrasound images are obtained in a manner similar to tactile images, with a small scanhead stroked on the surface of the breast. Although the data obtained is in slices perpendicular to the surface of the breast, the data can be localized on the surface of the breast in the same way as tactile data, and so can be registered to mammograms using the algorithm developed in this work. Both MR imaging and diffuse optical tomography are obtained with the breast in compression between parallel plates [figure 5.3], and so this work allows for images such as tactile maps and ultrasonograms to be registered to them.

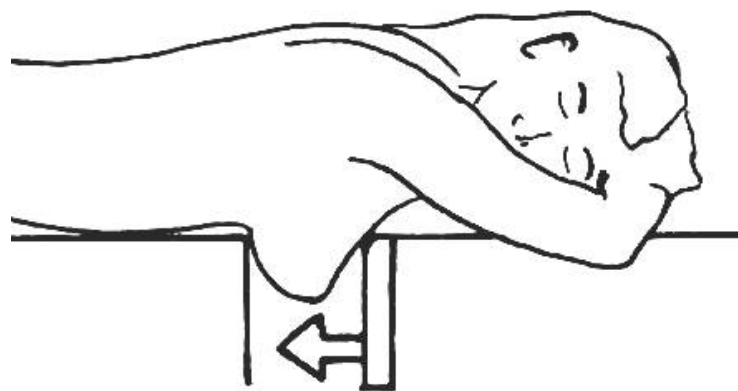


Figure 5.3. Modality of imaging for MRI and optical tomography of the breast. In both modalities, the breast is compressed by moving the plate above the breast in the direction indicated.

5.1.4. Previous Work

The general problem of organ image registration has been studied by various researchers [Meyer 99, Reuckert 99, Krucker 00]. Most of these studies dealt with the registration of images from the same image modality, where large relative deformations were not expected. A few studies have focused on the registration of images between different modalities [Wells 96], however these multi-modal approaches relied on registering images based on their content. In our case, since we seek to show that tactile images and mammograms can be correlated, using the information contained in each image to register it to the other would require assuming the outcome we wish to prove. Since we seek a registration algorithm that can show the relationship between tactile imaging and mammography we turn to understanding the differences in the tissue deformation under the two modalities in order to develop our registration algorithm.

The motion of specific areas of the breast under parallel plate compression has been studied most notably by Azar et al [01]. In their study, coarse finite element models were created and deformed between parallel plates in order to track the relative motion of a lesion for biopsy. Their method had to be applied while the patient's breast was in compression, and so a fast algorithm was of the essence. The coarse meshing they used was solvable in about 10 minutes.

We will follow their example and use finite element models to develop an understanding of the deformations incurred under tactile imaging and mammography. Since our finite element models will be used only to develop a library of deformation fields which we can study in order to develop a registration algorithm, we do not have the solving time constraints as in this earlier study. We can therefore afford smaller elements to obtain a more detailed deformation field, which we can use to devise a registration algorithm applicable to a range of breast shapes and sizes.

5.2. Mechanical Modeling

5.2.1. Model-based Approach

The first step in registering tactile images to mammograms is to develop an understanding of the deformation of breast tissue under mammographic and tactile imaging compression. As detailed in the previous section, finite element models have been used in previous studies for tracking the deformation of small volumes in a breast under compression [Azar 01] with satisfactory clinical validation, even for models with only a few large elements. We therefore follow this example to generate finite element models that will provide insight into a range of clinical cases. These models will be compressed with modeled mammographic and tactile imaging compressions, and the resulting deformations studied as a basis to developing a registration algorithm.

The following sections detail the finite element model development and deformation results. From the model results, we develop a registration algorithm that is in turn applied to the deformation data from each model to register points in the breast deformed under tactile imaging compression to their corresponding points under mammographic compression. The results of this model registration are presented, and some merits and limitations of this algorithm are discussed.

5.2.2. Finite Element Model Development

The shape of the natural human breast varies considerably from woman to woman, but some generalities may be drawn based on the volume of breast tissue. Breast contours are in general defined by the mass and composition of the glandular and fatty tissue, the amount and elasticity of the enveloping skin, and the elasticity of the interlaced fibrous tissue. Despite these many variables, the underlying biology varies within limited ranges, and so generalities may be drawn about breast shapes for breasts of various masses. For example, in a natural human breast (of a non-pregnant woman) the proportion of fat to glandular tissue increases as breast mass increases. The amount and elasticity of the fibrous tissues, however, does not increase proportionally with mass, and the supporting area of the chest wall is relatively fixed from the 3rd to the 6th or 7th rib [Gray 01]. These conditions taken together make it so that a large breast placed on a horizontal surface (such as the bottom plate of a mammography machine) tends to extend further horizontally than it does vertically compared with a smaller breast.

In light of the above discussion that breast volume is the greatest determinant of breast shape, three representative subjects (healthy female volunteers) were analyzed that spanned the range of breast size and thus shape in order to characterize realistic shapes for breast models for this study. The size and shape are indicated in table 5.1. Breast contours of each subject's breasts were measured with each breast resting on a horizontal plate. Curves of the front and side profiles of the left and right breast were generated by tracing the outline of the breast as viewed through a vertical plexiglass sheet positioned at the edge of the breast. Figure 5.4 shows the three models created by fitting splines to the contour information from the three subjects. The average contours of the left and right breast were used, generating models symmetric about the vertical center plane. The chest wall is assumed to be 1cm beyond the skin surface of the chest.

Table 5.1. Size and shape of the models used to span the range of interest.

Subject Breast Size Label	Extent of Breast From Skin of Chest Wall	Width of Breast Along chest Wall	US Brassiere Cup Size
Small	5.8 cm	12.3 cm	A
Medium	9.6 cm	15.8 cm	C
Large	11.9 cm	18.7 cm	DD

The breasts were modeled as fat-replaced postmenopausal breasts, since most cases of breast cancer occur post menopause. The fat was modeled as a linear elastic isotropic material of 15kPa modulus, congruent with tissue property measurements found in literature [Wellman 99, Krouskop 02]. Finite element models were created and meshed in Femap v8.0 (EDS Inc.) and solved using Abaqus Standard 6.2-5 (HKS Inc.) with nonlinear geometry formulation. The models were composed of between 1000 and 1500 tetrahedral elements (the greater number for the larger model) with the largest element

extent less than 8mm. The mammography plate was modeled as a rigid horizontal plate with a 1.5cm radius of curvature along the bottom edge closest to the chest wall, corresponding to the plates seen clinically. The tactile imager was modeled as a long cylinder of 3.8cm radius spanning the width of the breast. It was indented into the breast at five positions away from the chest wall. The full compression field from the tactile imager was interpolated between the results for each position. The contact boundaries between the breast and the plates and tactile imager were non-slip. The breast tissue was fixed to the chest wall, and the boundary through the nipple was defined as symmetric.

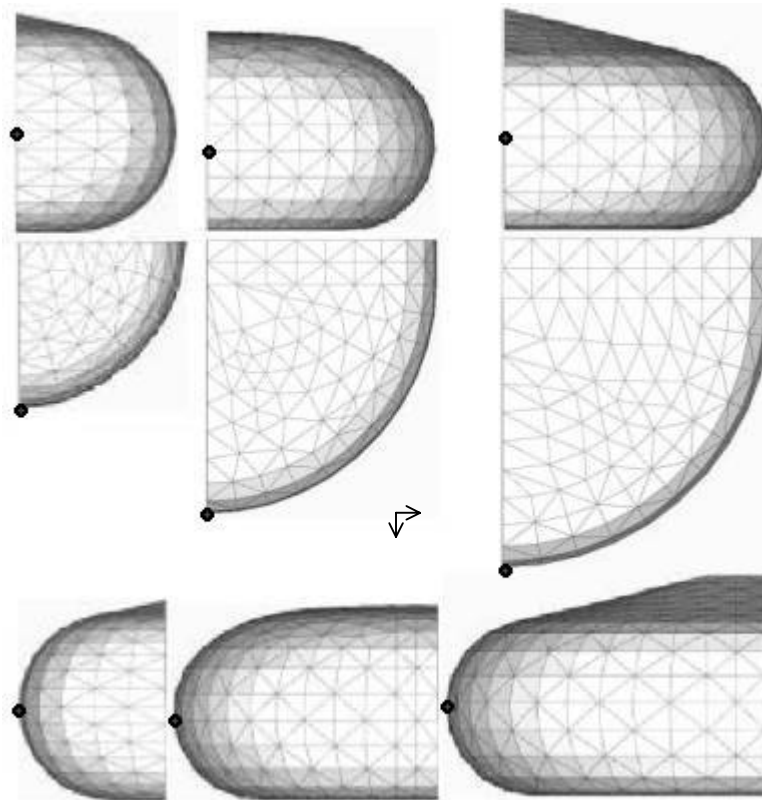


Figure 5.4. Finite element models of the small, medium and large breasts created for this study. Only one half of each breast is modeled, and symmetry is assumed around the vertical midline. In this way, each model is an average of both sides of both the left and right breast of one subject. From the top down are shown the front, top, and side views. The position of the nipple is indicated in each view by a black dot. The arrows indicate a 1cm extent in the x and y directions

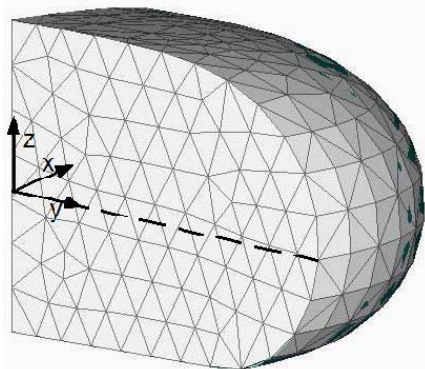


Figure 5.5. Cartesian coordinates used for model and data analysis, shown on the medium model. The flat back of each model, corresponding to the rigid chest wall, is at $y = -1$ cm, so that the back edge of the mammography plate used clinically is at $y = 0$. The midline, which connects the chest wall to the nipple along the y axis, is shown as a dashed line

In order to test the algorithm on cases that span a range of breast stiffnesses, we created a fourth model, of a medium-sized pre-menopausal breast. The glandular tissue was modeled as a cone with its base at the chest wall and its tip at the nipple [figure 5.6]. The three-dimensional elements of the cone were composed of a linear elastic material with a modulus of elasticity three times greater than the surrounding fat [Wellman 99, Krouskop 00]. This model was subjected to mammographic and tactile imaging compressions in the same manner as the postmenopausal models described above.

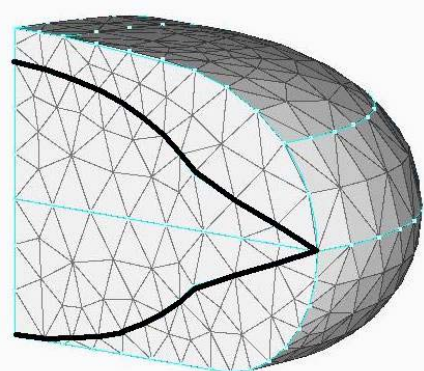


Figure 5.6. Medium pre-menopausal breast model showing outline of glandular tissue cone with base on the chest wall and apex at the nipple

5.2.3. Finite Element Model Data

Mammographic and tactile image compressions were applied to the finite element models, and the deformations at each finite element node were recorded. Total compression of up to 50% were achieved on the postmenopausal breast models under mammographic compression, while the tactile imaging compression was limited to the clinical tactile imaging pressure maximum of 100 Pa which resulted in compressions of less than 30%. The full mammographic compression and one sample compression of the tactile imager on the medium sized breast are shown in figure 5.7.

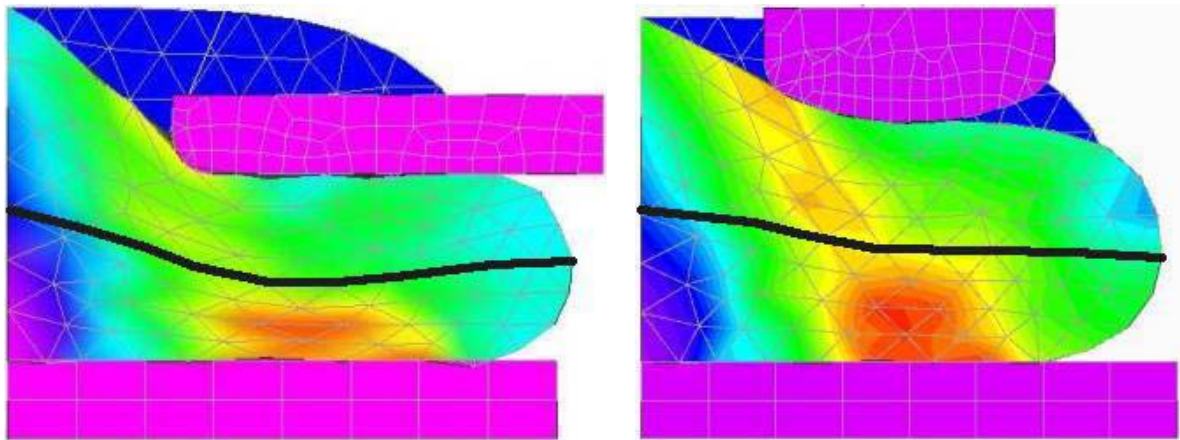


Figure 5.7. Medium-sized, postmenopausal breast model under mammographic and tactile compression, showing areas of increased von Mises stress at the base plate. The contact boundaries were non-slip and the breast tissue was fixed to the chest wall. The tactile imager scanhead was modeled at five locations and the total tactile compression was interpolated between the results. The midline of the model is shown as a dark line in each picture. In the background the outline of the uncompressed breast is seen in dark blue.

In general, the mammographic displacements were in the same direction as, but greater than, the tactile imaging displacements. The displacements for each modality on the

midplane of the medium postmenopausal breast are shown in figure 5.8. We define the midplane as the 4mm thick horizontal slice centered vertically on the nipple. Note that there is considerable sideways (x -direction) displacement, and the difference between the absolute displacements in the x -direction is greater than the absolute difference in the y -direction (away from the chest wall).

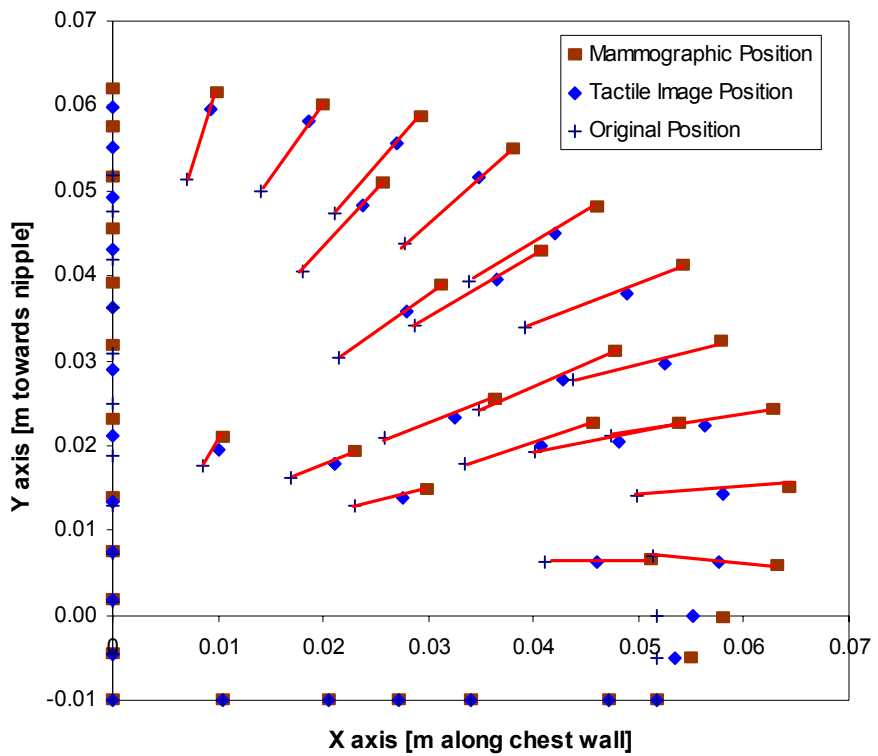


Figure 5.8. Mammographic and tactile imaging displacement field on the midplane of the modeled medium breast. The solid lines indicate the translation of the original point due to mammographic compression

5.2.4. Algorithm Development

Tactile and mammographic images are two-dimensional projections of three-dimensional information. A mammogram is a vertical projection through the compressed tissue onto a horizontal plate by near-parallel beams of x-rays. A tactile image is a projection of three-dimensional pressure information onto a flat plane that best fits the approximately horizontal surface of the top of the breast as it is compressed by the tactile imager. For each case, we need to collapse the three-dimensional deformation field information of the models into a two-dimensional field for analysis.

In order to determine a two-dimensional displacement field that is representative of the complete field, we first visualize the displacement of each point in the volume. Figure 5.9 shows the displacements of the mammographic compression for the medium breast model. The y and x displacements for points greater than 1cm above the baseplate and 1cm below the top of the uncompressed breast are shown. With reference to the anatomy of a premenopausal breast shown in figure 1.4, points beyond this range are almost certainly original fatty tissue, and are unlikely to contribute an abnormality to the image. As expected, the plot of y -displacements indicates that the further the initial position was from the chest wall, the greater the displacement. The x -displacements are slightly more complicated, since in this direction, some points are closer to the chest wall and therefore are expected to move less. There is an obvious trend, however, for points further away from the line of symmetry ($x=0$) to have a greater x -displacement, which is expected.

For displacements in each direction, the displacement of points that initially were within 2mm of the horizontal plane that contains the nipple approximate the displacements of points through the rest of the volume under mammographic compression. Thus the deformations encountered at the midplane are representative of the mammographic deformations.

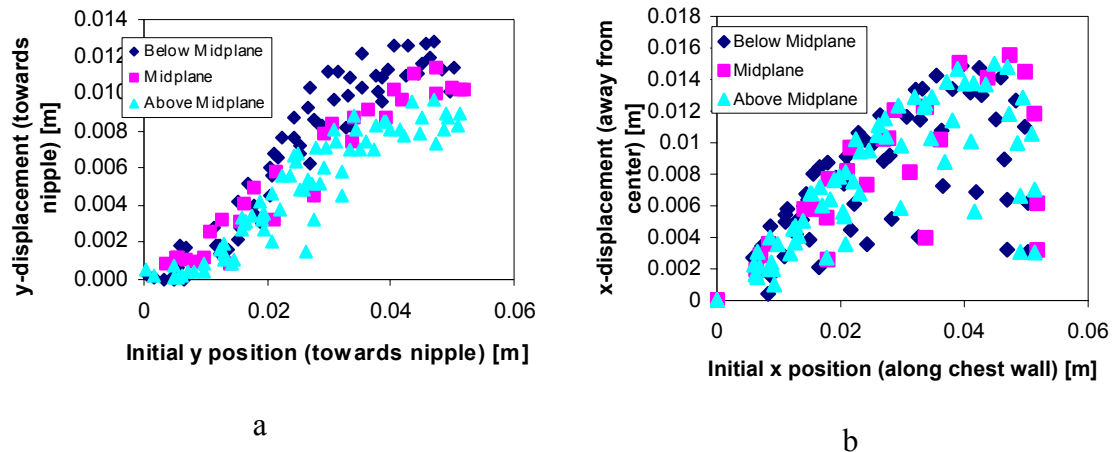


Figure 5.9. Mammographic component displacements. a) Displacement along the y direction, away from the chest wall, and b) displacement along the x direction, parallel to the chest wall. In both cases, the displacement of the points in the midplane (4mm thick plane with the nipple at midheight) approximate the displacements of the points in the rest of the volume

Figure 5.10 shows the component displacements under tactile imaging compression. The tactile imager records the palpable extent of tissues, and so points below the midline form a small contribution to the tactile image [Wellman 99]. From figure 5.10 we see that the displacement of the points on the midplane of the breast model approximate the displacements of the points in the rest of the volume as they did for the mammographic compression. This is especially true for the points above the midline, which provide a greater contribution to the tactile map.

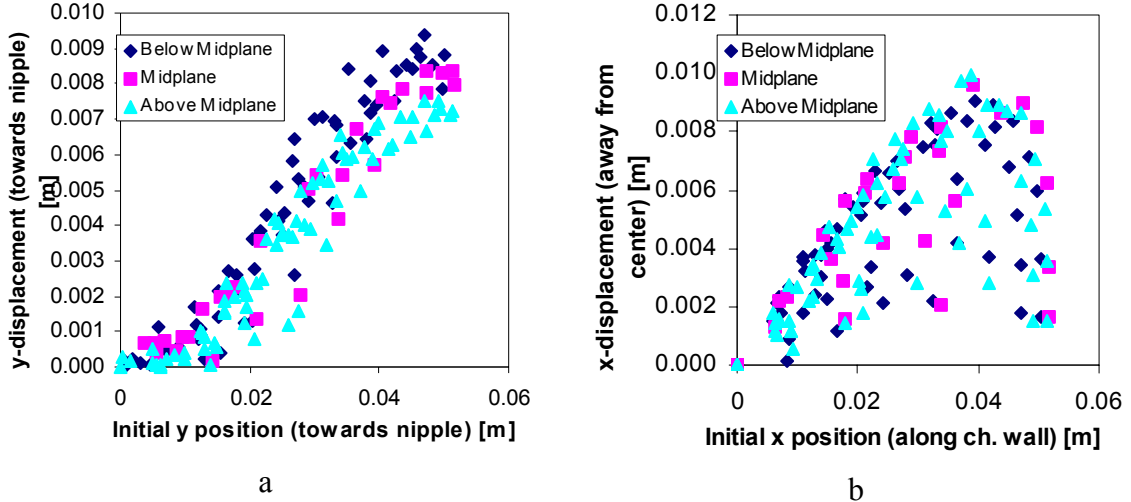


Figure 5.10. Tactile Imaging component displacements. a) Displacement along the y direction, away from the chest wall, and b) displacement along the x direction, parallel to the chest wall. In both cases, the displacement of the points on the midplane are representative of the displacements for the points in the rest of the volume, especially points in the upper half of the breast, which are stronger contributors to a tactile map

We can now focus our study on the deformation field of the points on the horizontal midplane of the breast in order to determine an algorithm to register the tactile image points to their corresponding points on the mammogram. We seek an algorithm that can register tactile images to mammograms, namely a mapping $(x,y) \rightarrow (x',y')$ such that

$$\text{Mammogram}(x,y) = \text{TactileImage}(x',y')$$

We begin by examining the data in figure 5.8 and looking for patterns in the difference between the displacements under the two compressions. We can collapse the difference in y -displacements onto one axis [figure 5.11a] and look for an appropriate function to fit the data. Fitting a function

$$\text{Required}_y\text{Displacement} = f(\text{Original}_T\text{actile}_I\text{maging}_y\text{Position})$$

shows that there is little difference in the R^2 value whether we allow the fit to have a non-zero intercept or force the fit to go through the point $Zero_Position = Zero_Displacement$. We therefore require the fit to have a zero intercept, since this is more physically reasonable. We find that a linear fit has an R^2 value of 0.71, while a second-order polynomial fits the data to $R^2 = 0.83$. If we only look at points 1cm beyond the chest wall, (which are the points of interest, as they are in the mammographic field) then the fit for both the first-order and second-order polynomials increases to $R^2 = 0.85$. Given this parity, we keep the simpler linear fit and require the registration algorithm that takes the point at y in the tactile image to y' in the mammogram to have the form

$$y' = y(1 + K_{yy}y)$$

where K_{yy} is a constant that will be determined from parameters associated with each tactile image and mammogram pair.

Performing a similar analysis for the difference in the x -displacements (along the chest wall, away from the center) yields figure 5.11b, showing a much larger spread of the data. Separating the data into bins along the y -axis shows a clear dependence on the y -position of the point in the tactile image. The slopes for the four bins shown in figure 5.11b fit a linear trend with an R^2 value of 0.97. With this in mind, we require the registration algorithm in the x direction (from x in the tactile image to x' in the mammogram) to take the form

$$x' = x (1 + K_{xx} x) (1 + K_{xy} y)$$

where the K_x are constants that will be determined from parameters associated with each tactile image and mammogram pair.

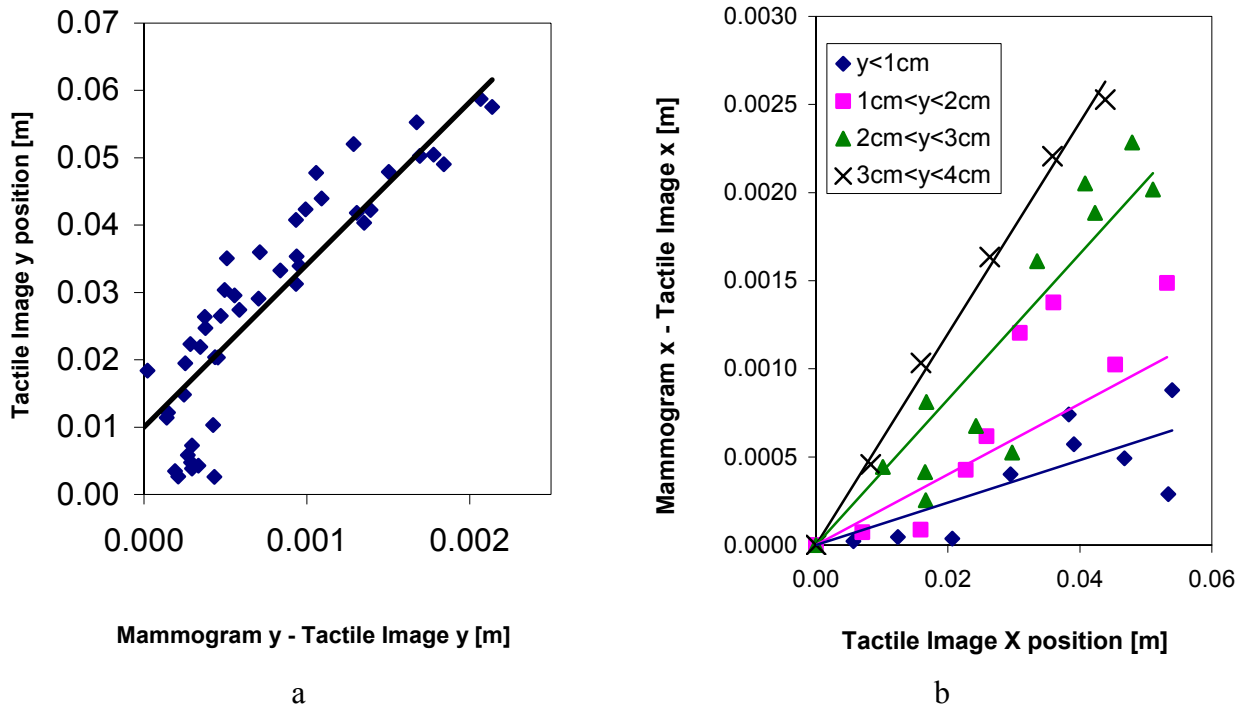


Figure 5.11. Difference in translation in y (a) and x (b) between the tactile imaging and the mammographic midplane compressions for the medium breast model. The difference in y shows a linear growth with the tactile imaging y -position, while the difference in x shows a linear relationship to both x and y .

The parameters available for registration from clinical data are parameters associated with the edges of the breast in the mammogram and the tactile image, i.e. the size of the non-background areas of the images. The parameters K_{yy} , K_{xx} , and K_{xy} must therefore be allowed to depend only on the size of the images and the total required deformation. We denote the maximum excursion of the mammogram and the tactile image in the x

direction as X_{Mm} and X_{Mt} respectively and in the y -direction as Y_{Mm} and Y_{Mt} and use these values in determining the constants K_{yy} , K_{xx} , and K_{xy} .

The parameter K_{yy} needed to stretch the tactile image in the y -direction is dependent on the difference between the values of the maximum extent in the y -direction for the mammogram and the tactile image. We therefore propose the following transformation in the y -direction:

$$y' = y \left(1 + \frac{y}{Y_{Mt}} \frac{Y_{Mm} - Y_{Mt}}{Y_{Mt}} \right). \quad (5.1)$$

Similarly, in the x -direction we expect K_{xx} to depend on the difference $X_{Mm} - X_{Mt}$. The parameter K_{xy} should, much like K_{yy} , depend on $Y_{Mm} - Y_{Mt}$. Examination of the various sized models shows a dependence on $X_{Mm} - X_{Mt}$ as well, in that the larger the difference in the x direction between the mammogram and the tactile image, the smaller the relative effect of the y -difference. We therefore propose the following transformation in the x -direction:

$$x' = x \left(1 + \frac{x}{X_{Mt}} \frac{X_{Mm} - X_{Mt}}{X_{Mt}} \right) \left(1 + \frac{y}{Y_{Mm}} \left(\frac{Y_{Mm} - Y_{Mt}}{2[2X_{Mm} - 2X_{Mt}]} \right)^3 \right). \quad (5.2)$$

The third power is an empirical constant based on the cubic relationship between the volume of tissue to be compressed and the linear difference between the amount of deformation in the two modalities.

Letting $\Delta x_{\text{stretch}} = 2(X_{Mm} - X_{Mt})$ and $\Delta y_{\text{stretch}} = Y_{Mm} - Y_{Mt}$ the transformation becomes

$$x' = x \left(1 + \frac{x}{X_{Mt}} \frac{\frac{1}{2} \Delta x_{stretch}}{X_{Mt}} \right) \left(1 + \frac{y}{Y_{Mm}} \left(\frac{\Delta y_{stretch}}{2 \Delta x_{stretch}} \right)^3 \right)$$

and

$$y' = y \left(1 + \frac{y}{Y_{Mt}} \frac{\Delta y_{stretch}}{Y_{Mt}} \right).$$

5.2.5. Finite Element Model Registration

The registration algorithm in equations 5.1 and 5.2 was applied to the deformation fields of the midplane of the modeled tactile images. Values for the constants of the registration are given in table 5.2. The location of points in the tactile image using these values match the mammographic deformation well for all four models [table 5.3]. The algorithm shows the least error for the medium sized models, which is ideal as this is expected to be closest to the median clinical case. The registration worked best for the premenopausal model. The vertical strains and resulting lateral deformations were smaller on this model than the softer postmenopausal models, due to the stiffer glandular tissue. The smaller absolute deformations incurred in this model most likely account for the smaller error in registration. The largest errors were incurred in the areas of the breast furthest from the origin. This is to be expected, as these areas experience the accumulated errors of registration in both the x and the y directions. When the registration algorithm is applied to planes away from the midplane, the errors also

decrease, probably also due to the lower total deformations in the planes away from the nipple.

Table 5.2. Values of the registration constants for the various finite element models

Model	X_{Mm}	X_{Mt}	Y_{Mm}	Y_{Mt}
Small postmenopausal	7.5cm	6.6cm	6.0cm	5.5cm
Medium postmenopausal	9.4cm	8.7cm	8.9cm	8.5cm
Large postmenopausal	11.4cm	10.6cm	12.6cm	12.2cm
Medium premenopausal	8.2cm	7.5cm	8.8cm	8.2cm

Table 5.3. Error between the registered tactile image and the corresponding points on the mammogram for the midplane of the finite element models.

Model	Mean Absolute Registration Error [% of total displacement]	Average Absolute Registration Error	Maximum Absolute Registration Error
Small postmenopausal	5.7 %	2.06 mm	6.47 mm
Medium postmenopausal	3.3 %	1.56 mm	5.03 mm
Large postmenopausal	5.0 %	2.91 mm	7.34 mm
Medium premenopausal	2.2 %	0.37 mm	2.59 mm

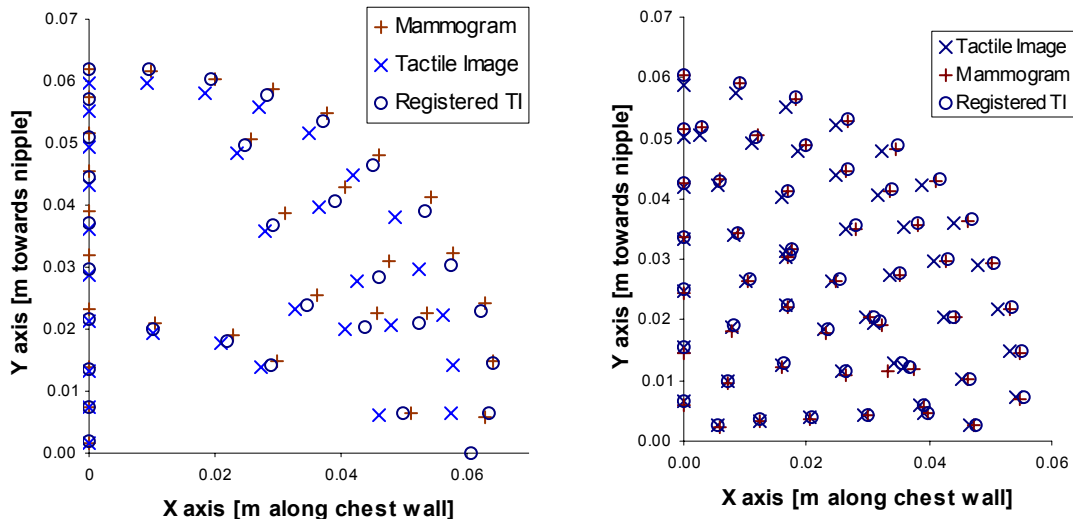


Figure 5.12. Mammogram and registered tactile image points in the midplane of the medium sized models. Left: Postmenopausal model. Right: Premenopausal model

5.3. Physical Modeling

5.3.1. Physical Model Construction

In the previous section an algorithm was developed to register points in a tactile map to the corresponding points on a mammogram based on the size of the two images. The algorithm was based on the displacements of the midplane of three breast models, which were shown to be representative of the displacements through the rest of the volume. In order to test the algorithm experimentally, we constructed a physical model of a human breast on which tactile imaging and mammography can be simulated.

The model breast was made in a mold taken of the left breast of a volunteer test subject. The subject was different from the subjects studied for the development of the finite element models, and the resulting model is slightly larger than the medium finite element model constructed in the previous section. The initial cast [figure 5.13a] was constructed of plaster bandages. The subject was vertical with the breast resting on a flat plate as it would before mammography or tactile imaging in our study. When the cast was dry, it was trimmed to a plane parallel to the flat chest wall supporting the breast, and reinforced with thick model plaster [figure 5.13b]. The inside was coated with a thin layer of enamel paint to fill the plaster pores, and lined with petroleum jelly so that the model material did not adhere to the mold.

The inside of the mold was coated with a 1.5mm layer of silicone (GE RTV 108) to simulate skin [figure 5.14]. This silicone has tensile strength similar to that of natural skin, but is transparent, allowing us to image the spheres under mammographic compression. The bulk of the model breast was formed from two-part silicone rubber (GE RTV 6166) mixed to a ratio to provide a young's modulus of 15kPa, corresponding to a postmenopausal breast. The model bulk required approximately 900mL of silicone. In order to have simulated lesions to image and confirm registration, 15mm rubber spheres with a young's modulus of 500kPa were incorporated into the model at various locations [figure 5.14]. Once cured, the final model was removed from the mold and attached to a thin (3mm) sheet of plexiglass to simulate the chest wall.

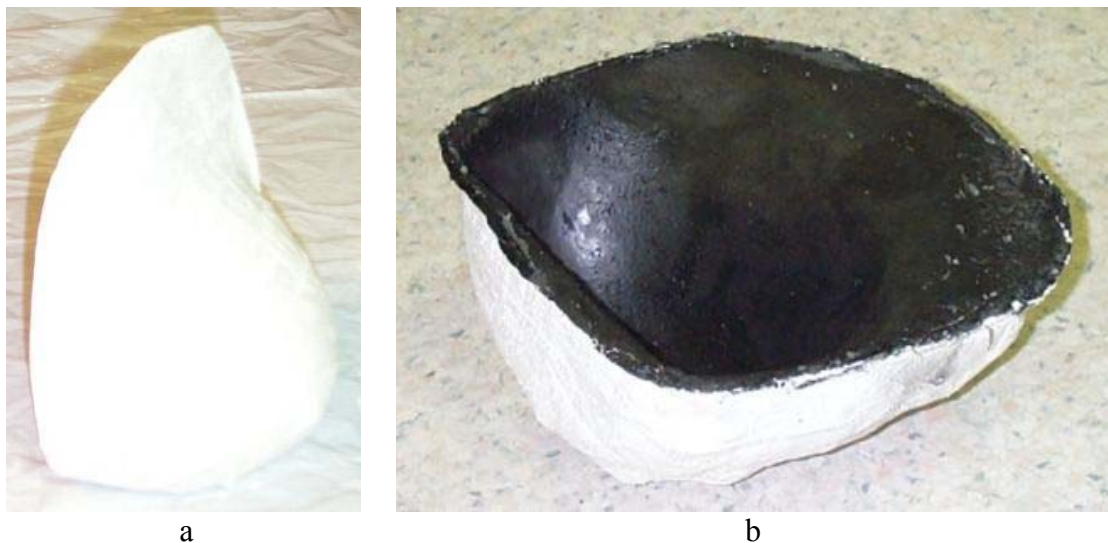


Figure 5.13. Mold for breast model. (a) An initial layer of plaster is cast on the subject's left breast and trimmed to a plane parallel to the chest wall. (b) The thin base layer is reinforced with plaster, and the hollow sealed with enamel spray and coated with a thin layer of petroleum gel before the model is cast.

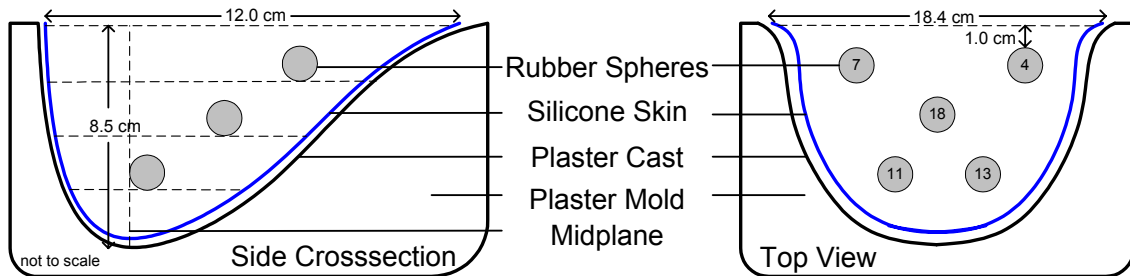


Figure 5.14. Side and top views of 3-dimensional breast model construction. Silicone (GE RTV108) was spread on the inside of the mold and allowed to cure to become the skin of the model. Soft RTV 6166 silicone was then poured in layers so that rubber spheres were placed where they can be imaged under both mammography and tactile imaging. The final model was attached to a plexiglass ‘chest wall’. In the side view, the layer interfaces and midline are indicated, though they are not physical boundaries in the actual model. The top view shows the relative arrangement of the rubber spheres, with their depth from the top surface indicated on each sphere in millimeters.



Figure 5.15. Model breast constructed to test our registration algorithm. The model is made of GE RTV 6166 two-part silicone, with modulus of elasticity if 15kPa. Rubber spheres are incorporated into the model to provide registration points. The model is coated with GE RTV 108 silicone to simulate skin and glued to a plexiglass sheet to simulate the chest wall.

5.3.2. Obtaining Model Mammogram and Tactile Image

In order to test the registration algorithm, we obtained a tactile image and simulated mammogram of the model built in the previous section. Both images were obtained with the model breast supported on a rigid horizontal surface. A tactile image was taken using the laboratory imager detailed in §1.4.1, with the tactile frame positions located in three dimensions using the magnetic tracker. Metal objects were eliminated as much as possible from the field of interest to minimize disturbance of the recorded positions. The imager was covered in Parafilm (M) and the surface of the breast model lubricated as in clinical tactile imaging.

The mammogram was obtained by compressing the model manually under a clear plexiglass plate (3/4" thick to eliminate bending of the plate). The plate was positioned with one edge parallel to the chest wall, at a distance of approximately 1cm, similar to a clinical mammography machine. The plate was held compressed in a horizontal position while a digital picture was taken from above, resulting in an image of the compressed outline of the model as well as the positions of the spheres within the model in a simulated mammogram [figure 5.16]. The 9.5cm thick model was compressed 26% to 7cm thick. The camera had a focal length of 5 cm and was positioned 100 cm above the base plate, so distortion through the breast model bulk is minimal. The pixel size in the mammograms was 0.018 mm, corresponding to a block 11 pixels square in the tactile image (pixel size 2mm).

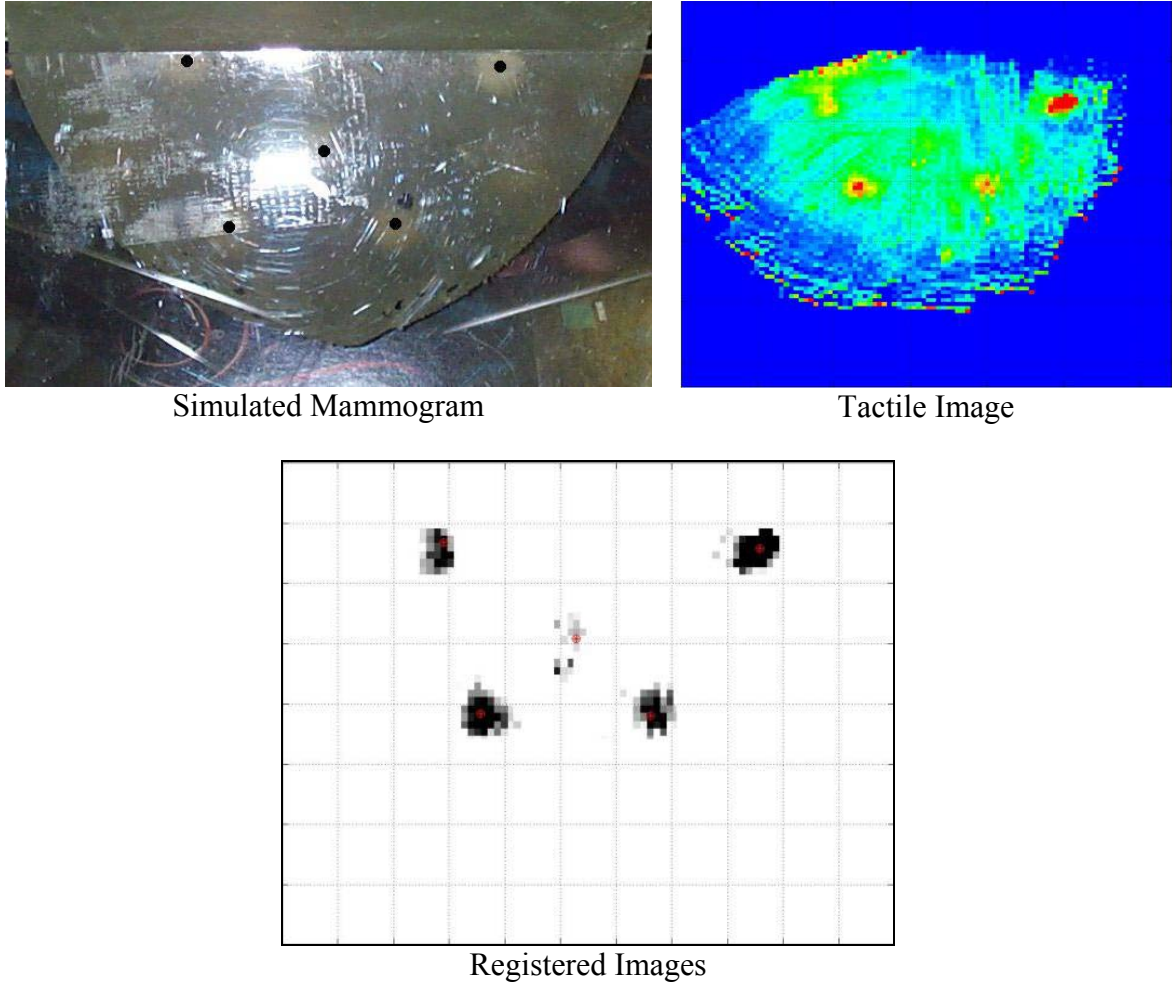


Figure 5.16. Mammogram, tactile image, and overlaid registration of the breast model. The spheres in the mammogram are marked with black dots. The bottom image shows the registered tactile image (thresholded and with edge effects eliminated), with the sphere positions from the mammograms overlaid as red dots.

5.3.3. Experimental Results

A simple threshold was used to eliminate the background of the mammogram and tactile image. For the tactile image, sharp edge effects were eliminated manually. The centroids of the 5 spheres were calculated as the center of mass of an area at least 8 mm

square around the image of each sphere. The centroids of the spheres in the simulated mammogram were identified manually, since the sphere image edges were very faint and blurry in the simulated mammogram. The tactile image was registered to the mammogram as outlined in § 5.2.4.

Figure 5.16 shows the results of the calibration, namely the registered tactile image of the embedded spheres overlaid with the positions of the spheres in the mammogram. The registration of the two images has an average error of 1.3 mm between the centroids of the spheres in the mammogram and the tactile image. This is considerably improved over the error to the calibrated but not registered tactile image of 2.4 mm. The largest error after registration is 1.9 mm for the central sphere, most likely because it was the deepest sphere and thus the most difficult to image.

5.3.4. Discussion

As seen in figure 5.16, the registration of the tactile image to the mammogram of the model breast is quite good. This is to be expected since the silicone model is composed mainly of a homogenous, linear elastic material, as were the finite element models used to devise the registration algorithm. Errors in the registration of the two images may stem not only from the registration itself, but also from magnetic warping in the tactile image and errors in identifying the exact centroids of the spheres. Registration of the two images was computationally expedient, since only one calculation has to be performed for each pixel in the tactile image. In the process employed here for registration, the

longest time was taken in identifying the points of interest in the mammograms. This is expected to be the case for actual clinical data as well. The success the registration algorithm incurred for the model data is sufficient to move on to testing on clinical data.

5.4. Preliminary Clinical Testing

The registration algorithm developed in the previous sections resulted in low errors in the registration of finite element and physical model data. The algorithm was developed with an eye to applying the registration to tactile images taken alongside clinical mammograms. The next step in moving towards this goal, therefore, is to develop a protocol for obtaining tactile images in a clinical setting with synchronized mammograms, and testing the registration on a limited set of clinical data. Successful completion of this stage will require not only support of the registration algorithm, but also implementation of a relatively efficient and subject-friendly data collection that can be seamlessly integrated into existing clinical practice.

5.4.1 Clinical Data Acquisition

As a preliminary study of the clinical application of our registration algorithm, we tested the registration on mammograms and tactile images from subjects undergoing breast cancer screening in order to establish a protocol for obtaining and registering tactile images in a clinical setting. Eleven subjects were recruited who were scheduled to

undergo a routine mammogram. The subjects were all female, with ages from 35 to 70 (average age 54), and were representative of the relative risk of breast cancer. They spanned the range from premenopausal to postmenopausal (2 premenopausal, 2 perimenopausal, and 7 postmenopausal), from small breasts to large breasts (brassiere sizes A to DD, with C as the median), and included women with previous positive and negative biopsies (7 of the 11 have had previous biopsies, 5 of which were positive). Tactile images were recorded on each breast directly after the crano-caudal mammogram, before the subject moved relative to the bottom plate of the mammogram [figure 5.17]. The tactile images were obtained starting from near the chest wall at the center of the breast and moving in parallel stripes away from the chest wall to the left and right of the center of the breast [figure 5.18].

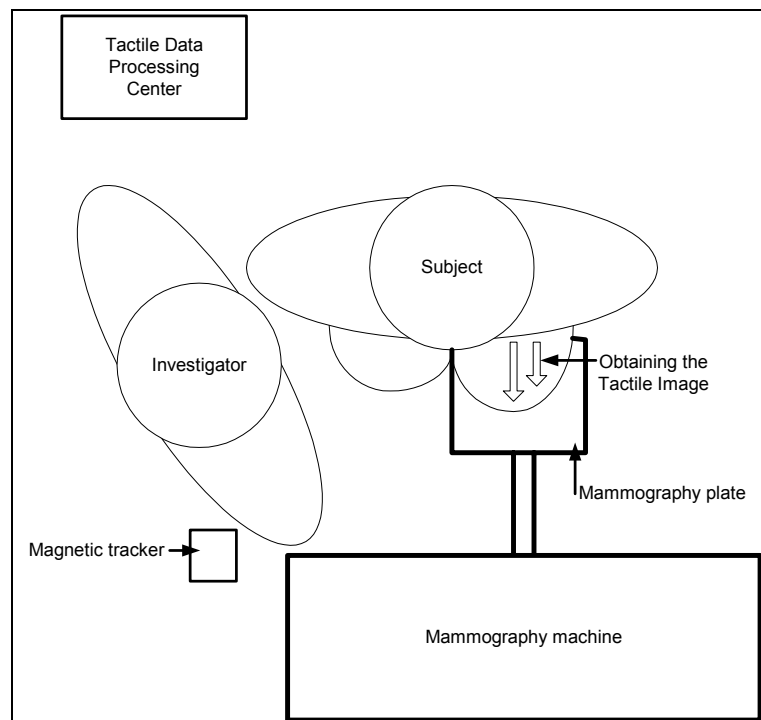


Figure 5.17. Experimental setup, top view. After the crano-caudal mammogram was obtained the tactile image was obtained on the same breast before the subject moved.

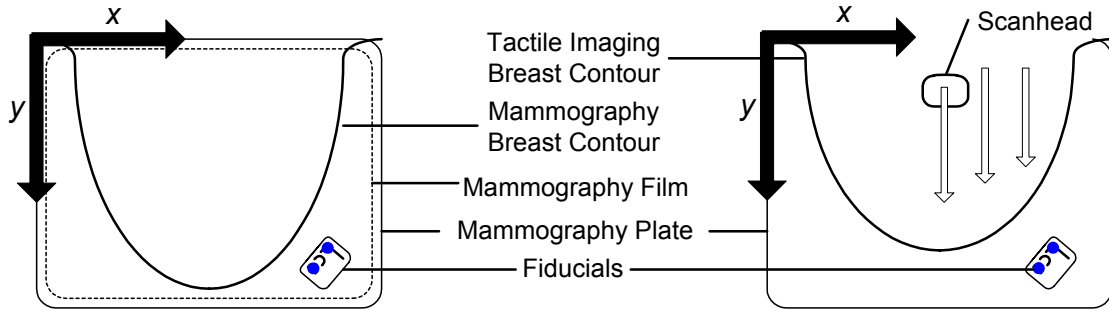


Figure 5.18. Top views showing imaging setup and expected maximum contours of a mammogram and tactile image. Without the compression of the top mammography plate, the breast relaxes into a smaller horizontal contour. The tactile image (right) was obtained in swipes moving away from the chest wall, starting with the center and moving outwards first to one side then the other.

The tactile imager used in the clinical data acquisition is the clinical imager described in §1.4.1, which uses magnetic positioning in order to locate the pressure frames. Unfortunately, the mammography machine and other metal objects in the room distort the positioning field. Due to this magnetic distortion, we expect errors in the positioning of the information in the tactile image [LaScalzaa 03, Milne 96, Poulin 02]. The relative error from one pixel to the next is incremental, however, resulting in an overall warping of the tactile image, which we can account for by obtaining global background calibration information.

A cartesian coordinate system is employed due to the rectangular shape of the mammography plate. The x axis, $y = 0$, is the top edge, along the chest wall, with y increasing towards the nipple. The y axis, $x = 0$, is to the left of the breast as viewed from the investigator, with x increasing towards the woman's left, for either breast [figure 5.18].

The tactile images were 30 x 30 cm in extent, which was sufficient to record the entire area of the largest mammographic plate. The tactile image resolution was 0.5mm by 0.5mm per pixel achieved by sub-sampling the pressure sensels [Wellman 99]. The mammograms were digitized per a standard digitizing technique [Health 02]. The resolution of the digitized mammograms was set at 0.5mm/pixel to correspond to the resolution of the tactile images. The top left corner of the mammographic film is assigned to $(x,y) = (1,1)$ cm, since the film is 1 cm smaller than the mammography plate on each side. The mammograms were digitized on a three-colour scale and converted to a single channel intensity scale using a standard intensity algorithm of $I = 0.30R + 0.59G + 0.11B$ [Marginal 02].

5.4.2. Calibration

Since the warping due to the magnetic field distortion and the registration required due to the mammographic compression are independent, we treat them separately, calibrating for the effects of the magnetic field before registering the tactile images to the mammogram.

Calibration method

Our goal is to establish a two-dimensional field of the displacements required to map each point in the collected tactile image to the corresponding point calibrated to the

mammography plate. This field will take the form $[U(x,y), V(x,y)]$ for the required displacements in the x and y directions, respectively, such that

$$(x_{cal}, y_{cal}) = (x + U(x,y), y + V(x,y)).$$

The calibration field will be established based on two pieces of information: calibration to the edge of the mammography plate, which is approximately constant for all subjects, and calibration to mammographic fiducials, which is different for each tactile image collected.

Available Calibration Information

Background calibration information was obtained from the mammography plate and the mammography markers used to label each mammogram. Plate information was acquired by taking a tactile image of the centerline of the plate, the edge closest to the patient (along $y = 0$) and the edge furthest from the magnetic tracking device ($x = 0$) [figure 5.19]. Since the tactile imager should not be used to image hard edges, the plate edges of interest were covered with a layer of soft foam approximately 2.5cm wide and 1cm thick. A half-cylinder of rubber with approximately 2cm diameter was placed on the centerline, and covered with the same foam. The mammography markers used to identify the mammographic view were also modified with foam dots which could be imaged in the tactile image without altering the radioopacity of the markers for mammographic use [figure 5.20]. This provided another set of registration points, two fiducials approximately 1.5cm apart, specific to each mammogram/tactile image combination.

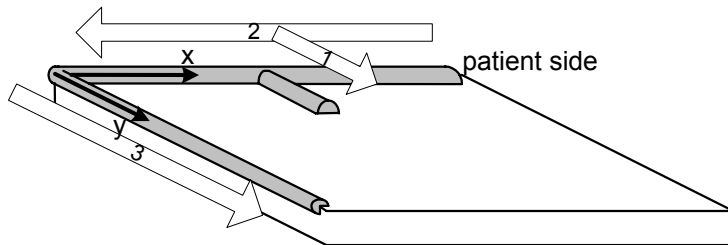


Figure 5.19. Mammography plate with foam along two edges and centerline used to record the plate position in the tactile image.

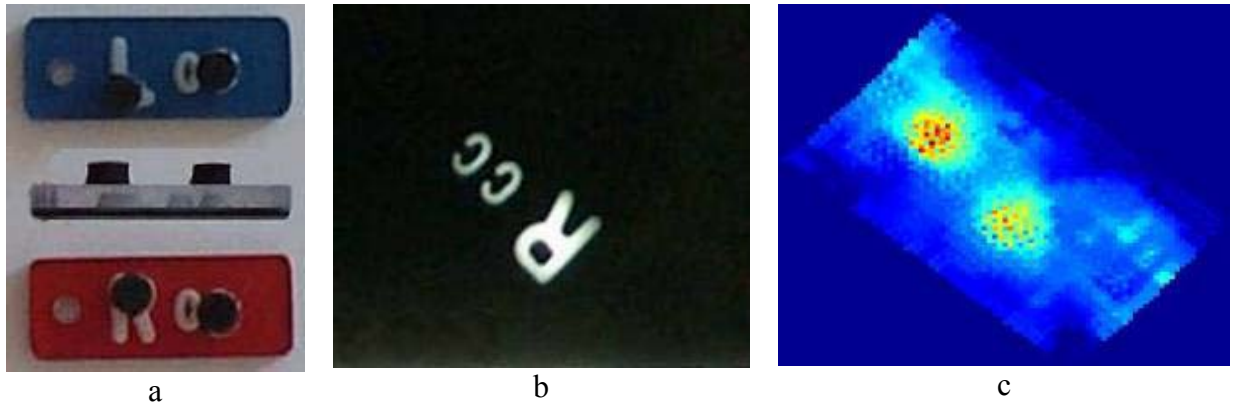


Figure 5.20. (a) Left (Lcc) and right (Rcc) cranio-caudal mammography markers. Black foam dots were glued onto the second ‘c’, the corner of the ‘L’ and the head of the ‘R’ for registration to the tactile image as fiducials for calibrating the tactile images. (b) and (c) show a mammographic and tactile image of the same marker.

The calibration lines corresponding to the centerline and two edges of the mammography plate are shown in figure 5.21. Since the lines were obtained by tactile imaging, they have finite width. The line of interest is taken through the maximum along each line’s tactile image. The fiducial in the mammogram is taken to be the center of the second ‘c’, the inner corner of the ‘L’, and the center of mass of the head of the ‘R’, as applicable. For the tactile image, the general area of the fiducial is identified, and the center of mass of the pixel intensity corresponding to the foam is taken as the fiducial center.

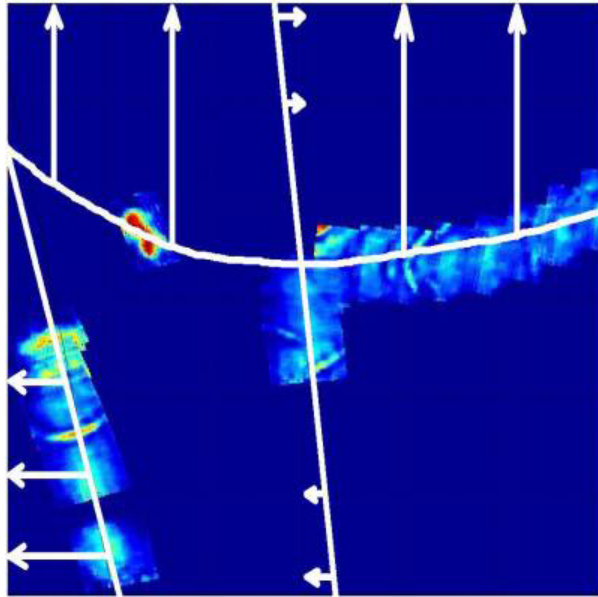


Figure 5.21. Tactile image of left edge, center swipe, and top edge of the mammography plate for the second day of clinical data acquisition. Superimposed in white are the lines fit to these warped edge calibration lines, and arrows indicating the required displacements of these lines for calibration with the mammography plate. The field is 30x30cm.

Calibrating with the Edge Information

The required x -displacements of the uncalibrated plate edge and plate center are well fit by a 1st order polynomial (figure 5.21), and so from this we get two equations:

$$f_1(y) = a_{u1}y + b_{u1} \quad (5.3)$$

which is the required displacement of the line $x = a_{u1}y + b_{u1}$ so that it maps onto the plate edge at $x = 0$; and

$$f_2(y) = a_{u2}y + b_{u2} \quad (5.4)$$

for $x = a_{u2}y + b_{u2} + X/2$ to map to the centerline $x = X/2$, where X is the maximum extent in the x direction, namely 30cm.

The mapping of the plate top is neither linear nor symmetrical and so is fit with a 3rd degree polynomial, resulting in

$$g(x) = a_vx^3 + b_vx^2 + c_vx + d_v \quad (5.5)$$

for the line $y = a_vx^3 + b_vx^2 + c_vx + d_v$ to map onto the line $y = 0$.

In the absence of further information the calibration field is complete. In the x -direction we have calibration information along two distinct lines, so we can interpolate the results to construct the final field. In the y -direction we only have calibration information along one line, so we assume this is valid through the entire map. With plate calibration information only, then, the calibrated Tactile Image becomes

$$\text{CalibratedTI}(x, y) = \text{OriginalTI}\left(x + \frac{f_2(y) - f_1(y)}{X/2 + f_2(y) - f_1(y)}(x - f_1(y)) + f_1(y), y + g(x)\right)$$

The above transformation accounts for a great deal of the raw calibration, and is common to all of the tactile images collected.

Calibrating with Fiducial Information

The calibration field created using the plate edge information was modified for each tactile image based on the fiducial information. With fiducials located at x positions $x_{fid\min}$ and $x_{fid\max}$ and y positions $y_{fid\min}$ and $y_{fid\max}$ in the tactile image, we calculate the required horizontal and vertical displacement of each of the two fiducial points to map to the corresponding fiducials on the mammogram. The straight line between the two fiducials is mapped by a linear interpolation of these displacements (i.e. the point exactly halfway between the two fiducial points in the tactile image is mapped to the point exactly halfway between the two fiducial points in the mammogram). The resultant information is contained in the 1st order polynomials $u_{fid}(x,y)$ and $v_{fid}(x,y)$, valid for

$$x = \left(\frac{y - y_{fid\min}}{y_{fid\max} - y_{fid\min}} \right) (x_{fid\max} - x_{fid\min}) + x_{fid\min}$$

with $x_{fid\min} < x < x_{fid\max}$ and $y_{fid\min} < y < y_{fid\max}$. This information is combined with the information from the plate edge calibration in equations 5.3 to 5.5 to create smooth horizontal and vertical calibration fields $U(x,y)$ and $V(x,y)$ as explained below.

For the x and y ranges for which we have the fiducial information, namely $x_{fid\min} < x < x_{fid\max}$ and $y_{fid\min} < y < y_{fid\max}$, we once again fit a polynomial through the data afforded by the fiducials and the plate edge matching. The polynomial is second degree in the x -direction and first degree in the y -direction, so that no information is artificially created. Namely, for calibrating in the horizontal direction:

For $y_{fidmin} < y < y_{fidmax}$ we have three pieces of information: f_1, f_2 and u_{fid} .

Therefore, we can find a unique polynomial field $U(x,y) = A_u(y)x^2 + B_u(y)x + C_u(y)$ where the coefficients A_u, B_u and C_u are the least-squares solution M_u to

$$\begin{aligned} u &= XM_u \\ \begin{bmatrix} f_1(y) \\ f_2(y) \\ u_{fid}(y) \end{bmatrix} &= \begin{bmatrix} (f_1(y))^2 & f_1(y) & 1 \\ (f_2(y)+X/2)^2 & f_2(y)+X/2 & 1 \\ x^2 & x & 1 \end{bmatrix} \begin{bmatrix} A_u \\ B_u \\ C_u \end{bmatrix} \end{aligned} \quad (5.6)$$

$$\text{where } x = \left(\frac{y - y_{fid\ min}}{y_{fid\ max} - y_{fid\ min}} \right) (x_{fid\ max} - x_{fid\ min}) + x_{fid\ min}.$$

Similarly, in the vertical direction, for $x_{fidmin} < x < x_{fidmax}$, we know g and v_{fid} , and so we can find $V(x,y) = A_v(x)y + B_v(x)$ where A_v and B_v are the solution M_v to

$$\begin{aligned} v &= YM_v \\ \begin{bmatrix} g(x) \\ v_{fid}(x) \end{bmatrix} &= \begin{bmatrix} g(x) & 1 \\ y & 1 \end{bmatrix} \begin{bmatrix} A_v \\ B_v \end{bmatrix} \end{aligned} \quad (5.7)$$

$$\text{where } y = \left(\frac{x - x_{fid\ min}}{x_{fid\ max} - x_{fid\ min}} \right) (y_{fid\ max} - y_{fid\ min}) + y_{fid\ min}.$$

For calibrating in the vertical direction the equations for A_v and B_v can be written directly as

$$\begin{aligned} A_v &= \frac{g(x) - v_{fid}(x)}{g(x) - y_{fid}} \\ B_v &= g(x) \left[1 - \frac{g(x) - v_{fid}(x)}{g(x) - y_{fid}} \right] \end{aligned} \quad (5.8)$$

Incorporating equation 5.8 into our calibration algorithm we get

$$\text{CalibratedTI}(x,y) = \text{OriginalTI}(x + U(x,y), y + V(x,y))$$

$$\text{CalibratedTI}(x,y) = \text{OriginalTI}\left(x + A_u(y)x^2 + B_u(y)x + C_u(y), y + g(x) + (y - g(x))\frac{g(x) - v_{fid}(x)}{g(x) - y_{fid}}\right)$$

valid for $x_{fidmin} < x < x_{fidmax}$ and $y_{fidmin} < y < y_{fidmax}$.

We extend the range of validity of these fields $U(x,y)$ and $V(x,y)$ to the rest of the rows and columns for which we do not have fiducial information by adjusting the parameters M_u and M_v from the adjacent rows and columns for which we have information such that the errors to the information at each row or column are minimized. The parameters M were varied across the entire range $98\% M_{old} \leq M_{new} \leq 102\% M_{old}$ and the combination of parameters that resulted in the smallest error was taken. This narrow range was sufficient to minimize computation time and keep the final displacements field smooth, while allowing for a minimum to be found in 96% of the rows and columns. In 4% of the cases, the parameter combination required was outside or on the edge of this range. In these cases, the combination of parameters at the edge of this range that gave the smallest

error was kept in order to keep the final calibration fields smooth in keeping with the laws of magnetism. For each row we minimize the error of fitting to the required calibrating displacement of the side edge and center swipe

$$\varepsilon_u = \sqrt{(f_1(y) - U(f_1(y), y))^2 + (f_2(y) - U(f_2(y) - X/2, y))^2}$$

and for each column we minimize the error of fitting to the required calibrating displacement of the top edge

$$\varepsilon_v = |g(x) - V(x, g(x))|.$$

With the calibration field $[U(x,y), V(x,y)]$ completed [Figure 5.22], the final calibrated Tactile Image becomes

$$FullCalibratedTI(x, y) = OriginalTI(x + U(x,y), y + V(x,y)).$$

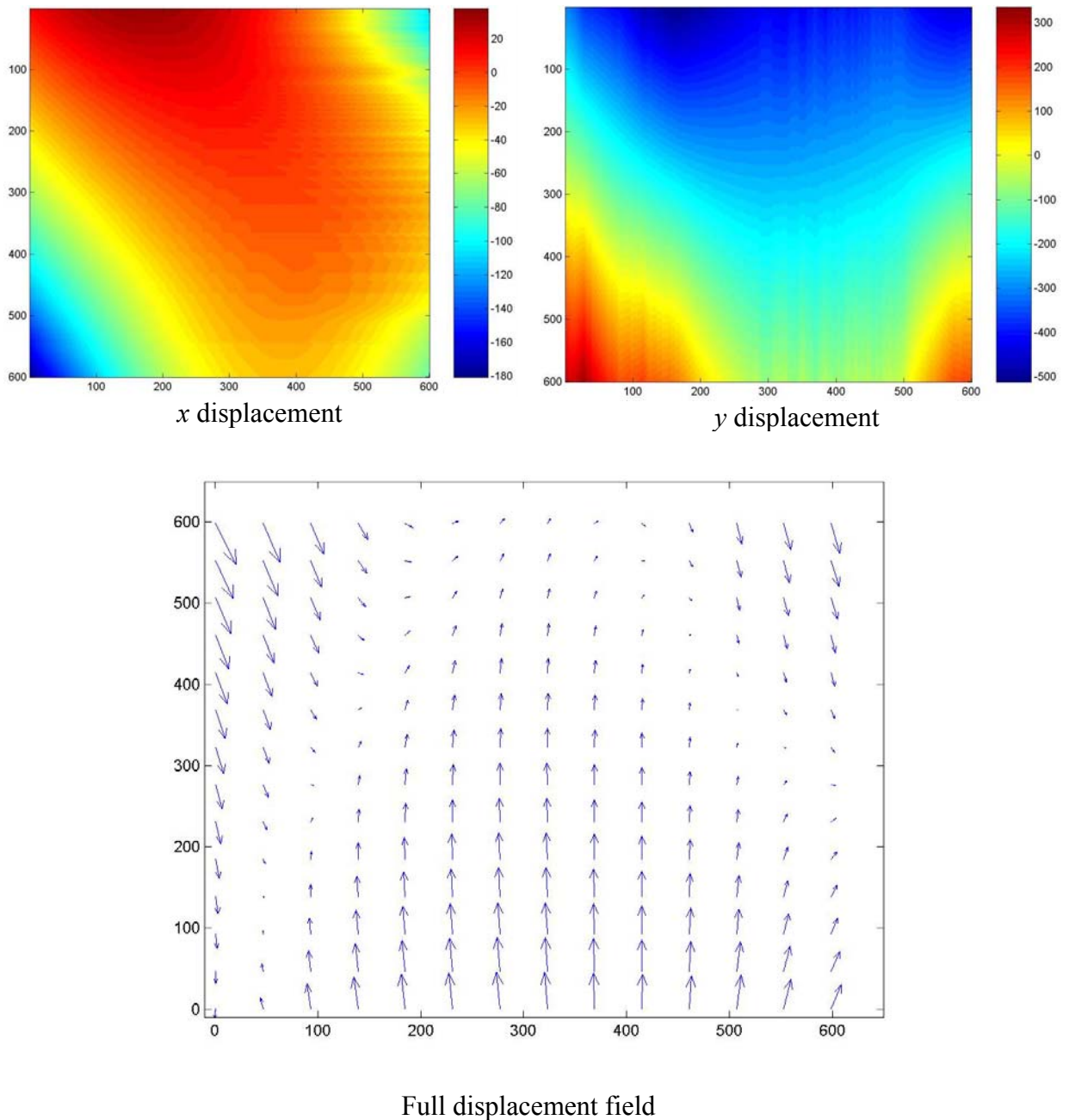


Figure 5.22. Sample calibration field for one tactile image using both plate and fiducial information. The axes indicate position (in # pixels) and the colorbar indicates the required displacement of each point, also in pixels. Top left: horizontal displacement required of the tactile image for calibration (positive is to the right). Top right: vertical displacement calibration (positive is downwards). Bottom: Sparse quiver plot of full displacement field (arrow sizes are relative to each other)

Calibration Errors

The calibration field calculated above is necessary due to the distortion of the position recording. This is due to the warping of the magnetic field used to calculate the position of our tactile frame data, caused by the presence of objects in the field of the magnetic position tracker. The main culprit for the magnetic warping is the large mammography machine itself. The relative position of the magnetic tracker to the mammography machine was maintained approximately constant, so its effects can be accounted for by the plate edge calibration. Another source of magnetic distortion is the presence of humans in the magnetic field. The positions of the subject and investigator were different between the collection of the tactile image and that of the plate edge data. Therefore the fiducials, which are collected at the same time as the tactile image, must account for the effect of the human presence.

The plate edge calibration was only collected once per clinical day (approximately once every four subjects), and although the location of the magnetic tracker was marked on the floor, any shift between patients can result in errors in the calibration. The fit of the plate information to the functions chosen to represent them was quite good, with a mean absolute error of less than 1.5mm for the straight lines, and 2.1mm for the curved top edge. The largest errors occur at the ends of the lines, and so are not expected to result in large errors in the actual images.

The calibration adjustment based on the fiducial information is also a source of error due to the proximity of the two fiducials. Even a small error in the relative position of the fiducials can be amplified upon extrapolation, and was the main reason why we employed an error minimization algorithm rather than a simple extrapolation for the generation of the entire displacement field. The effect of the mammography fiducials themselves on the magnetic field of the tactile imager tracker is unknown. Errors caused by the fiducial calibration, however, are tempered by the fact that the overall effect of the fiducial calibration is small, typically accounting for a 1.5cm displacement at the edges of the 30cm field of view.

5.4.3. Clinical Registration

The calibration algorithm developed in the previous section was applied to all 22 tactile images collected. In order for the registration algorithm of equations 5.1 and 5.2 to be applied, the parameters X_{Mm} , X_{Mt} , Y_{Mm} and Y_{Mt} , corresponding to the maximum excursion in the x (X_M) and y (Y_M) directions of the mammograms ($-_m$) and tactile images ($-_t$) must be determined. These parameters were determined from the edge contours of the images.

In order to find the mammogram edge, a threshold was established to separate the background noise from the mammogram. After eliminating the fiducials, the edge of the mammogram was found using a collapsing contour which was collapsed to values at a threshold set above the background noise (10% of the peak value). Specifically, for each

x location, the furthest extent of the mammographic image signal was recorded, and for each y location, the furthest left and right extents of the signal were recorded. The same edge-finding algorithm was used on the tactile images, but a non-zero threshold is not needed since there data outside of the region scanned on the breast is absent. An example of the resulting contours is shown in figure 5.23.

The edges thus found are not shaped in the familiar breast silhouette. The mammograms tend to be darker near the base, where there is less glandular tissue. The tactile images, on the other hand, tend to be void near the nipple, since the connective tissue under the nipple tended to retract it under tactile imaging, and so this area was not well recorded. In seeking an appropriate fit to the rough edge data found by the collapsing contour method, we look again at the finite element model data.

The finite element edge data showed a better fit to a fourth order polynomial (specifically, $y=ax^4+bx^2+c$, since there is perfect symmetry in the finite element models) however in the real mammographic data, two cases were seen: one where the fit generated by second order polynomials in x or x^2 varied by only a few percent, and the other where the fourth order fit (second order in x^2) became unstable and provided results such as a concave shape near the nipple, which is physically unreasonable. This occurred when the edge of the mammogram near the base of the breast was not easily defined due to the lack of glandular tissue. Since the second order polynomial has a more constrained shape (namely, a parabola) the second order fit remains well behaved even in the absence of information at the base. Applying a fourth-order fit to the tactile imaging data showed

similar problems due to the lack of information at the tip of the contour. A second-order fit remained stable across all tactile images, and was very similar to the fourth-order fit for the cases where the latter remained physically reasonable.

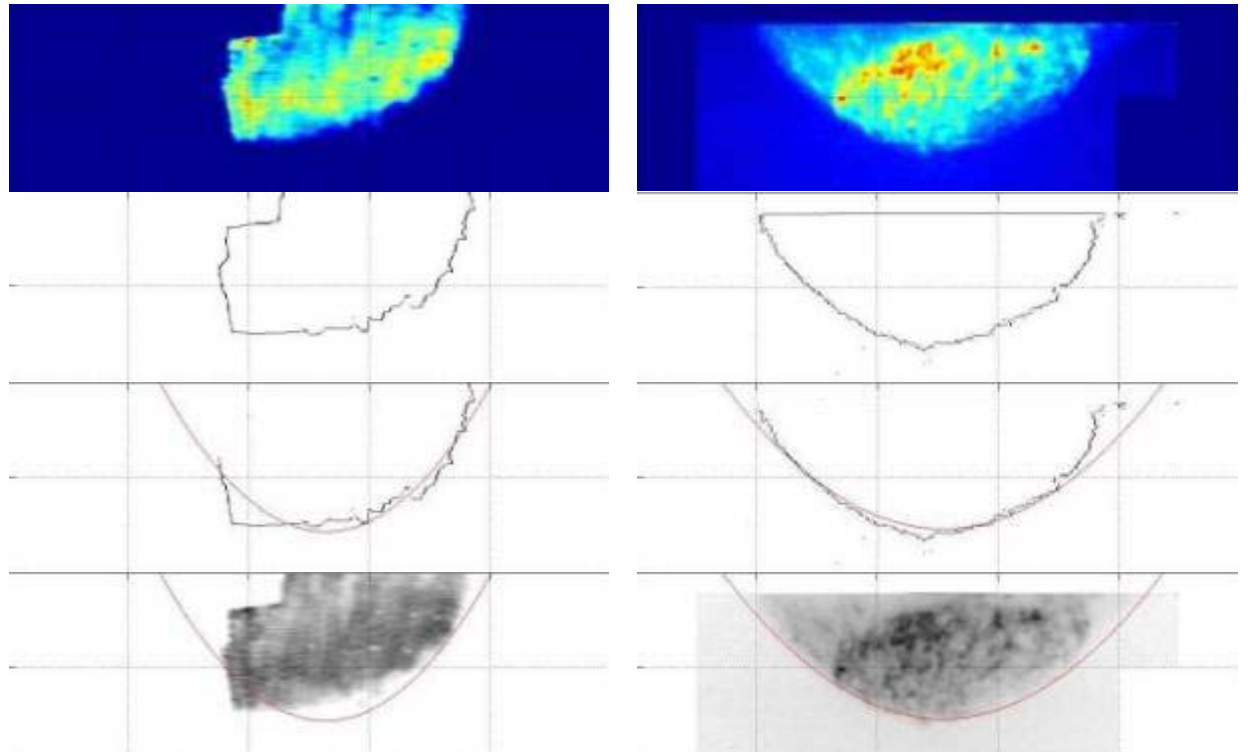


Figure 5.23. Fitting a parabolic edge to the tactile image (left) and mammogram (right). The tactile image has been calibrated but not yet registered. The field of view in each image is 10cm x 25cm. From the top are shown the original images, the coarse edge found by a collapsing contour, the parabolic edge fit to the maximum y excursion of each edge, and the edge overlaid on the original image

The parameters that are obtained from a parabolic fit to the edge and thus define each breast shape are indicated in figure 5.24. Note that the roots R_L and R_R are obtained from the parameters of the parabola $y = -a(x-b)^2 + Y_m$ by

$$R_{L,R} = b \mp \sqrt{\frac{Y_m}{a}} .$$

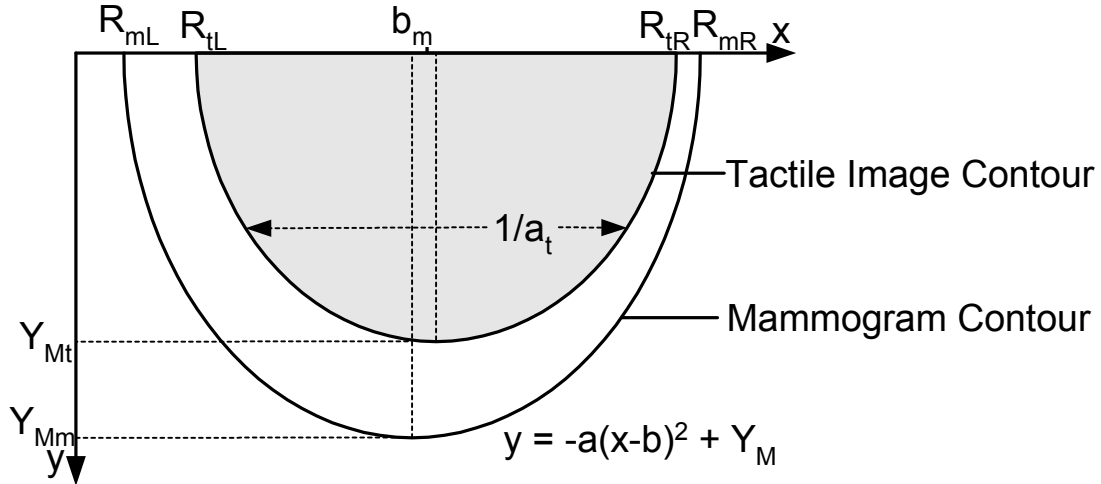


Figure 5.24. Parameters extracted from the edge of the mammograms and tactile images used to register the tactile images to the mammograms.

Once $[a, b, Y_M]$ are found for each tactile image and mammogram pair, the central values b and size parameters a and Y_M can be compared. For each pair, Y_{Mm} for the mammogram was greater than the Y_{Mt} for the tactile image, as expected from the above discussion. The central value b differed by up to 1cm, which can be due to multiple factors, including a shift in the subject position, error in calibrating for the effects of the magnetic field, incomplete tactile imaging on one side of the breast, and breast asymmetry. In this general case of $b_m \neq b_t \neq 0$ the registered x coordinates have to be shifted to $(x' - b_m)$ and $(x - b_t)$. With $\Delta x_{\text{stretch}} = (R_{mR} - R_{mL}) - (R_{tR} - R_{tL}) = 2(R_{mR} - R_{tR})$ and $\Delta y_{\text{stretch}} = Y_{Mm} - Y_{Mt}$ the registration algorithm thus becomes:

$$x' = b_m + (x - b_t) \left(1 + (x - b_t) \frac{\frac{1}{2} \Delta x_{\text{stretch}}}{(R_{tR} - b_t)^2} \right) \left(1 + \frac{y}{Y_{Mm}} \left(\frac{\Delta y_{\text{stretch}}}{2 \Delta x_{\text{stretch}}} \right)^3 \right)$$

and

$$y' = y \left(1 + \frac{y}{Y_{Mt}} \frac{\Delta y_{stretch}}{Y_{Mt}} \right).$$

This transformation was applied to each of the calibrated tactile images in order to register them to their corresponding mammograms.

5.4.4. Clinical Data Results

The above registration algorithm was applied to register the calibrated tactile images to the digitized mammograms and the resulting images compared. Figure 5.25 shows the uncalibrated tactile image, and the registered images for a subject (one breast). The registered tactile image shows increased intensity in similar regions as the mammogram. This was qualitatively noted across all 22 mammogram-tactile image pairs available.

A true test of registration for these images within the noninvasive framework requires the registration of specific points between the two modalities that are known independently to correspond. To that end, the twenty-two mammograms collected were presented to a radiologist, who was asked to outline areas of expected stiffness and areas of interest, namely areas that may require a radiologist to pause and scrutinize the area in further detail. Areas of expected stiffness included areas of dense glandularity, areas of scarring, and areas of large calcifications that may be close to the surface. The areas of interest that the radiologist identified possessed similar criteria, as he identified areas where the glandular tissue provided a radiologic signature that was distinct to his trained eyes. Because of the criteria used by the radiologist in outlining the areas of interest, if the

registration algorithm performs well we expect that the outlined areas will correspond to areas of intensity in the tactile images. Since these mammograms were collected in a screening setting, pathologies were not expected. In fact, only one area was highlighted for 15 mammograms, two areas in each of 3 mammograms, three areas in another 3 mammograms, and four in just one mammogram.

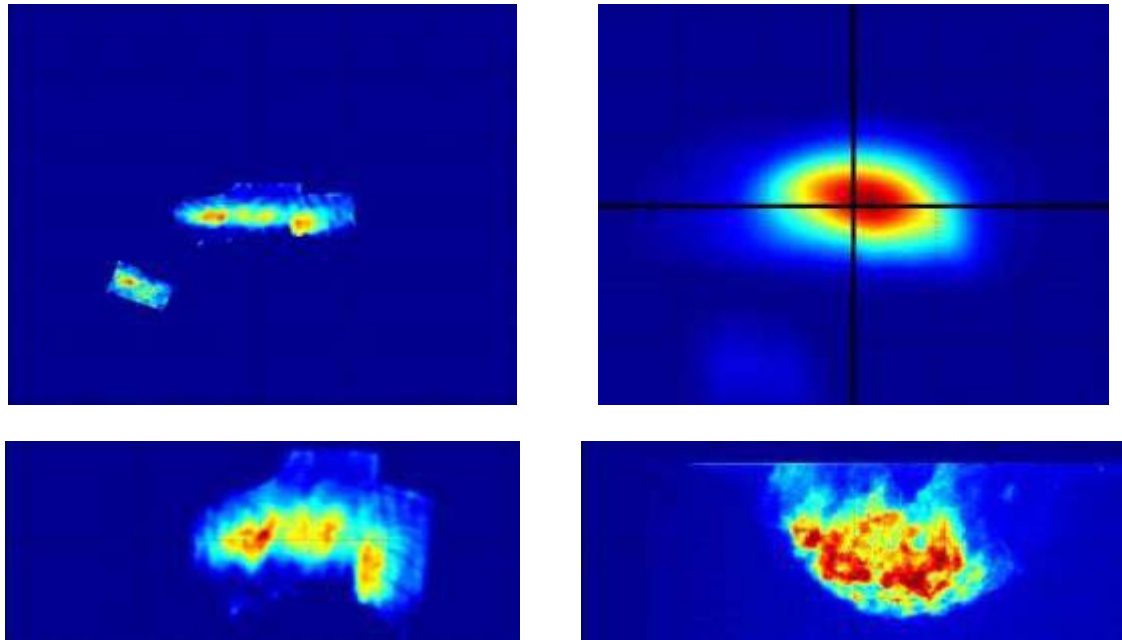


Figure 5.25. Top left shows the uncalibrated tactile image in the full 30cm x 30cm field of view. At bottom left is the tactile image after calibration and registration, shown for 10cm in y and 20 cm in x . At bottom right is the corresponding mammogram (also 10cm x 20cm). All images are represented by a single intensity value at each pixel, which is represented here with blue as the lowest and red the highest value. The bottom of the tactile image, corresponding to the area close to the nipple, is not as full as the mammogram because the tactile imager cannot obtain images at the sloping edge of a breast. The mammogram starts at $y=1\text{cm}$ since the edge of the mammographic film. The top right shows the correlation for the two images shown for 30cm x 30cm (an excursion of 15cm in x and y in either direction).

The areas the radiologist outlined in the mammograms were translated directly from the mammograms to the registered tactile maps. For each mammogram and tactile map, the average intensity of each area was calculated, as well as the average in the background (the pixels outside the areas of interest and inside the edge of the image). For the mammograms, the areas highlighted, on average, had a mean more than 20 times greater than the background [table 5.4]. The same areas in the tactile images had a mean more than 14 times the background. Interestingly, the standard deviation for the areas is more than 10 times greater than the background for both mammograms and tactile images. This implies that the areas in question encompass a greater range of values than the background, which is, as expected, comparatively featureless.

Table 5.4. Statistics for areas highlighted by radiologist on mammograms, translated to tactile images. The pixels in the areas are significantly different from the remaining background.

	Mammograms	Tactile Images
Mean Areas / Mean Background	23.72	14.16
St Dev Areas / St Dev Background	13.11	10.39
Observations	31	31
<i>t</i> stat	15.41	10.42
<i>P</i> value	<0.0005	< 0.0005

In order to ascertain that the difference in the mean values in the tactile images is truly due to absolute peaks in the tactile images, and not because the relatively low values of the background are washing out the actual maximum values, we also look at the location of the pixels of highest values in the tactile images and how these compare to the areas highlighted by the radiologist. The pixels with the highest 2.5% of values of the tactile image are considered. This number was chosen as it resulted in total tactile image area not larger than the areas highlighted in the mammograms. Figure 5.26 shows the

mammographic areas of interest and the areas of peak tactile intensity for a mammogram-tactile image pair. The centroids of the areas differ by 4mm between their locations in the two images. Of the 31 areas highlighted by the radiologist, 28 areas had comparable tactile image areas identified by this method, with a mean absolute discrepancy of the centroids of 8.4mm. If we discount the 6 mammograms where the radiologist indicated an overall lack of features then the discrepancy of the area centroids drops to 4.9mm.

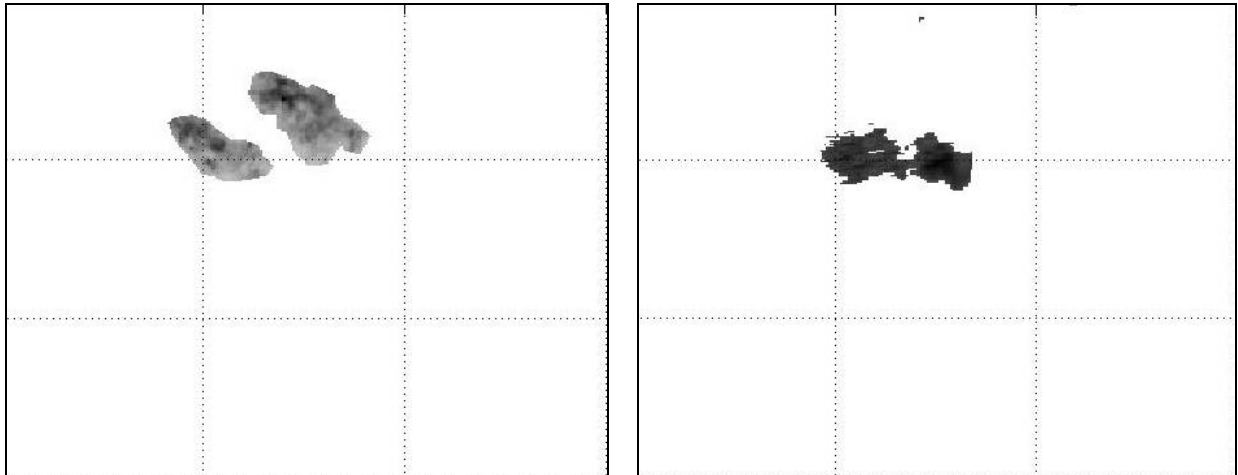


Figure 5.26. Comparing mammography areas to areas of highest intensity in the tactile image. Left: Areas of interest in the mammogram identified by radiologist. Right: Pixels of highest 2.5% intensity in the tactile image. Both images have been cropped in the same manner. The images and grid are the same size.

The above analysis indicates that in general, we expect an overall correlation between areas of increased radioopacity and areas of increased stiffness. We can therefore explore the results of a simple correlation between the two images as a final test of our registration. Figure 5.25 shows the correlation between the tactile image and mammogram shown. In this case, the peak of the correlation is within 3mm of center, indicating that the best match between the two images requires a displacement of only

3mm from their current positions. The correlation peak drops to 25% of its value at a radius of 9.5mm, but the value of the correlation at the center is greater than 99% of the overall correlation peak. This means that as they are, the images are extremely well correlated (99% of peak) and that the correlation of these images is highly position dependent (global maximum is the only local maximum, and the correlation radius is small). The overall results of this correlation analysis are shown in table 5.5.

Table 5.5. Summary of correlation analysis across all mammogram-tactile image pairs.

Mean Correlation quantity	Value
Distance from peak to center	9.9mm
Value at center (% of peak)	95.6%
Radius of correlation peak (at 25% of peak value)	17mm

Figure 5.27 shows another mammogram-tactile image pair. The correlation between these two images is far poorer than that seen in figure 5.25. The tactile image clearly exhibits more extensive stiff regions than the mammogram implies, which result in a poor correlation. Note, however, that near the base of the mammogram there are a few small very bright dots. These are clips left over from a previous surgical biopsy and indicate areas of scar, which is stiffer than the surrounding tissue, but does not image well in mammography a few years post-surgery. Cases like the one in figure 5.27 are just as valuable as that in figure 5.25, since not all pathologies have a mammographic presence [Wellman 01] but may warrant further investigation in a diagnostic setting. These cases, however, help drive down the results in table 5.5.

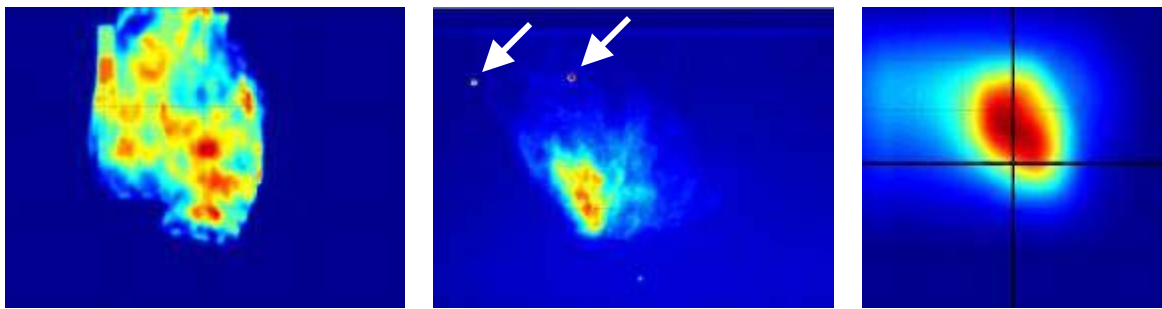


Figure 5.27. A tactile image (left) and mammogram (center) pair (each shown for 20 x 25cm) and their correlation for 20 x 20cm (right). The tactile image shows more bright regions than the mammogram, since this subject has had several biopsies which have resulted in scarring. In the mammogram, the only signature of the scarring are the clips left behind from the biopsies (arrows). The correlation between these two images shows a wide off-center peak, as the best correlation would occur when the bright spots in the tactile image evenly surround the bright spot in the mammogram.

5.5. Discussion

The registration of tactile images to mammograms is inherently dependent on the amount of mammographic compression, the uniformity of that compression, and the breast size, shape, and stiffness characteristics. The registration algorithm generated in this study works well in registering the midplane deformations of four different finite element models, though it is not possible to create an algorithm with constants derived from the simple parameters used in this study that would work perfectly for every breast. The parameters used in the registration algorithm depend only on the extent of the mammogram and tactile image, and are readily available in a clinical setting.

The registration algorithm was developed based on the displacement of the 4mm thick horizontal midplane of the finite element models. In practice, however, the tactile images

obtained on physical breasts (both the silicone models and the images collected clinically) are on a plane that best fits the top surface of the breast as compressed in the tactile image. This plane is not perfectly horizontal, though the approximation to horizontal improves with larger breasts or as the patient ages. In practice, the smallest, stiffest breasts had planes of best fit at angles no greater than 30° , which would result in a maximum error of 13%. In these small breasts, which have a maximum extent less than 6 cm, that translates to an absolute error of 7.8 mm. Although we expect the oblique angle of the tactile imaging plane to result in a registration error, these worst-case calculations indicate that this error is small. This error was one of the dominant errors in the registration of the physical model data, and the good result of that registration confirms that errors due to the angle of the tactile imaging plane are indeed small.

The calibration step required for each clinically collected tactile image was responsible for several centimeters of image manipulation. The displacements required for calibration were greater than the maximum required for registration in more than half of the tactile images collected. Therefore, performing the calibration step well is imperative. This calibration could be improved upon by using another set of fiducials, and by obtaining the plate edge calibrations more completely and more frequently (for example, before and after every subject) since the position of humans in the field of the magnetic tracker affected the overall magnetic warping. A better solution yet would be to move away from a magnetic tracker, which was the main source of the image warping that required calibration. An optical tracker, for example, would not suffer the same problems, and can alleviate this error.

The registration algorithm had lower errors in the premenopausal breast model probably due to the lower absolute displacements and smaller required registration steps. This smaller absolute displacement is expected for all smaller, stiffer breasts, and we may expect the registration to be particularly good in these cases. Practically, however, it is difficult to image breasts in this end of the spectrum under either mammography or tactile imaging. A small, stiff, breast poses a problem in mammography as it is often difficult to obtain sufficient compression of the breast. In this case of small stiff breasts, the problem of a non-horizontal best fit plane is greatest. The resulting image is also quite bright and nonspecific due to the underlying stiffness. Some registration correlation was found for these cases, however the results are difficult to interpret, in that since the extent of the images is so small any absolute error will be small, but relative errors will remain high.

Another possible source of error in registering physical tactile maps to mammograms is that the tactile imager cannot obtain information about the very edge of the breast, unlike mammograms and the finite element model data that was used to generate the registration algorithm. Since the tactile imager requires pressure perpendicular to the tissue, imaging near the edges does not allow imaging against the bottom mammography plate. However, in order for the registration algorithm to work properly, we need information as close to the edge of the breast as possible. If we assume that this difficulty arises after the scanhead has to be tilted to 45° , then the largest error will occur in the thickest breasts. Based on the largest finite element model, this accounts for a discrepancy of up to 9 mm. In practice, since the tactile image is not smooth, by forcing the parabolic

tactile image edge to skirt the outside of the tactile image we help account for this discrepancy. Besides this precautionary step, however, in a clinical setting, full symmetrical coverage of the breast under tactile imaging should be encouraged.

Overall, the results of this study indicate that registration is possible between tactile images and mammograms. The three metrics employed to check clinical registration all had good results well within radiologist tolerance of misregistration. This shows promise in increasing the efficacy of breast cancer screening by adding a new, inexpensive imaging modality registered to the current standard. Due to the passive, noninvasive nature of tactile imaging, the clinical study presented here encountered a very high patient compliance. 100% of subjects approached agreed to participate in the study and all followed through with tactile imaging of both breasts after their mammogram. Only one subject noted discomfort, on one breast which had recently undergone surgery. Even in this case, however, a tactile image was still obtained by imaging in the lowest possible pressure range set in the tactile imager.

5.6. Future Work

The results of this study show promise in increasing the efficacy of breast cancer screening by adding a new, inexpensive imaging modality registered to the current standard. The driving goal of the registration work was to set the foundation for establishing tactile imaging as an adjunct to screening mammography by increasing the

positive predictive value (PPV) of screening. To that end, a means of registering tactile images to mammograms was developed, and a protocol for collecting clinical tactile images was tested on a preliminary study.

The next stage in this study will involve expanding the clinical work to obtain tactile images and mammograms on more subjects beyond the preliminary study presented here. A sample protocol that may be used is included in Appendix B. The resulting mammographic and tactile images will be analyzed by radiologists in a random study and the PPV rates for mammography alone compared to that of mammograms studied in conjunction with tactile images. The results of such a study are needed to establish an increase in the positive predictive value of tactile imaging as an adjunct to screening mammography.

Chapter 6

Summary and Future Work

The work presented in this thesis concerns tactile imaging as it pertains to medical applications. The main focus was on breast pathology screening applications, specifically identifying parameters of imaged tissue and registering tactile images to other imaging modalities. The work presented can be extended to other organs and imaging modalities.

A new approach to storing and displaying tactile information was presented, in the form of tactile scanning, to obtain the composite tactile image (CTI). The two-dimensional CTI contains all the pressure information from the centerline of a tactile image, stacked so that the asymmetry of pressure frames collected near, but not directly over, an irregularity in the underlying tissue is clearly seen. Unlike previous ways of dealing with tactile information, the CTI requires no spatial averaging of the data, and thus there is no inherent loss of information. Tactile scanning enabled the successful estimation of geometry and stiffness parameters from imaged tissue.

A method for estimating the geometric and stiffness parameters of a round lesion attached to the substrate of a tissue was developed in chapter 2. A linear inversion algorithm was used to estimate the underlying parameters from finite element data and physical model data. The work presented in this thesis on parameter estimation is the first to successfully estimate lesion stiffness from tactile imaging data. The errors incurred are within the separation of the elastic moduli of different pathologies, and so the results show promise for clinical application.

The inversion algorithm used was effective despite being linear. It was shown that, although tactile imaging is not inherently linear in the underlying geometry and stiffness parameters, approximate linearity can be found between the tactile information and simple combinations of the parameters. Parameter linearization for use in tactile image inversion proved to be an important feature in expanding the limits of the parameter estimation problem to include the estimation of the tissue and lesion moduli.

In chapter 3, the inversion algorithm developed for a lesion attached to the substrate of a soft tissue was applied to the expanded problem of a lesion embedded within the soft tissue substrate. This problem has a larger parameter space due to the addition of the parameter related to the depth of the lesion, and so the tactile scanning data was divided based on a simple parameter from the CTI. The results of estimating the underlying parameters from finite element models were once again within clinical relevance, and so the work can be carried forward to model and clinical testing.

The estimation of tissue parameters in the case of a round inclusion wholly embedded in tissue is analogous to the estimation of large vessel parameters. The liver is an ideal candidate for this as it is a large, solid organ, with large thin-walled veins traversing its bulk. The inversion algorithm developed for solid lesions was easily applied to finite element models of human liver and excised, perfused, porcine livers, with good local results. Estimating the tissue thickness showed greater errors than expected from the previous analysis, and is likely due to the thin wedge shape of the porcine liver lobes. The thinness of the tissue results in a greater strain in the tissue, and thus accentuates the nonlinearity of the tissue elasticity, while the nonuniformity of the tissue thickness resulted in errors in recording the actual tissue thickness for estimation. Despite the errors incurred in estimating the specific parameters of the porcine livers studied, tactile imaging was clearly able to distinguish embedded vessels and provide information on their geometry.

The success of the inversion algorithm developed for specific tissue geometries naturally led to the question of where the limits of general inversion lie. Thus in chapter 4, we tackled the problem of a stiff substrate of continually varying thickness under a soft layer with complementary thickness (i.e. the total thickness of the two layers was constant). Using the result that tactile scanning is approximately linear in a simple combination of substrate and total thickness, we found the impulse response of our system. We showed that the resolution of the inversion is limited by the width of this impulse response, which in turn is dependent on the stiffness of the top layer of tissue. Further work can be

performed in detailing the dependence of this resolution to scanhead design, and applying the continuous inversion algorithm developed to physical data.

Chapter 5 detailed the work in developing an algorithm to register tactile images to mammograms. Since tactile imaging essentially quantifies palpation, it is a logical adjunct to mammography, which ideally is performed with concurrent palpation information of the breasts being imaged. Our premise was that by changing the way that tactile images are obtained (taking the images with the woman standing, rather than laying on her back in the traditional palpation posture) we may find a way to register the resulting tactile image to mammograms. We developed the registration algorithm based on results from finite element models constructed from breast contour data. The registration algorithm was applied to the tactile image obtained on a realistic physical three-dimensional breast model and the resulting image compared to a simulated mammogram of the model. The registration of points within the finite element and physical models was successful enough to attempt registration of clinically obtained tactile images to their attendant mammograms.

A protocol was established for obtaining clinical tactile images for a preliminary study performed in a screening mammography setting. This study highlighted the importance of image calibration, and a robust calibration algorithm was developed. Calibration and registration was performed on each tactile image collected. The mammograms were presented to a radiologist who identified areas of interest in the field of the mammogram. Analysis of these areas in both the mammogram and the tactile image showed a strong

correlation between these areas and areas of intensity in the tactile image. Overall correlations between tactile images and mammograms also proved to be robust, as poor correlations were the result of underlying pathology rather than a poor registration. This work lays the foundation for a larger clinical study that can examine a possible increase in the positive predictive value of breast cancer screening if tactile imaging is used as an adjunct to screening mammography.

The finite element models developed for the work in this thesis were constructed with linear elastic materials, which is not necessarily representative of biological tissue. Results from these linear models were used to guide the development of the estimation and registration algorithms already discussed. The algorithms were successful in application to physical data, which supports the conclusion that the data they were based on is congruent to data obtained on physical systems. Future work, however, may focus on regenerating the finite element data using more realistic nonlinear materials. In this way, the relationship between the nonlinear material properties and the tactile or displacement data can be studied. This may lead to innovations in the algorithms not possible with the linear data available for this work, which in turn may yield better results when the algorithms are applied to clinical data.

The work on the registration algorithm, combined with the parameter estimation work of the previous chapters, is a coherent tactile imaging package that can provide quantitative tissue geometry and stiffness information to soft tissue imaging. The work on continuous estimation of tissue parameters has shown us the inherent limits of tactile imaging using

the current sensors, yet even within these limits the stiffness maps that can be achieved may prove to be an important adjunct to the radioopacity measures of mammography. The registration work developed in this thesis can easily be expanded to imaging modalities beyond mammography and tactile imaging as long as the inherent tissue compression is compatible. Therefore, other modalities can be included in the registration, to provide multiple observations of the same tissue. The ideal long-term application of the work in this thesis would see tactile imaging performed in a screening or diagnostic setting in conjunction with other modalities, where tactile imaging provides a map of the underlying tissue stiffness to the harmony of registered information.

References

- ACS, American Cancer Society, "Breast Cancer Screening Guidelines", 2003.
- Azar, F. S., Metaxas, D. N. and Schnall, M. D., Methods for modeling and predicting mechanical deformations of the breast under external perturbations. MICCAI 2001, Springer-Verlag. 2001.
- Barton, M. B., Harris, R. and Flethcer, S., "Does This Patient Have Breast Cancer? (The rational clinical examination)." JAMA **282**(13): 1270, 1999.
- Carter, F. J., Frank, T. G., Davies, P. J., McLean, D. and Cuschieri, A., "Measurements and modelling of the compliance of human and porcine organs." Medical Image Analysis **5**: 231-236, 2001.
- Chen, D. T., Kakdiaris, I. A., Miller, M. J., Loftin, R. B. and Patrick, C., "Modeling for Plastic and Reconstructive Breast Surgery." MICCAI 2000.
- Childress, D. S. and Berkley, J. J., "Determining soft tissue material properties for the purpose of finite element modeling of the below knee amputee residual limb." 1997.
- Cotin, S., Delignette, H. and Ayache, N., "Real-time elastic deformations of soft tissues for surgery simulation." IEEE Transactions on visualization and computer graphics **5**(1): 62-72, 1999.
- Crawford, J. M. and Cotran, R., The Liver and the Biliary Tract. Robbins Pathologic Basis of Disease. R. Cotran. Philadelphia, WB Saunders Co.: Ch 19, 1999.
- Cundari, M. A., West, A. I., Noble, B. D., Roberts, T. W. and Widder, D. R., "Clinical tissue examination". US Patent #6,091,981, July 18, 2001.
- Cundari, M. A., West, A. I. and Roberts, T. W., "Layer of material for use with tissue examination device". USA Patent #6,179,790, January 30, 2001.
- DiBartolo, B., Classical Theory of Electromagnetism. USA, Prentice Hall, 1991.
- Durduran, T., Choe, R., Culver, J. P., Zubkov, L., Holboke, M. J., Giamarco, J., Chance, B. and Yodh, A. G., "Bulk Optical Properties of Healthy Female Breast Tissue." Phys. Med. Biol. **47**: 2847-2861, 2002.
- Eshelby, J. D., "The determination of the elastic field of an ellipsoidal inclusion and related problems." Proc R Soc Lond **A241**: 376-396, 1957.

Eshelby, J. D., "The Elastic Field Outside an Ellipsoidal Inclusion." Proc R Soc Lond **252**(1271): 561-569, 1959.

Evans, M. F., "False-positive results in breast cancer screening." Canadian Family Physician **45**: 73-74, 1999.

Frei, E. H., Sollish, B. D., Yerushalmi, S., Lang, S. B. and Moskitzky, M., "Instrument for viscoelastic measurement". USA Patent February 17, 1981.

Friedlander, C. C. and C. C., "Breast Imaging Today and Tomorrow." Nurse Practitioners' Forum **10**(3): 129-36, 1999.

Fung, Y. C., Biomechanics: Mechanical Properties of Living Tissues. New York, Springer Verlag, 1993.

Goodier, J. N., "Concentration of stress around spherical and cylindrical inclusions and flaws." Phil Mag **7**(22): 678, 1936.

Gray, H., Gray's Anatomy, Running Press, 1901.

Grundfest-Brondatowski, S., et al, ed. Controversies in Breast Disease: Diagnosis and Management. Marcel Dekker Inc., New York, 1998.

Hansen, Christian Per, Rank-Deficient and Discrete Ill-Posed Problems: Numerical Aspects of Linear Inversion, 1998

Health, P. i., Digitizing x-rays. Cambridge, MA, MDB-TR Medical Record, 2002.

Hendrickson, D., "Digital imaging company hopes to aid early breast cancer detection." Mass High Tech: 5, 2003.

Hermann, G., et al., Nonpalpable Breast Cancer: Diagnosis and Management. New York, Igaku-Shoin, 1992.

Hyvarinen, A., Karkunen, J. and Oja, E., Independent Component Analysis. New York, John Wiley & Sons Inc., 2001.

Imaginis, "<http://imagineis.com/breasthealth/statistics.asp>.", 2003.

Jatoi, I., Breast Cancer Screening. New York, Chapman and Hall, 1997.

Johnson, K. L., Contact Mechanics. Cambridge, Cambridge University Press, 1985.

Kita, Y., Tohno, E., Highnam, R. P. and Brady, M., A CAD system for 3D locating of lesions in mammogram. MICCAI 2001, Springer-Verlag. 2001.

Komen, "<http://www.columbusraceforthecure.org/education/womenshealth.asp>.", 2003.

Kopans, D. B., "Clinical breast examination for detecting breast cancer." JAMA **283**(13): 1688, 2000.

Krouskop, T. A. et al, "Elastic Moduli of Breast and Prostate Tissues under Compression." *Ultrasonic Imaging* **20**: 260-74, 1998.

Krouskop, T. A., Price, R. E., Wheeler, T. and Younes, P. S., Modulus Variations in Breast Tissues. 1st Int. Conf. On the Ultasonic Measurement and Imaging of Tissue Elasticity, Niagara Falls, ON, CA. 2002.

Krucker, J. F., Meyer, C. R., LeCarpentier, G. L., Fowlkes, B. and Carson, P. L., "3D Spatial Compounding of Ultrasound Images using Image-Based Nonrigid Registration." *Ultrasound in Med. & Biol.* **26**(9): 1475-1488, 2000.

LaScalzaa, S., Aricob, J. and Hughes, R., "Effect of metal and sampling rate on accuracy of Flock of Birds electromagnetic tracking system." *J. Biomechanics* **36**(1): 141-144, 2003.

Lavin, P. T. and G., F., "Studies in cariation associated with the measurement of solid tumors." *Cancer* **46**: 1286-90, 1980.

Lester, S. and Cotran, R., The Breast. Robbins Pathologic Basis of Disease. R. Cotran. Philadelphia, WB Saunders Co.: Ch 25, 1999.

Maier, C. F., Nikolov, H., Chu, K., Chronik, B. and Rutt, B. K., "Practical Design of a High-Strength Breast Gradient Coil." *Magnetic Resonance in Medicine* **39**: 392-401, 1998.

Marginal, A primer on image histograms and curves. New York, Marginal Software, 2002.

Maurel, W., Wu, Y., Thalmann, N. M. and Thalmann, D., Biomechanical Models for Soft Tissue Simulation, Springer-Verlag, 1998.

Medical Scientists, I., Estimated Sensitivity and Specificity of Clinical Breast Examination and Breast Self-Examination for Breast Lumps and Breast Cancer, 1997.

Meyer, C. R., Boes, J. L., Kim, B., Bland, P. H., LeCarpentier, G. L., Fowlkes, B., Roubidoux, M. A. and Carson, P. L., "Semiautomatic Registration of Volumetric Ultrasound Scans." *Ultrasound in Med. & Biol.* **25**(3): 339-347, 1999.

Miller, K., "Biomechanics of soft tissues." *Med Sci Monit* **6**(1): 158-167, 2000.

Milne, A. D., Chess, D. G., Johnson, J. A. and King, G. J. W., "Accuracy of an electromagnetic tracking device: A study of the optimal operating range and metal interference." *J. Biomechanics* **29**: 791-6, 1996.

Niemczyk, P., Sarvazyan, A. P., Fila, A., Amenta, P., Ward, W., Javidian, P., Breslauer, K. and Summings, K., "Mechanical Imaging, a new technology for cancer detection." *Surgical Forum* **47**(96): 823-825, 1996.

Ortega, J. M., Matrix Theory: A second course. New York, Plenum press, 1987.

Ottensmeyer, M. P. and Salisbury, J. K. J., In Vivo Data Acquisition Instrument for Solid Organ Mechanical Property Measurement. MICCAI, Springer-Verlag. 2001.

Pennypacker, H. S. et al, "Why can't we do better breast examinations?" Nurse Prac. Forum **10**(3): 122-8, 1999.

Picinbono, G., Delignette, H. and Ayache, N., "Non-linear and anisotropic elastic soft tissue models for medical simulation." Epiduare Project, 2003.

Poulin, F. and Amiot, L.-P., "Interference during the use of an electromagnatic tracking system under OR conditions." J. Biomechanics **35**(2002): 733-737, 2002.

Reuckert, D., "Nonrigid Registration using Freeform Deformations: Application to Breast MR Images." IEEE Trans Med Imag **18**: 712-21, 1999.

Ronnov-Jessen, L., Petersen, O. and Bissel, M., "Cellular changes involved in conversion of normal to malignant breast: Importance of the stromal reaction." Physiological Reviews **76**(1): 69-125, 1996.

Sanada, M., Ebara, M., Fukuda, H., Yoshikawa, M., Sugiura, N., Saisho, H., Yamakoshi, Y., Ohmura, K., Kobayashi, A. and Kondo, F., "Clinical evaluation of sonoelasticity measurement in liver using ultrasonic imaging of internal forced low-frequency vibration." Ultrasound in Med. & Biol. **26**(9): 1455-1460, 2000.

Sarvazyan, A. P., "Mechanical imaging: A new technology for medical diagnostics." International Journal of Medical Informatics **49**: 195-216, 1998.

Sarvazyan, A. P., "Device for breast haptic examination". USA Patent #5,833,633, Nov 10, 1998.

Sarvazyan, A. P., Computerized Palpation is more sensitive than the human finger. Proc 12th Int Symp on Biomedical Measurements and Instrumentation, Dubrovnik-Croatia. 1998.

Sarvazyan, A. P., "Method and device for mechanical imaging of breast". USA Patent #5,860,934, Jan 19, 1999.

Sarvazyan, A. P., Skovoroda, A. R., Emelianov, S. Y., Fowlkes, J. B., Pipe, J. G. and Adler, R. S., Biophysical bases of elasticity imaging. Acousti. Imaging. J. P. Jones. New York, Plenum. **21**: 223-240, 1995.

Sarvazyan, A. P., Skovoroda, A. R. and Pyt'ev, Y. P., Mechanical introscopy - a new modality of medical imaging for detection of breast and prostate cancer. Eighth IEEE Symp. Computer Based Med. Sys. 1997.

Services, U. D. o. H. a. H., High-Quality Mammography: Information for referring providers. Rockville, MD, Agency for Health Care Policy and Research, 1994.

Strang, G., Linear Algebra and its applications. New York, Academic Press, 1980.

Tavassolis, Atlas of Breast Pathology, 1996.

Thomas, C. L., Taber's Cyclopedic Medical Dictionary. Philadelphia, F.A. Davis Co., 1997.

Thurfjell, L., "Improved Efficiency for MRI-SPET Registration Based on Mutual Information." Eur. J. Nuclear Med. **27**: 847-56, 2000.

Transmed., www.transmed.com. 1997.

US Dept of Health and Human Services: Clinical Practice Guideline. High Quality Mammography: Information for referring providers. Agency for Health Care Policy and Research. Rockville, MD, 1994

van Engeland, S. and Karssemeijer, N., Matching Breast lesions in multiple mammographic views. MICCAI 2001, Springer-Verlag. 2001.

Wang, Y., Nguyen, C., Srikanthana, R., Geng, Z. and Freedman, M. T., Tactile Mapping of Palpable Abnormalities for Breast Cancer Diagnosis. IEEE Intl. Conf. Robotics Automation. 1999.

Weber, G., Using Tactile Images to Differentiate Breast Cancer Types. Division of Engineering and Applied Sciences. Cambridge, Harvard University, 2000.

Weber, G., www.griffinweber.com, 2000.

Wellman, P. S., Tactile Imaging. Division of Engineering and Applied Sciences. Cambridge, Harvard University: 137, 1999.

Wellman, P. S., Howe, R. D., Dewagan, N., Cundari, M. A., Dalton, E. P. and Kern, K. A., Tactile imaging: a method for documenting breast masses. First joint Biomed Eng Soc/IEEE Eng Med Bio Soc Conf. 1999.

Wellman, P. S., Dalton, E. P. and al, e., "Tactile Imaging of Masses: First Clinical Report." Archives of Surgery **136**(2): 204-8, 2001.

Wells, W. M., "Multi-modal Volume Registration by Maximization of Mutual Information." Med. Imag. Anal. **1**: 35-51, 1996.

West, A. I., Krag, D., Weinstein, J. B. and Dewagan, N., "Obtaining images of structures in bodily tissue". USA Patent December 31, 2002.

Yu, H. Y. and Sanday, S. C., "Axisymmetric Inclusion in a Half Space." Journal of Applied Mechanics **57**(March): 74-77, 1990.

Yu, H. Y. and Sanday, S. C., Elastic field in joined semi-infinite solids with an inclusion. Proc R Soc Lond, London. 1991.

Appendix A

Parameters for finite element models created for parameter estimation work

A.1.

Parameters for fixed lesion finite element models with varying background modulus B

B [Pa]	L [Pa]	t [m]	d [m]
15000	15000	0.025	0.015
15000	22500	0.025	0.015
15000	22500	0.03	0.015
15000	30000	0.025	0.015
15000	30000	0.03	0.015
15000	45000	0.03	0.01
15000	45000	0.025	0.015
15000	45000	0.03	0.0175
15000	45000	0.02	0.005
15000	45000	0.03	0.015
15000	75000	0.025	0.015
15000	75000	0.03	0.015
15000	75000	0.03	0.02
15000	75000	0.025	0.01
15000	75000	0.025	0.0075
15000	75000	0.03	0.0175
15000	75000	0.03	0.01
13000	130000	0.025	0.01
13000	130000	0.03	0.0175
13000	130000	0.04	0.02
13000	130000	0.04	0.015
13000	130000	0.02	0.005
15000	150000	0.025	0.015
15000	150000	0.03	0.015
15000	150000	0.04	0.02
15000	150000	0.03	0.02
15000	150000	0.03	0.0175
15000	150000	0.03	0.01
15000	150000	0.025	0.01
15000	150000	0.025	0.0075
15000	150000	0.02	0.005
40000	200000	0.025	0.01
40000	200000	0.025	0.0075
15000	300000	0.025	0.015
15000	300000	0.03	0.015
15000	300000	0.04	0.015
15000	300000	0.04	0.02
40000	400000	0.03	0.0175
40000	400000	0.025	0.01
40000	400000	0.025	0.0075

15000	450000	0.02	0.005
15000	450000	0.03	0.015
15000	450000	0.025	0.015
15000	450000	0.03	0.01
50000	500000	0.025	0.015
50000	500000	0.03	0.015
50000	500000	0.04	0.015
50000	500000	0.04	0.02
50000	500000	0.03	0.01
50000	500000	0.04	0.015
50000	500000	0.02	0.005
15000	600000	0.03	0.015
15000	600000	0.025	0.015
15000	750000	0.025	0.015
15000	750000	0.03	0.015
15000	1500000	0.025	0.015
15000	1500000	0.03	0.015
15000	1500000	0.03	0.02
15000	1500000	0.025	0.01
15000	1500000	0.025	0.0075
15000	1500000	0.03	0.01
15000	1500000	0.03	0.0175
15000	1500000	0.04	0.015
15000	1500000	0.02	0.005
30000	1500000	0.025	0.015
30000	1500000	0.04	0.02
15000	2500000	0.025	0.015
15000	2500000	0.03	0.02
15000	2500000	0.025	0.01
15000	2500000	0.025	0.0075
50000	2500000	0.025	0.015
50000	2500000	0.03	0.015
50000	2500000	0.04	0.015
50000	2500000	0.04	0.02
18000	3600000	0.03	0.015
15000	5000000	0.025	0.015
50000	5000000	0.025	0.015
50000	5000000	0.03	0.015
50000	5000000	0.04	0.015
50000	5000000	0.04	0.02
50000	5000000	0.03	0.01
50000	5000000	0.02	0.005

A.2.

Parameters for fixed lesion finite element models with constant background modulus
 $B = 15 \text{ kPa}$

B [Pa]	L [Pa]	t [m]	d [m]
15000	30000	0.03	0.015
15000	30000	0.025	0.015
15000	45000	0.03	0.015
15000	45000	0.03	0.0175
15000	45000	0.03	0.01
15000	45000	0.025	0.015
15000	75000	0.03	0.015
15000	75000	0.03	0.01
15000	75000	0.03	0.0175
15000	75000	0.025	0.015
15000	75000	0.025	0.01
15000	75000	0.025	0.0075
15000	150000	0.04	0.02
15000	150000	0.03	0.01
15000	150000	0.03	0.015
15000	150000	0.03	0.02
15000	150000	0.025	0.01
15000	150000	0.025	0.0075
15000	150000	0.025	0.015
15000	150000	0.02	0.005
15000	300000	0.04	0.015
15000	300000	0.04	0.02
15000	300000	0.03	0.015
15000	300000	0.025	0.015
15000	450000	0.03	0.015
15000	450000	0.025	0.015
15000	450000	0.02	0.005
15000	600000	0.03	0.015
15000	600000	0.025	0.015
15000	750000	0.03	0.015
15000	750000	0.025	0.015

A.3.

Parameters for fixed lesion physical models with constant background modulus
 $B = 15 \text{ kPa}$

L [kPa]	t [mm]	d [mm]
137.00	25.77	12.70
137.00	25.77	14.10
137.00	30.47	17.15
137.00	38.04	25.40
137.00	18.53	12.70
137.00	18.53	14.10
137.00	30.47	25.40
231.26	30.28	15.88
231.26	30.28	17.15
231.26	36.23	25.40
231.26	26.8	19.05
231.26	19.25	15.88
231.26	19.25	17.15
231.26	26.8	25.40
430.93	25.5	12.70
430.93	37.19	19.05
430.93	28.79	15.88
430.93	25.5	14.10
430.93	28.79	17.15
482.80	35.76	19.05
430.93	28.39	19.05
430.93	18.06	12.70
430.93	20.73	15.88
430.93	18.06	14.10
482.80	27.16	19.05
482.80	35.76	25.40
430.93	20.73	17.15
430.93	28.39	25.40
482.80	27.16	25.40

A.4. Parameters for floating lesion finite element models with constant background modulus $B = 15 \text{ kPa}$

High CTIa:

L [Pa]	t [m]	d [m]	z [m]
30000	0.095	0.015	0.045
30000	0.065	0.015	0.030
30000	0.085	0.015	0.040
30000	0.045	0.015	0.020
30000	0.050	0.020	0.020
30000	0.070	0.020	0.030
30000	0.090	0.020	0.040
45000	0.085	0.015	0.040
45000	0.065	0.015	0.030
45000	0.095	0.015	0.045
45000	0.045	0.015	0.020
45000	0.070	0.020	0.030
45000	0.090	0.020	0.040
45000	0.050	0.020	0.020
75000	0.085	0.015	0.040
75000	0.095	0.015	0.045
75000	0.045	0.015	0.020
75000	0.065	0.015	0.030
75000	0.090	0.020	0.040
75000	0.050	0.020	0.020
75000	0.070	0.020	0.030
150000	0.065	0.015	0.030
150000	0.085	0.015	0.040
150000	0.045	0.015	0.020
150000	0.095	0.015	0.045
150000	0.070	0.020	0.030
150000	0.090	0.020	0.040
150000	0.050	0.020	0.020

Low CTIa:

L [Pa]	t [m]	d [m]	z [m]
30000	0.100	0.005	0.055
30000	0.030	0.005	0.020
30000	0.080	0.005	0.045
30000	0.060	0.005	0.035
30000	0.040	0.005	0.025
30000	0.070	0.010	0.040
30000	0.045	0.010	0.025
30000	0.050	0.010	0.030
30000	0.095	0.010	0.050
30000	0.085	0.010	0.045
30000	0.090	0.010	0.050
30000	0.065	0.010	0.035
45000	0.030	0.005	0.020
45000	0.080	0.005	0.045
45000	0.060	0.005	0.035
45000	0.100	0.005	0.055
45000	0.040	0.005	0.025
45000	0.050	0.010	0.030
45000	0.045	0.010	0.025
45000	0.095	0.010	0.050
45000	0.090	0.010	0.050
45000	0.085	0.010	0.045
45000	0.070	0.010	0.040
45000	0.065	0.010	0.035
75000	0.080	0.005	0.045
75000	0.030	0.005	0.020
75000	0.060	0.005	0.035
75000	0.040	0.005	0.025
75000	0.100	0.005	0.055
75000	0.090	0.010	0.050
75000	0.065	0.010	0.035
75000	0.085	0.010	0.045
75000	0.095	0.010	0.050
75000	0.070	0.010	0.040
75000	0.050	0.010	0.030
75000	0.045	0.010	0.025
150000	0.080	0.005	0.045
150000	0.030	0.005	0.020
150000	0.100	0.005	0.055
150000	0.040	0.005	0.025
150000	0.060	0.005	0.035
150000	0.070	0.010	0.040
150000	0.090	0.010	0.050
150000	0.065	0.010	0.035
150000	0.095	0.010	0.050
150000	0.085	0.010	0.045
150000	0.045	0.010	0.025
150000	0.050	0.010	0.030

A.5.

Parameters for finite element models of liver with central vessel

B [Pa]	t [m]	d [m]
12500	0.06	0.005
12500	0.06	0.0065
12500	0.05	0.0065
12500	0.04	0.005
15000	0.05	0.005
12500	0.05	0.008
12500	0.06	0.008
12500	0.05	0.005
15000	0.05	0.0065
15000	0.06	0.0065
12500	0.04	0.0065
15000	0.04	0.005
15000	0.06	0.005
15000	0.06	0.008
15000	0.05	0.008
12500	0.05	0.01
12500	0.06	0.01
10000	0.06	0.005
15000	0.04	0.0065
10000	0.05	0.005
10000	0.05	0.0065
15000	0.05	0.01
10000	0.04	0.005
10000	0.06	0.0065
15000	0.06	0.01
10000	0.06	0.008
10000	0.05	0.008
15000	0.04	0.008
12500	0.04	0.008
10000	0.04	0.0065
10000	0.06	0.01
10000	0.05	0.01
10000	0.04	0.008
12500	0.04	0.01
15000	0.04	0.01
10000	0.04	0.01

Appendix B

Suggested Protocol for Future Clinical Work in Mammography Registered Tactile Imaging

B.1. Introduction

The initial clinical study, presented in chapter 5, provided preliminary clinical data on which to test our registration algorithm. Equally important, however, is the knowledge gained towards optimizing a larger clinical trial to continue the work started in this thesis. In this appendix we include a suggested protocol for collecting and analyzing mammograms and tactile images in order to show an increase in the positive predictive value (PPV) of screening mammography when tactile imaging is used as an adjunct.

The PPV is the measure of true positive results to all positive results. True positive results account for only a small fraction (approximately 1%) of screening cases, and about 10% of diagnostic cases. Therefore, in order to test for an increase in the PPV of mammography with tactile imaging over the PPV of mammography alone on a reasonable number of subjects, the clinical trial should be performed on subjects undergoing a diagnostic mammogram. This will still require the number of subjects to be

on the order of 100 or more, however is an improvement over the case of pure screening mammography.

B.2. Protocol

Subjects will be recruited from patients referred for a diagnostic mammogram. Informed consent will be obtained when the subject is received at the diagnostic unit, and she (or he) will undergo all procedures as usual. The tactile imager will be set up in the mammography suite with a reclining bed also available for the supine tactile image. Tactile images of one or both breasts (depending on whether one or both breasts are to be imaged by mammography) can then be obtained in the cranio-caudal plane with the subject standing at the mammography machine, as well as with the subject supine on the bed, which images a larger area, but is not directly registered with the mammogram.

Copies of the regular screening mammography views will be made, with regard for patient confidentiality. These are the cranio-caudal and medio-lateral x-rays, henceforth referred to as “the mammograms”. The master database will consist of these mammograms, the tactile images, and the final diagnosis. The mammograms and tactile images will be shown to various radiologists for their assessment. This assessment will be compared to the patient’s diagnosis for statistical analysis

B.2.1. Radiologists' Involvement

This study requires the involvement of several radiologists to read mammograms as well as tactile images. Since the hypothesis of this work is that tactile imaging is an effective adjunct to mammography, the images from tactile imaging should be read at the same time as the mammography images. Radiologists are thus the prime candidates for this study to target. Radiologists are also quite used to viewing images taken by different imaging techniques, in different planes, and constructing a mental image of the three-dimensional position of noticeable structures. They will be trained to read tactile images and shown examples of tactile images registered to mammography prior to the study.

B.2.2. Study Phases

Phase I

The initial phase is designed to provide immediate validation of the imaging and radiologist protocols. Up to 40 subjects will be recruited and tactile images obtained in two planes, as described above. These subjects will be selected such that at least 50% of them present with a palpable lump. This biases the initial study in favor of cases which can be visualized with tactile imaging, to afford the most immediate assessment of the function of tactile imaging in this context. Copies of the subjects' mammograms and diagnostic reports will be obtained and assembled with the tactile maps into the main database. A pool of 6 radiologists will then assess each of the following imaging modalities, for 10 patients at a time:

- The regular screening mammograms
- The mammograms and the registered cranio-caudal tactile images
- The mammograms and the supine tactile images
- The mammograms and both sets of tactile images

Random selection will determine which of the above imaging modalities for any one patient each radiologist assesses. Each radiologist will provide a decision on whether there is an abnormality that should be evaluated further, and the location of that abnormality. The experience of each radiologist will also be recorded for use in the statistical analysis.

After 40 patients have been assessed, the sensitivity and specificity of each imaging modality will be calculated, and an Analysis of Variance (ANOVA) performed, in order to isolate the effects of imaging modality, underlying pathology, and radiologist variability.

Phase II

Once the best imaging modality is determined, the study will be streamlined accordingly, and another 60 patients will be recruited, again with a 50% bias towards patients with a palpable abnormality. After each set of 20 patients the assessing radiologists will be asked to review the images and provide a decision about the presence of an abnormality.

The positive predictive value will be assessed and ANOVA performed after these initial 100 patients.

Phase III

The final phase of the study will recruit patients with no bias for palpable lesions. Some of these subjects will be therefore be regular screening patients. The images obtained from these subjects will be assessed as above, and the results tabulated for presentation.

B.3. Notes

All clinical trials involving human subjects must be approved by an Independent Review Board (IRB), which is staffed by people familiar with the proper protocols for human subject trials. The nature of the work suggested here, however, requires the recruitment of people (mostly women) who are enduring a very stressful and possibly emotional experience – facing the possibility of breast cancer. This should be kept in mind at all times, and the needs of the patient always given the highest priority. The emphasis on women already scheduled for a mammogram was established so that no subject is asked to undergo radiation exposure, no matter how minimal, for this study. Similarly, no aspect of the subject's regular care should ever be hampered for any facet of this study. Our experience from the initial study taught us that some women, especially in a more relaxed screening environment, and those women who have a personal history of breast

cancer, were eager to help in any way they could, particularly for a noninvasive test such as tactile imaging. Recruiting a few subjects from such a group at the initial phase might be of great benefit if this is the researchers' first exposure to clinical trials. A caring breast surgeon with an established practice can be invaluable in helping identify subjects that would be ideal for such an initial study.